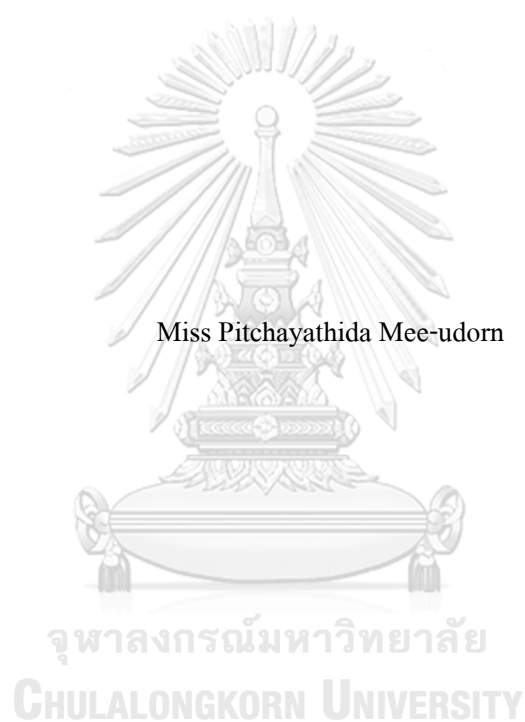CATALYTIC MECHANISM AND INHIBITION OF *Plasmodium* sp. SERINE

HYDROXYMETHYLTRANSFERASE BY COMPUTATIONAL SIMULATIONS

Miss Pitchayathida Mee-udorn

จุฬาลงกรณ์มหาวิทยาลัย

CHULALONGKORN UNIVERSITY

A Dissertation Submitted in Partial Fulfillment of the Requirements

for the Degree of Doctor of Philosophy in Bioinformatics and Computational Biology

Inter-Department of Bioinformatics and Computational Biology

GRADUATE SCHOOL

Chulalongkorn University

Academic Year 2022

กลไกการเร่งปฏิกิริยาและการยับยั้งของเอนไซม์ซีรีนไฮดรอกซีเมทิลทรานสเฟอเรสของ
Plasmodium sp. โดยการจำลองเชิงคอมพิวเตอร์

น.ส.พิชญธิดา มีอุดร

จุฬาลงกรณ์มหาวิทยาลัย
CHULALONGKORN UNIVERSITY

วิทยานิพนธ์นี้เป็นส่วนหนึ่งของการศึกษาตามหลักสูตรปริญญาวิทยาศาสตรดุษฎีบัณฑิต
สาขาวิชาชีวสารสนเทศศาสตร์และชีววิทยาเชิงคอมพิวเตอร์ (สหสาขาวิชา) สหสาขาวิชาชีวสารสน
เทศศาสตร์และชีววิทยาทางคอมพิวเตอร์
บัณฑิตวิทยาลัย จุฬาลงกรณ์มหาวิทยาลัย
ปีการศึกษา 2565

Thesis Title	CATALYTIC MECHANISM AND INHIBITION OF *Plasmodium* sp. SERINE HYDROXYMETHYLTRANSFERASE BY COMPUTATIONAL SIMULATIONS
By	Miss Pitchayathida Mee-udorn
Field of Study	Bioinformatics and Computational Biology
Thesis Advisor	Associate Professor Dr. THANYADA RUNGROTMONGKOL

Accepted by the GRADUATE SCHOOL, Chulalongkorn University in Partial Fulfillment of the Requirement for the Doctor of Philosophy

.... Dean of the GRADUATE SCHOOL

(Associate Professor Dr. YOOTTHANA CHUPPUNNARAT)

DISSERTATION COMMITTEE

.... Chairman

(Associate Professor Dr. TEERAPONG BUABOOCHA)

.... Thesis Advisor

(Associate Professor Dr. THANYADA RUNGROTMONGKOL)

.... Examiner

(Professor Dr. PORNTHEP SOMPORNPISUT)

.... Examiner

(Assistant Professor Dr. SITTIPORN PATTARADILOKRAT)

.... External Examiner

(Dr. Penchit Chitnumsub)

พิชญ์ธิดา มีอุดร : กลไกการเร่งปฏิกิริยาและการยับยั้งของเอนไซม์ซีรีนไฮดรอกซีเมทิลทรานสเฟอเรสของ *Plasmodium* sp. โดยการจำลองเชิงคอมพิวเตอร์. (CATALYTIC MECHANISM AND INHIBITION OF *Plasmodium* sp. SERINE HYDROXYMETHYLTRANSFERASE BY COMPUTATIONAL SIMULATIONS) อ. ที่ปรึกษาหลัก : รศ. ดร.ธัญญดา รุ่งโรจน์มงคล

มาลาเรียได้แพร่กระจายไปในหลายประเทศ โดยมีผู้เสียชีวิตเพิ่มขึ้นถึง 12% หลังจากการอุบัติของโควิด-19 ซึ่งใน บริเวณลุ่มแม่น้ำโขง พบประสิทธิภาพของยาต้านมาลาเรียลดลง เนื่องมาจากสาเหตุการดื้อยา ดังนั้นการค้นหาโปรตีนเป้าหมาย ใหม่ ๆ ที่น่าสนใจจึงเกิดขึ้น โดยเอนไซม์ซีรีนไฮดรอกซีเมทิลทรานเฟอเรสของพลาสโมเดียมก่อโรคมาลาเรีย เป็นเอนไซม์ที่มี โครงสร้าง การทำงาน และกลไกการเข้าจับที่แตกต่างจากของมนุษย์ จึงถูกนำมาศึกษาในการศึกษานี้ โดยเริ่มจากการศึกษากลไก การทำงานของเอนไซม์ด้วยด้วยวิธีทางคอมพิวเตอร์ (Combined quantum mechanics/molecular mechanics molecular dynamics (QM/MM MD) simulations) ซึ่งกำหนดให้ E56 และ Y64 ที่อยู่ในบริเวณจับของเอนไซม์ เป็นกรดอะมิโนที่ทำหน้าที่รับ-ส่ง อิเล็กตรอนในปฏิกิริยา จากการศึกษาพบว่า ปฏิกิริยาเกิดขึ้นได้จนถึงขั้นการเกิด Formaldehyde ปฏิกิริยาไม่สามารถดำเนินต่อไป ได้ จึงสรุปได้ว่า Level of theory ที่ใช้คำนวณไม่เหมาะสมกับ QM region ของกลไกนี้ อาจต้องทำการเปลี่ยนชนิดของ Level of theory หรือโปรแกรมที่ใช้คำนวณ นอกจากนี้ได้ทำการศึกษาการจำลองทางพลศาสตร์เชิงโมเลกุล ที่เวลา 500 นาโนวินาที เพื่อ ศึกษากลไกการเข้าจับของตัวยับยั้ง Pyrazolopyran(+)-85 และ Pyrazolopyran(+)-86 ต่อเอนไซม์ซีรีนไฮดรอกซีเมทิลทรานเฟอ เรสของพลาสโมเดียม *Plasmodium falciparum* และ *P. vivax* พบว่าประสิทธิภาพในการเข้าจับของ Pyrazolopyran(+)-86 ดีกว่า Pyrazolopyran(+)-85 ประมาณ 2 kcal/mol และพบว่า L124, G128, H129, L130, K139, N356 และ T357 เป็นกรดอะมิโนที่สำคัญ ต่อการเข้าจับของตัวยับยั้ง สำหรับการออกแบบและปรับปรุงโครงสร้างของตัวยับยั้งใหม่ ๆ โดยใช้ข้อมูลจากการศึกษาก่อนหน้า พบว่ากลุ่ม Isopropyl ตรงโครงสร้างแกนหลักของ Pyrazolopyran(+)-86 ควรถูกเปลี่ยนเป็นกลุ่มที่มีประจุเป็นลบ เช่น กลุ่ม Carboxylate เพื่อดึงดูดกับ R371 ซึ่งมีประจุเป็นบวก นอกจากนี้ กลุ่ม Phenolic อื่น ๆ ควรเข้ามาแทนที่วงแหวน Phenyl หรือ Piperidine เพื่อเพิ่มการยึดจับด้วยพันธะไฮโดรเจน นอกจากนี้ ในการหาตัวยับยั้งอื่น ๆ ของเอนไซม์ซีรีนไฮดรอกซี เมทิลทรานเฟอเรส ด้วยวิธีการที่รวดเร็ว เช่น Drug repurposing ได้ถูกนำมาศึกษาในการศึกษานี้ด้วย โดยยาที่ได้รับการรับรอง แล้ว (FDA-approved drugs) ถูกนำมากรองผ่านโครงสร้างของเอนไซม์ซีรีนไฮดรอกซีเมทิลทรานเฟอเรสของพลาสโมเดียม 7 โครงสร้าง พบว่ามีเพียงสาร 8 ชนิดที่พบว่ามีค่าพลังงานการเข้าจับต่ำที่สุดในทุกโครงสร้าง และถูกนำไปทดสอบด้วยวิธีการยับยั้ง เอนไซม์ในห้องปฏิบัติการ โดยผลการทดลองพบว่า Amphotericin B ให้ค่าการยับยั้ง IC_{50} ต่ำที่สุด คือ 106 ± 1 ไมโครโมลาร์ เมื่อ ศึกษาความสามารถในการเข้าจับด้วยวิธีการทางคอมพิวเตอร์ พบว่า Amphotericin B สามารถเข้าจับกับเอนไซม์ซีรีนไฮดรอกซี เมทิลทรานเฟอเรสของพลาสโมเดียมได้ดีเท่ากับตัวยับยั้งกลุ่ม Pyrazolopyran และพบว่า Y63, L124, L130, F134, V141, K251, D258, N259 และ S263 เป็นกรดอะมิโนสำคัญต่อการเข้าจับของ Amphotericin B จากการศึกษาทั้งหมดนี้ สามารถให้ข้อมูลเชิง ลึกของการเข้าจับของตัวยับยั้งกลุ่ม Pyrazolopyran และ ได้โครงสร้างแกนหลักใหม่ของตัวยับยั้งเอนไซม์ซีรีนไฮดรอกซี เมทิลทรานเฟอเรสของพลาสโมเดียม ที่แตกต่างจากตัวยับยั้งอื่น ๆ ก่อนหน้า ซึ่งสามารถใช้เป็นข้อมูลสำหรับการออกแบบยาต้าน มาลาเรียใหม่ ๆ ได้

สาขาวิชา	ชีวสารสนเทศศาสตร์และชีววิทยาเชิง	ลายมือชื่อนิสิต ....
	คอมพิวเตอร์ (สหสาขาวิชา)	
ปีการศึกษา	2565	ลายมือชื่อ อ.ที่ปรึกษาหลัก ....

6087818120 : MAJOR BIOINFORMATICS AND COMPUTATIONAL BIOLOGY

KEYWORD: Plasmodium SHMT, MD simulations, Drug repurposing, Molecular docking, Enzyme-based assay, pyrazolopyrans

Pitchayathida Mee-udorn : CATALYTIC MECHANISM AND INHIBITION OF *Plasmodium* sp. SERINE HYDROXYMETHYLTRANSFERASE BY COMPUTATIONAL SIMULATIONS. Advisor: Assoc. Prof. Dr. THANYADA RUNGROTMONGKOL

Malaria has spread in many countries with a 12% increase in death cases after the COVID-19 pandemic. Over the Greater Mekong subregion, the clinical efficacy of antimalarial drugs has been reduced due to resistance. Target-based approaches on attractive drug targets, such as *Plasmodium* serine hydroxymethyltransferases (SHMTs) exhibiting distinct structure and function as well as kinetic mechanisms from the human enzyme homologue, are highly useful methods to be used for bypassing the present resistance in the field. In this study, the catalytic mechanism of *Plasmodium* SHMT was investigated following the retro-aldol proposed scheme by the combined quantum mechanics/molecular mechanics molecular dynamics (QM/MM MD) simulations. E56 and Y64, residues in the *Plasmodium* SHMT binding pocket, were suggested as a general base and general acid. The PM6 and AM1/D levels of theory were applied to the QM region. However, the reaction was stopped after the formaldehyde occurred. This result indicated the unfavorable of the level of theory on the QM region. Further study should be performed by another method e.g., QUICK package in AMBER20 for HF and DFT calculations. Additionally, the 500-ns MD simulations were carried out to investigate the mode of action of pyrazolopyran(+)-85 and pyrazolopyran(+)-86 with the most attractive inhibition efficiency in *Plasmodium falciparum* and *P. vivax* SHMTs. The results suggested that the binding affinity of pyrazolopyran(+)-86 is more favorable than pyrazolopyran(+)-86 (~ 2 kcal/mol). L124, G128, H129, L130, K139, N356, and T357 are essential residues for inhibitor binding. The rational structure-based drug design suggested that the isopropyl moiety on the pyrazolopyran core should be changed to the negatively charged group (e.g., carboxylate group) for interacting with the positively charged residue R371. Alternatively, the phenolic compounds could be substituted with a phenyl or piperidine ring to promote hydrogen bond formation with the surrounding residues. Moreover, to find other inhibitors with a rapid method, drug repurposing was performed. The FDA-approved drugs were screened over seven *Plasmodium* SHMT structures. The result revealed that only eight potent compounds exhibited the lowest binding energy in all complexes and were then investigated by the enzyme-based assay. The experimental results indicated the lowest IC$_{50}$ value (106 ± 1μM) was observed on *Pf*SHMT by amphotericin B. The binding affinity of amphotericin B (–11.15 ± 0.09 kcal/mol) was in the same range as pyrazolopyran-based inhibitors. Moreover, Y63, L124, L130, F134, V141, K251, D258, N259, and S263 were the key binding residues to amphotericin B. These findings could provide insights into the mode of inhibition of pyrazolopyran-based inhibitors and introduce a new core structure of inhibitor that differs from the previous SHMT inhibitors which could be a rational idea for novel antimalarial drug design.

Field of Study:	Bioinformatics and Computational Biology	Student's Signature ....
Academic Year:	2022	Advisor's Signature ....

ACKNOWLEDGEMENTS

Pitchayathida Mee-udorn

TABLE OF CONTENTS

INTRODUCTION

1.1 Research concept

This research aims to study a novel antimalarial drug target in terms of catalytic mechanism, structural dynamics, inhibition affinity, and new drug design and development by computational approaches. The combined quantum mechanics/molecular mechanics molecular dynamics (QM/MM MD) simulation was performed to investigate the *Plasmodium* Serine hydroxymethyltransferase (SHMT) catalytic mechanism following the retro-aldol proposed scheme on the *P. vivax* SHMT model. The residues in the binding pocket, E56 and Y64 were selected for a general acid and a general base, respectively, to abstract proton and electron in the mechanism. Additionally, the molecular dynamics (MD) simulations of *P. falciparum* and *P. vivax* SHMTs with pyrazolopyran-based inhibitors bound were performed to clarify the dynamics and key binding residues in the SHMT binding pocket which affect the conformational change and binding affinity of this enzyme. The results of MD simulations could provide essential information for new SHMT inhibitors design. Moreover, FDA-approved drugs were included in this research. Screening of known drugs with a new target using computational combined with experimental procedures could reduce time and cost for drug development compared to the traditional one. Therefore, FDA-approved drugs were filtered throughout *Plasmodium* SHMT using the molecular docking method. The potent compound was then investigated by MD simulations. This computational information of *Plasmodium* SHMT with different inhibitor bounds could provide insight into the inhibition mode and essential ideas for novel antimalarial drug design and development. (All manuscripts as part of the thesis for graduation)

1.2 Research rationality

Most of the haemoprotozoan *Plasmodium* species have been described in birds, reptiles, and mammals [1-3]. Infection of *Plasmodium* parasites in humans can lead to one of the worst lethal diseases, malaria, with more than 241 million clinical cases and 627,000 deaths in 2020 [4]. Five *Plasmodium* parasite species were known to cause malaria disease "in

humans", including *P. falciparum, P. vivax, P. malariae, P. ovale*, and *P. knowlesi* [5-8], while the most severe form is caused by *P. falciparum* and *P. vivax* [9, 10]. The malaria parasite is transmitted by specific female Anopheles mosquitoes, are widespread in all major regions of Africa, the Americas, South-East Asia, the Eastern Mediterranean and the Western Pacific [4, 5]. In the last few years, antimalarial drug resistance in *P. falciparum* and *P. vivax* has been reported. Resistances of artemisinin and chloroquine, first-line treatment drugs of malaria, have been a global issue, especially in South-East Asia (*e.g.*, south of Thailand) [4, 11-15]. To resolve antimalarial drug resistance, target-based approaches were introduced for much better understanding of target interaction, potential resistance mechanisms, and toxicological risks [16-20]. Pyrazolopyran-based inhibitors targeting the enzyme serine hydroxymethyltransferase (SHMT) in the dTMP synthesis [19-21], were reported to be candidates for novel antimalarial drugs with similar interaction properties as SHMT substrate, tetrahydrofolate (THF). Specifically, pyrazolopyran(±)-85 and pyrazolopyran(±)-86 had a high binding affinity and low cytotoxicity with IC_{50} in the nanomolar scale of 90 ± 4 nM and 97 ± 1 nM, respectively [20].

SHMT (EC. 2.1.2.1), a pyridoxal-5$'$-phosphate (PLP)-dependent and a ubiquitous enzyme, can be found in all prokaryotes, eukaryotes, and archaebacteria. This enzyme is one of the key enzymes involved in one-carbon metabolism that catalyzes the reversible conversion of serine and THF to glycine and 5,10-methylenetetrahydrofolate (CH_2-THF) (**Fig. 1**) required for the de novo synthesis of purine and pyrimidine nucleotides [21-24]. Since the important role in nucleotide synthesis, expressional correlation of cancer and tumor growth [22, 25] and the unknown physiological significance of the one-carbon unit generated by SHMT, is associated with various diseases [23, 26], SHMT has been attracting attention as a novel biomarker and drug target, especially cancer and malaria [17, 19, 20, 22, 25]. In this study, the malaria parasite SHMTs, *P. falciparum* SHMT (*Pf*SHMT) and *P. vivax* SHMT (*Pv*SHMT) are focused as shown in **Fig. 2**, which have the high similar active site residues (96.7% identity). Thus, computer-aided design of inhibitors and investigation of the protein–inhibitor interactions using classical molecular dynamics (MD) simulations will be employed to propose the more effective inhibitor structures and to study the dynamics behavior of

pyrazolopyran(+)-85 and pyrazolopyran(+)-86 as selective inhibitors toward *Plasmodium* SHMTs with PLP covalently bound to L-serine.
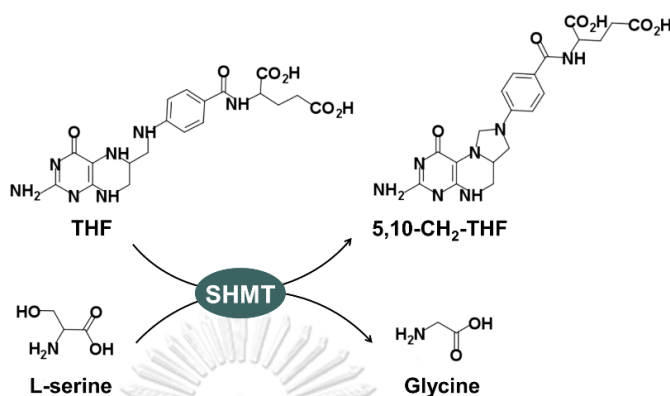
Fig.1 The representative mechanism of serine hydroxymethyltransferase (SHMT) which converts L-serine to glycine and tetrahydrofolate (THF) to 5,10-methylenetetrahydrofolate (5,10-CH$_2$-THF) in thymidylate synthesis cycle [21-24].
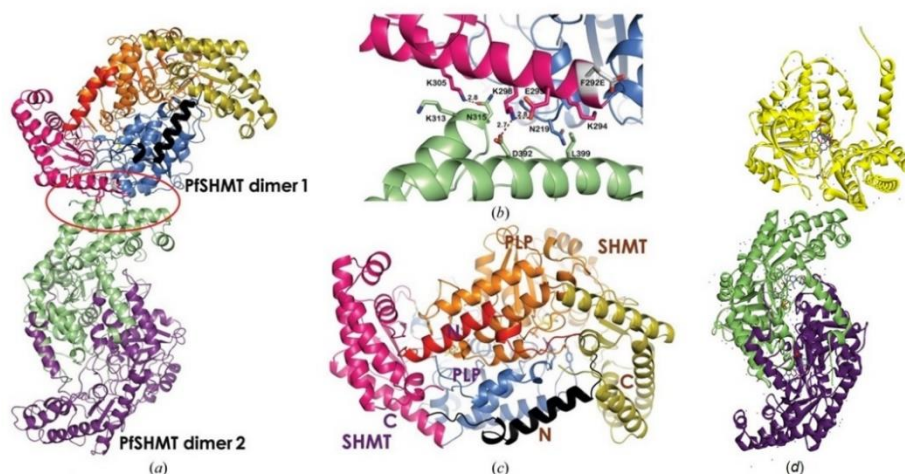
Fig. 2 The X-ray structures of (a) *Pf*SHMT, (b) *Pf*SHMT dimer interface in crystal packing, (c) the three domains of the *Pf*SHMT protomer: N (residues 1–34), large PLP binding (residues 35–290) and C domains (residues 291–442) and PLP are shown in yellow stick representation. (d) The X-ray structure of PvSHMT [27, 28].

Molecular dynamics (MD) simulation is a computational method which mimics what atoms do in real life, assuming a given potential energy function. The simulation will move the atoms and then update the position and velocity of each atom using Newton's law of motion (**Equation 1**):

$$F = ma$$ (**Equation 1**)

where F is force exerting on an atom, m is mass of the atom, and a is the atom's acceleration.

After that, acceleration is calculated from the potential energy function (**Equations 2** to **5**). The calculated acceleration is used to update the next position and velocity following the Newton's law of motion and repeat again and again until the system reaches the setting time.

$$F = -\nabla U(x)$$ (**Equation 2**)

$$U = E_{bonded} + E_{nonbonded}$$ (**Equation 3**)

$$U = \left[E_{(bond-strech)} + E_{(angle-bend)} + E_{(rotate-along-bond)} \right] + \left[E_{vdW} + E_{electrostatic} \right]$$ (**Equation 4**)

$$
\begin{aligned}
U = & \sum_{bonds} \frac{1}{2} K_l \left(l - l_0 \right)^2 + \sum_{angles} \frac{1}{2} K_\theta \left(\theta - \theta_0 \right)^2 \\
& + \sum_{dihedrals} \sum_n \frac{V_n}{2} \left[1 + \cos(\eta\tau) - \gamma \right] \\
& + \sum_{i<j} 4\varepsilon_{ij} \left[\left(\frac{\sigma_{ij}}{r_{ij}} \right)^{12} - \left(\frac{\sigma_{ij}}{r_{ij}} \right)^6 \right] \\
& + \sum_{H-bond} \left[\frac{C_{ij}}{r_{ij}} - \frac{D_{ij}}{r_{ij}} \right] \\
& + \sum \frac{q_i q_j}{\varepsilon r_{ij}} + \frac{1}{EE_{scale}} \sum_{i<j}^{1,4-terms} \frac{q_i q_j}{D r_{ij}}
\end{aligned}
$$ (**Equation 5**)

Numerous numerical algorithms have been developed for integrating the equations of motion, such as Verlet algorithm, Leap-frog algorithm, Velocity Verlet algorithm, Beeman's algorithm, Geer Predictor-corrector, and so on. For the AMBER program we will use here, the Leap-frog algorithm (**Equation 6**) is the main method, which is used to calculate the movement of atoms.

$$v(t) = \frac{1}{2}\left[v\left(t + \frac{1}{2}\Delta t\right) + v\left(t - \frac{1}{2}\Delta t\right)\right]$$ (**Equation 6**)

Along the MD simulation time, all the trajectories are preliminary analyzed by root-mean-square deviation (RMSD) (**Equation 7**) to indicate the stability of the system. Then, the trajectories at the equilibrium state are selected for further structural analyses, such as protein-ligand interactions, interaction energy, and so forth.

$$RMSD = \sqrt{\frac{1}{n}\sum_{i=1}^{n} d_i^2}$$ (**Equation 7**)

where the RMSD is performed over the n pairs of equivalent atoms and di is the distance between the two atoms in the *i*-th pair. Note that RMSD can be calculated for any type and subset of atoms; for example, Cα atoms of the entire protein, Cα atoms of all residues in a specific subset (*e.g.*, the transmembrane helices, binding pocket, or a loop), all heavy atoms of a specific subset of residues, or all heavy atoms in a small-molecule ligands [27, 28].

Screening of known drugs with a new protein target using drug repurposing approaches is a popular rapid method which reduce time, investment, and risk of use compared to the traditional processes (**Fig. 3**). Drug repurposing could provide new drugs or new inhibitor cores of target protein by using a computational or a simple experiment procedure [29, 30]. Therefore, finding other new potent inhibitors of *Plasmodium* SHMTs from FDA-approved drugs by drug repurposing method will be applied in this work.
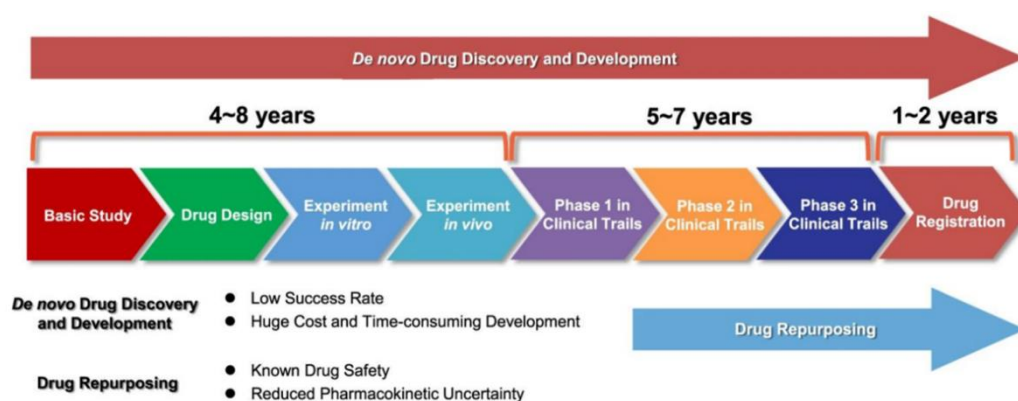
Fig. 3 Drug repurposing compared to the traditional drug discovery which take around more than ten years to complete [29].

The attractive properties of *Plasmodium* SHMT for the new antimalarial drug target motivate the more investigation by experimental and computational methods. However, the catalytic mechanism of SHMT remains unclear. The catalytic mechanism of SHMT were proposed by two schematic representations: retro-aldol cleavage mechanism and direct-displacement mechanism, as shown in **Fig. 4** [31]. The evidences suggested that SHMT mechanism are most likely to proceed via the retro-aldol cleavage mechanism [32-34]. Moreover, mutagenic studies reported that mutation of E75 of human and rabbit cytosolic SHMT, E74 of sheep liver cytosolic SHMT and Y83 of human and rabbit cytosolic SHMT and Y82 of sheep liver cytosolic SHMT in the enzyme binding pocket drastically reduced the SHMT activity (more than 300 times) [33, 34]. Therefore, E and Y in the binding pocket played the pivotal role in the SHMT catalytic mechanism, but the exact mechanism needs to be further investigated.
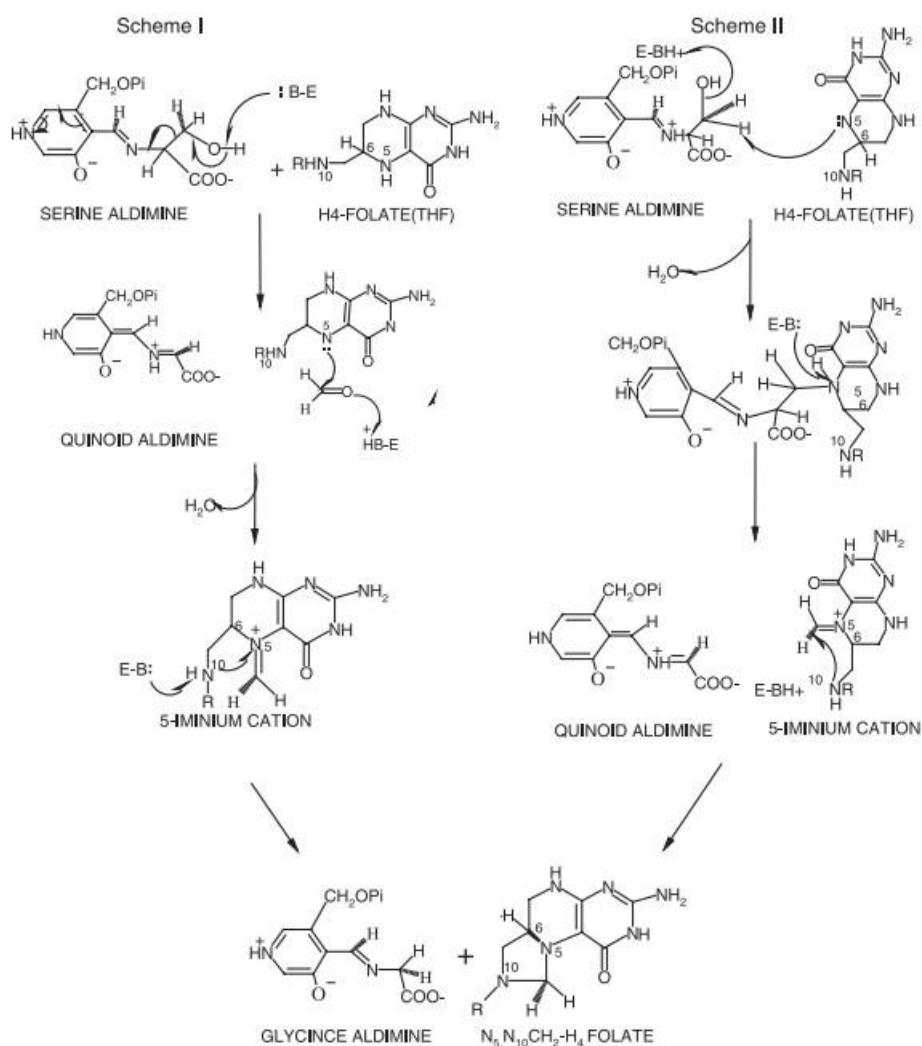
Fig. 4 Schematic representation of the mechanisms proposed for the reaction catalyzed by SHMT. Retro-aldol cleavage mechanism (Scheme I) and Direct-displacement mechanism (Scheme II) [31].

The QM/MM MD simulations method allows a model system to be split into different regions that are computed by different theoretical levels, high-level (HL) layer or QM region: a small part of the system and low-level (LL) layer or MM region: the larger part (**Fig. 5**) [35]. At the HL layer, the atoms were treated with the QM method using the level of theory for the calculations, and another layer was calculated with molecular mechanics (MM) level *e.g.*, the AMBER force field. Within the hybrid QM/MM method, it contains three classes of interactions: interactions between atoms in the QM region, between atoms in the MM region,

and interactions between QM and MM atoms. The interactions within the QM and MM regions are relatively straightforward to describe, that is at the QM and MM level, respectively. However, the interactions between the two subsystems are more difficult to describe, and several approaches have been proposed. These approaches can be roughly divided into two categories: subtractive (**Equation 8**) and additive (**Equation 9**) coupling schemes.

$$V_{QM/MM} = V_{MM} (MM+QM) + V_{QM} (QM) - V_{MM} (QM) \qquad \textbf{(Equation 8)}$$

$$V_{QM/MM} = V_{QM} (QM) + V_{MM} (MM) + V_{QM-MM} (QM + MM) \qquad \textbf{(Equation 9)}$$

The terms QM and MM stand for the atoms in the QM and MM subsystems, respectively [35-37].

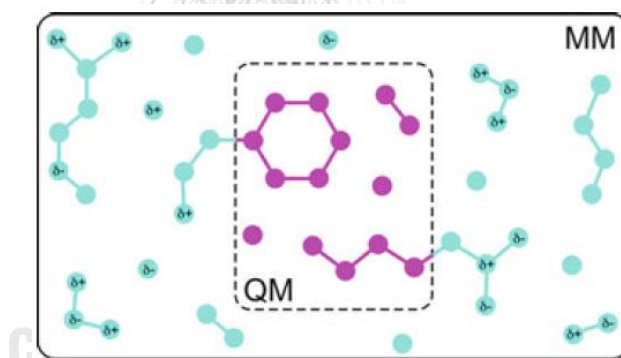**Fig. 5** Illustration of the QM/MM concept. A small region, in which a chemical reaction occurs and therefore cannot be described with a force field, is treated at a sufficiently high level of QM theory. The remainder of the system is modelled at the MM level [35].

1.3 Research objectives

i) To understand the retro-aldol cleavage mechanism of *P. vivax* serine hydroxymethyl-transferase using the combined QM/MM MD approach

ii) To determine the binding interactions of pyrazolopyran derivatives on *P. vivax* and *P. falciparum* serine hydroxymethyltransferase using molecular dynamics (MD) simulations

iii) To screen new potent compounds from FDA-approved drugs targeting *P. vivax* and *P. falciparum* serine hydroxymethyltransferase using drug repurosing method and investigate the binding interactions of a potent compound from drug screening on *P. falciparum* serine hydroxymethyltransferase using molecular dynamics (MD) simulations

1.4 Scope of the research

i) The retro-aldol catalytic mechanism of *Plasmodium vivax* SHMT was investigated by the combined quantum mechanics/molecular mechanics molecular dynamics (QM/MM MD) simulations

ii) The binding interactions of pyrazolopyran(+)-85 and pyrazolopyran(+)-86 on *P. vivax* and *P. falciparum* serine hydroxymethyltransferase were studied using molecular dynamics (MD) simulations, and the rational design of pyrazolopyran‑based inhibitors was investigated by molecular docking.

iii) The 2,509 FDA-approved drugs from the Drugbank database were screen using five crystal structures from PDB database and two structures from previous MD simulations of *P. vivax* and *P. falciparum* serine hydroxymethyltransferase.

1.5 Expected beneficial outcome(s) from the thesis

Molecular information of *Plasmodium* sp. serine hydroxymethyltransferase will be used as the supportive data for novel antimalarial drug development in the future.

LIST OF PROJECTS

This thesis contains a general summary (introduction, some background information, and conclusions) and the following paper which are referred to in the text by their roman number.

Project I: Retro-aldol reaction of *Plasmodium* serine hydroxymethyltransferases by the combined QM/MM MD simulations

Project II: Manuscript I, Structural dynamics and *in silico* design of pyrazolopyran-based inhibitors against *Plasmodium* serine hydroxymethyltransferases

Project III: Manuscript II, *in silico* and *in vitro* potential of FDA-approved drugs for antimalarial drug discovery against *Plasmodium* serine hydroxymethyltransferases

จุฬาลงกรณ์มหาวิทยาลัย

CHULALONGKORN UNIVERSITY
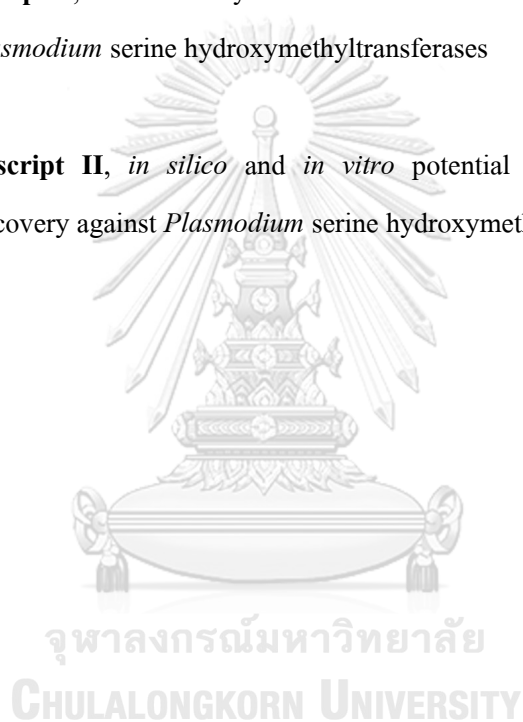
CHAPTER I

PROJECT I

Retro‑aldol reaction of *Plasmodium* serine hydroxymethyltransferases by the combined QM/MM MD simulations

Pitchayathida Mee-udorn[a], Bodee Nutho[b] and Thanyada Rungrotmongkol[a,c]*

[a]Program in Bioinformatics and Computational Biology, Graduate School, Chulalongkorn University, Bangkok 10330, Thailand

[b]Department of Pharmacology, Faculty of Science, Mahidol University, Bangkok 10400, Thailand

[c]Biocatalyst and Environmental Biotechnology Research Unit, Department of Biochemistry, Faculty of Science, Chulalongkorn University, Bangkok 10330, Thailand

E-mail address: t.rungrotmongkol@gmail.com, thanyada.r@chula.ac.th

Phone: +66-2218-5426. Fax: +66-2218-5418

Incomplete project due to the resource limitations and unfavorable conditions and method

1. Introduction

Plasmodium serine hydroxymethyltransferase is a new promising target protein for novel antimalarial drug development because of its attractive role in the dTMP cycle, which is involved in the DNA/RNA biosynthesis [19, 20, 22]. Recently, most studies reported new inhibitors of the SHMT enzyme [21, 38, 39]. However, the exact catalytic mechanism remains unclear. The SHMT mechanism was proposed by two schematic representations: the retro-aldol cleavage mechanism (Scheme I) and the Direct-displacement mechanism (Scheme II) [31]. The evidences suggested that the SHMT mechanism is most likely to proceed via the retro-aldol cleavage mechanism [32-34]. Therefore, the catalytic mechanism of *Plasmodium vivax* SHMT (*Pv*SHMT) will be investigated following the retro-aldol mechanism in this study. E56 and Y64, the residues in the binding pocket of *Pv*SHMT, will be selected as a general acid and a general base for the retro-aldol reaction because of their important role in the SHMT catalytic mechanism [33, 34]. Moreover, the study will be performed by the popular computational method: the combined quantum mechanics/molecular mechanics molecular dynamics (QM/MM MD) simulation [36, 37, 40, 41].

The complete mechanism was shown in **Fig. 1.1**. The rate-limiting step of this mechanism was the first step of the reaction [37, 40]. Y64 in a deprotonated form will abstract a proton from PLS cofactor which is in the external aldimine with the L-serine (E-Ser) form. Then, OH of Y64 will make a covalent bond with H3 of PLS. Meanwhile, C9…C11 of PLS will be broken spontaneously to form a formaldehyde (CH_2O), which will attach to tetrahydrofolate (THF) substrate in the next step of the reaction. To create the 5,10-CH_2-THF product, E56 will be a key residue in this step. The proton in the forming of 5,10-CH_2-THF will be attached to E56 which was previously abstracted by Y64 in a deprotonated form. Finally, 5,10-CH_2-THF, H_2O, and external aldimine with the glycine (E-Gly). To confirm the role of E56 and Y64 in the retro-aldol catalytic mechanism, the E56A mutation complex will be investigated. The reaction should occur as shown in **Fig. 1.2**. The formaldehyde will be created, but the reaction could not go to the final step. Additionally, for the Y64 mutation, the reaction might not be performed due to the lack of a general base at the first step of the mechanism (**Fig. 1.3**).
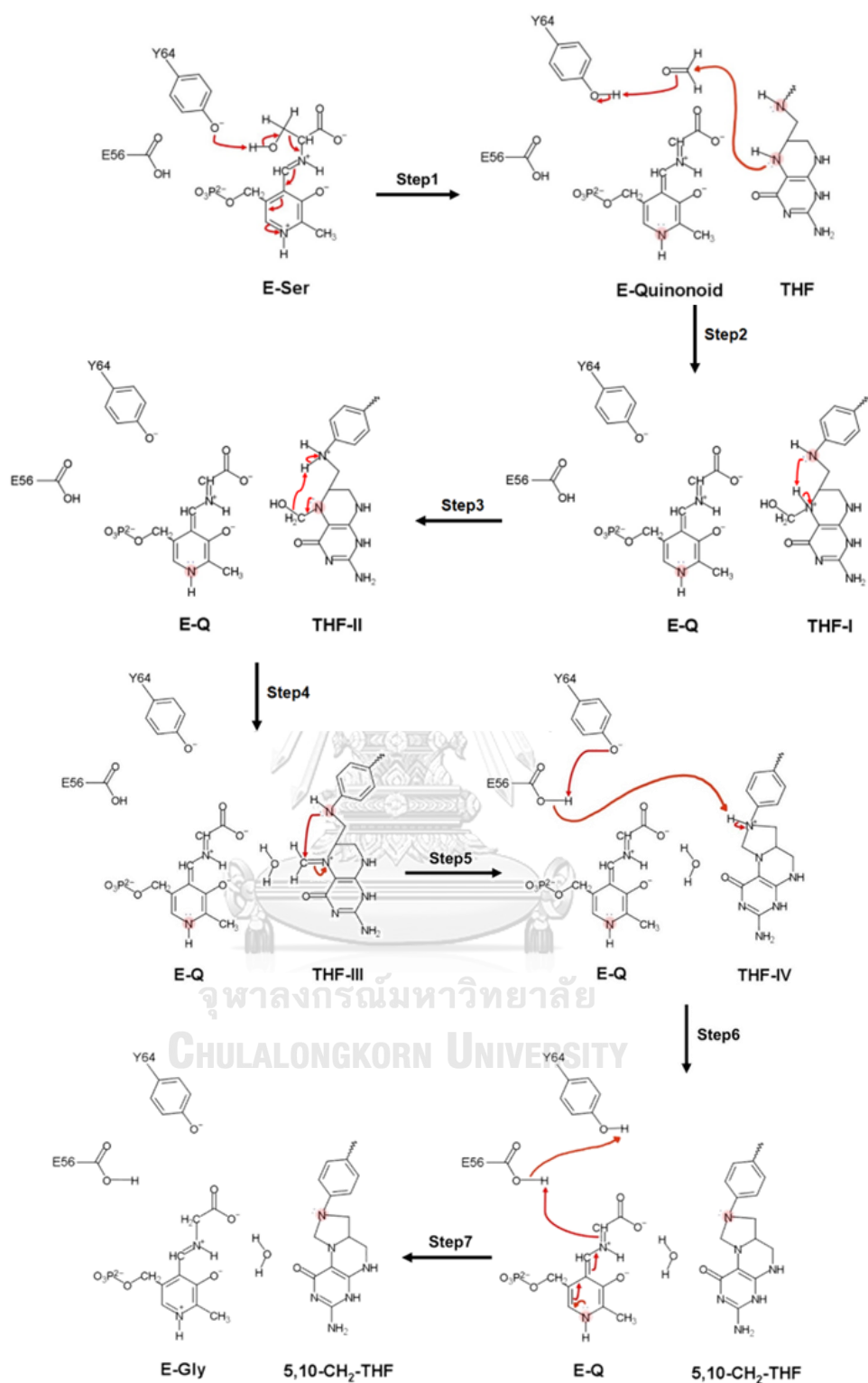
Fig. 1.1 The completed proposed retro-aldol catalytic mechanism of *Plasmodium vivax* serine hydroxymethyltransferase (SHMT). The key residues E56 and Y64 played important roles in the proton and electron abstraction in the reaction.
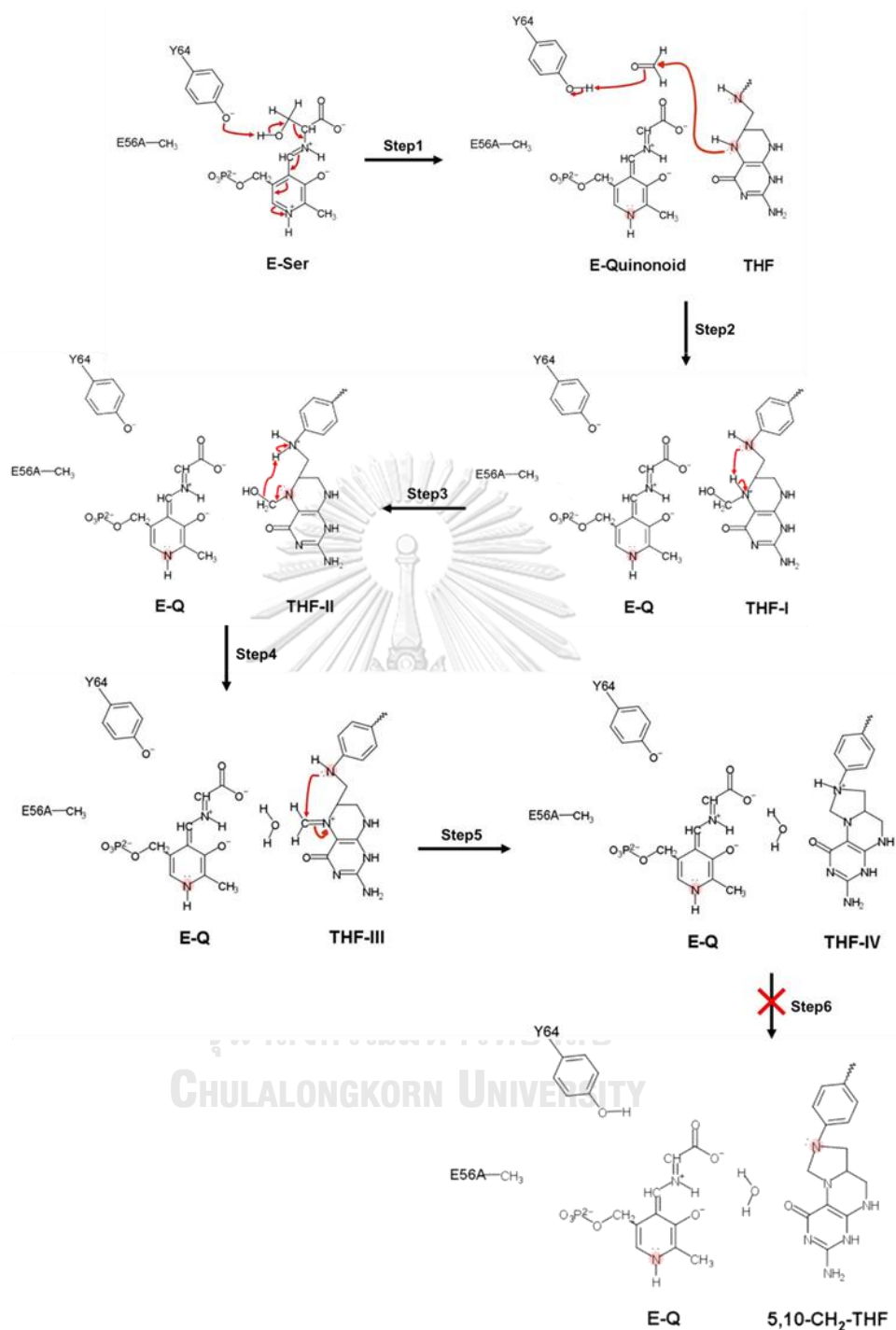
Fig. 1.2 The mechanism of E56A complex of *Plasmodium vivax* serine hydroxymethyltransferase (SHMT). The reaction can be performed, but the 5,10-CH$_2$-THF product could not form due to the mutation of a general acid, E56A.
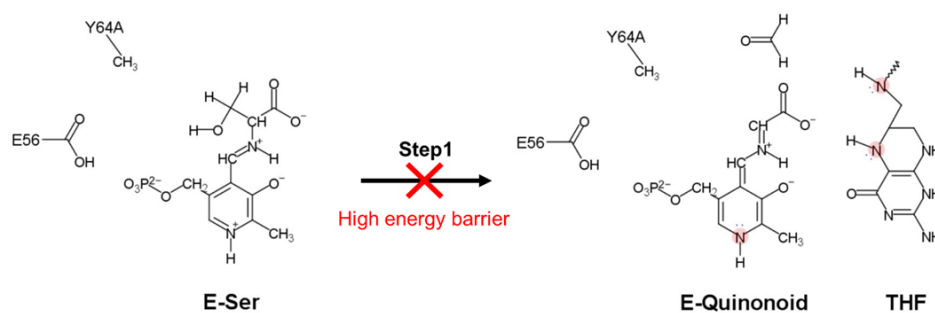
Fig. 1.3 The proposed mechanism of the mutation of Y64A complex. A general base could not abstract proton in the reaction. Therefore, the catalytic mechanism could not be performed due to the mutation of a general base, Y64A.

2. Materials and methods

2.1 Structure preparation for the QM/MM MD simulations

The catalytic mechanisms of *Plasmodium* SHMT were studied on two systems *i.e.*, wild-type and E56A complexes. The crystal structure of *P. vivax* SHMT (*Pv*SHMT) with D-serine and folinic acid bound (PDB entry 4OYT [42]) was selected as the initial structure for the QM/MM MD calculation of the wild-type system. The complex was modified by the deletion of D-serine and changing of folinic acid to THF substrate. The Schiff base form of pyridoxal 5'-phosphate cofactor with L-serine bound (PLS) was then superimposed to the modified complex from another crystal structure: *Pv*SHMT/PLS (PDB entry 4PFN [42]). A general base, Y64, was in the deprotonated form in wild-type and E56A complexes. The starting model (*Pv*SHMT/PLS/THF) was then relaxed and searched for the optimum reaction coordinates by the 60-ns MD simulation following the standard procedure [43-45] using the AMBER16 program [46]. For the E56A mutation complex, E56 from the wild-type complex was mutated to alanine using the Discovery Studio Visualizer [47]. Then, the 60-ns MD simulation of E56A *Pf*SHMT/PLS/THF was performed to relax the structure and find the optimum coordinates for the QM/MM MD simulations.

2.2 The QM/MM MD simulations of *Plasmodium* SHMT

The initial structure for the QM/MM MD simulation of wild-type and E56A systems was selected from the 60-ns MD snapshot with the optimum reaction coordinates of d3 and d4 (d3 = 1.5 Å and d4 = 3.5 Å) as shown in **Fig. 1.4**. Then, the starting structure of each system was heated from 10 K to 300 K for 20 ps with the 96 and 98 atoms (**Fig 1.5**) of the QM region in the *Pv*SHMT binding pocket. The QM region was treated with the PM6 and AM1/D levels of theory with a force of 300 kcal/mol/Å^2, and the MM region was treated with the AMBER force field. Then, the system was equilibrated for 50 ps and moved to the production phase for 50 ps. After that, the QM/MM MD simulation was performed using the umbrella sampling method of the AMBER16 program [46] by setting d1, d2, and d3 as the first reaction coordinates (**Fig 1.4**). The reaction started with 1.0 Å from the summation of break bond lengths (d1+d2) minus make bond length (d3). The QM/MM MD energy profile of each complex was extracted and predicted by the weighted histogram analysis method (WHAM) [48].

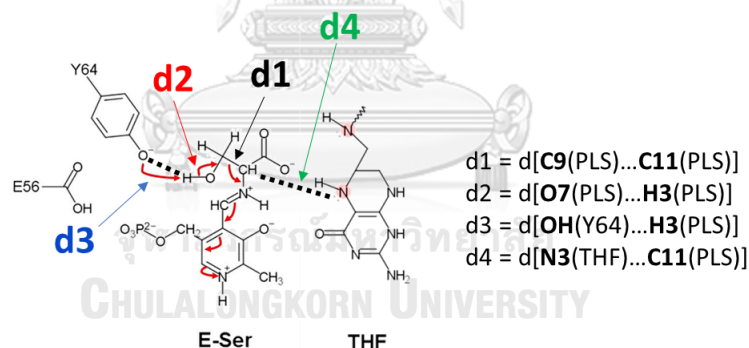
Fig 1.4 The reaction coordinates for QM/MM MD structure of wild-type and E56A systems where d1 is [C9(PLS)…C11(PLS) = 1.5 Å], d2 is [O7(PLS)…H3(PLS) = 1.0 Å], d3 is [OH(Y64)…H3(PLS) = 1.5 Å] and d4 is [C11(PLS)…N3(THF) = 3.5 Å].

Wild-type: 96 atoms   E56A: 98 atoms
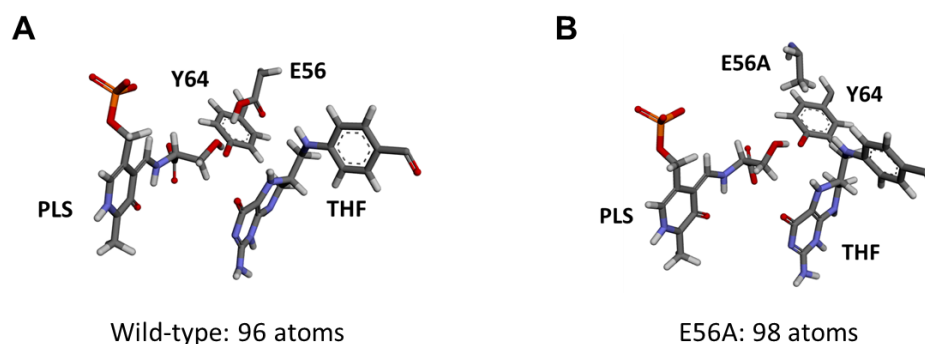
Fig 1.5 The QM region of (**A**) wild‑type and (B) E56A systems, which was in the binding pocket of *Pv*SHMT.

3. Results and Discussion

3.1 The retro‑aldol mechanism of *Plasmodium* SHMT

The retro‑aldol catalytic mechanism of *P. vivax* SHMT was investigated by the combined QM/MM MD simulation. The studied systems were the wild‑type and E56A complexes with PLS and THF bound. E56 and Y64 were selected for a general acid and general base, respectively, which abstract the proton and electron in the reaction. Y64 was in the deprotonated form in both complexes, while E56 was mutated to alanine in E56A system. For the wild‑type complex with PM6 level of theory, the d2 [O7(PLS)…H3(PLS)] was broken and H3 formed a new covalent bond to O7(Y64). However, the d1 [C9(PLS)…C11(PLS)] was not broken as expected in **Fig. 1.6A**. Therefore, formaldehyde (CH_2O) could not be formed in this system (**Fig. 1.6B**).

Fig. 1.6 (**A**) The QM/MM MD snapshot of the QM region of wild-type complex which was treated by the PM6 level of theory. The H3(PLS) was broken from O7(PLS) and formed a new bond to OH(Y64). (**B**) The first 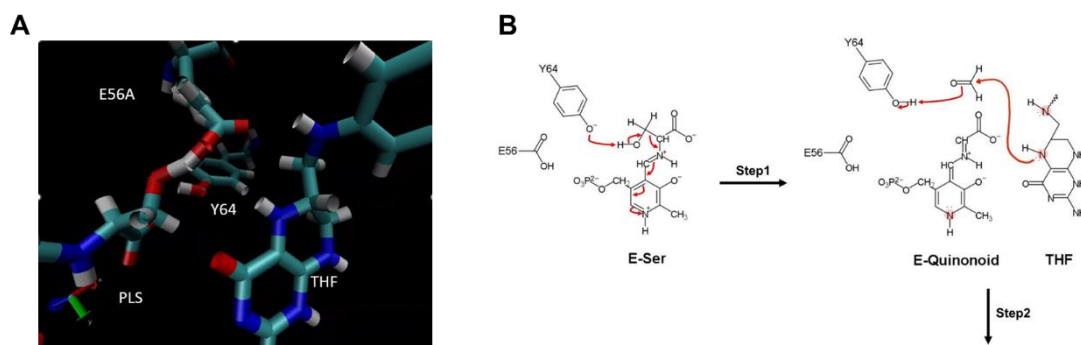step of the complete proposed retro-aldol mechanism which formaldehyde (CH_2O) was created after the breaking of H3(PLS)…O7(PLS).

The AM1/D level of theory was then treated to the QM region of the wild-type complex. The first step of the reaction was completed as the proposed scheme. The H3(PLS)…O7(PLS) was broken and a new covalent bond of H3(PLS)…O7(PLS) was formed. The C9(PLS)…C11(PLS) was then broken spontaneously, and formaldehyde was created in **Fig. 1.7A**. However, the second and third steps of the reaction in **Fig. 1.7B** did not happen. The formaldehyde could not move to form a new covalent bond to N3 of THF substrate. Therefore, the reaction was stuck at this step for the wild-type complex.
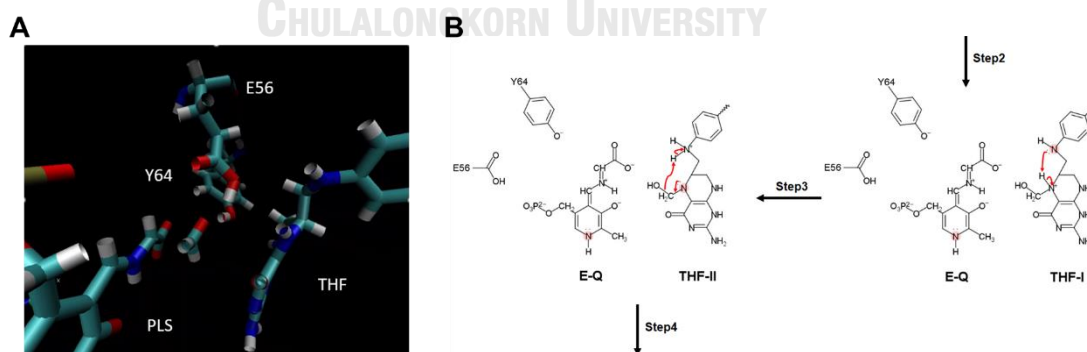

Fig. 1.7 (**A**) The QM/MM MD snapshot of the QM region of wild-type complex which was treated by the AM1/D level of theory. The first step of the reaction was completed, but formaldehyde (CH_2O) could not attach to THF substrate in the second step of the reaction. (**B**) In the second and third steps of the retro-aldol mechanism, H3(PL) was broken from OH(Y64) and

formed a new covalent bond to formaldehyde (CH_2O). The CH_2OH was then moved to form a new covalent bond to N3(THF).

The E56A mutation complex was studied to confirm the role of E56 and Y64 as a general acid and a general base. The QM/MM MD simulation was conducted following the same condition as the wild-type complex. The QM region was treated by the PM6 level of theory with a force of 300 kcal/mol/$Å^2$. **Fig. 1.8A** showed that the first step of the retro-aldol mechanism was performed and completed. H3(PLS) was broken from O7(PLS) and formed a covalent bond to OH(Y64). Then, C9(PLS)…C11(PLS) was spontaneously broken, and formaldehyde was conducted. However, formaldehyde moved back to form covalent bonds to OH(Y64) and O7(PLS) (**Fig. 1.8B**). Therefore, the forming of THF and formaldehyde in the second step could not be found in this mutated system.
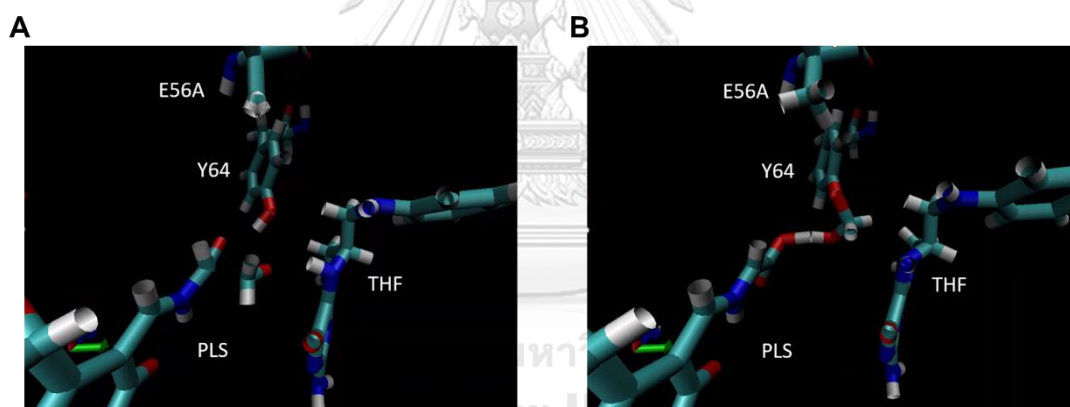
Fig. 1.8 The QM/MM MD snapshot of the QM region of the E56A complex which was treated by the PM6 level of theory. (**A**) The first step of the reaction was completed, and formaldehyde (CH_2O) was created. (**B**) Formaldehyde from the first step moved back to form covalent bonds to OH(Y64) and O7(PLS). Therefore, the reaction was stuck and could not go to the second step.

3.2 The alteration of a general base and a general acid of the catalytic mechanism

To confirm the key role of E56 and Y64 as a general acid and a general base in the retro-aldol mechanism, E56 was set as a general base and Y64 was set as a general acid in the QM/MM MD simulation. In **Fig. 1.9A**, Y64 was protonated, and the QM region was treated by the PM6

level of theory with the same force as the previous complexes. The results in **Fig. 1.9B** showed that the first reaction step could not be performed as the proposed mechanism. Many parts of the molecules in the QM region were broken. These might be the effect of the wrong selection of a general acid and a general base of the reaction. Therefore, the study of the alteration complex confirmed that E56 and Y64 should be the correct general acid and a general base as mentioned in the wild-type system.

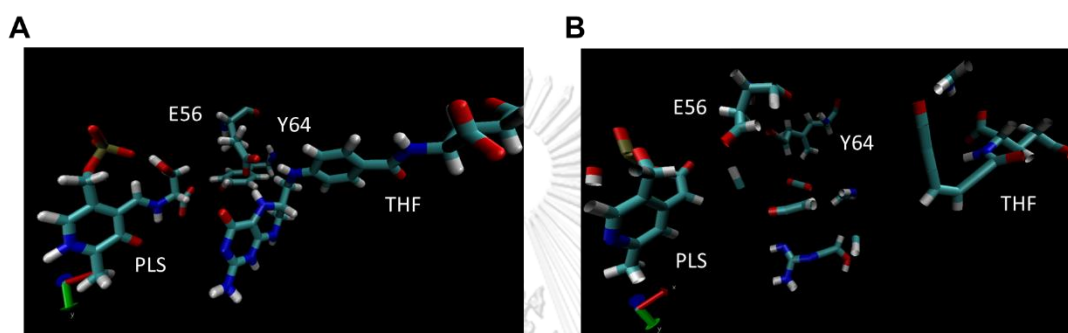**Fig. 1.9** (**A**) The QM region of the alteration of the retro-aldol mechanism in which Y64 was protonated and selected as a general acid, and E56 was selected as a general base. (**B**) The QM/MM/MD snapshot of the alteration complex. The first step of the reaction could not be performed, and many parts of the QM region were broken.

จุฬาลงกรณ์มหาวิทยาลัย

CHULALONGKORN UNIVERSITY

4. Conclusions

The catalytic mechanism of *Plasmodium* SHMT was performed by the QM/MM MD simulation following the proposed retro-aldol mechanism. E56 and Y64 were selected as a general acid and a general base to abstract proton and electron in the wild-type reaction. Moreover, the mutation of E56 to alanine was conducted to confirm the role of E56 and Y64 in the catalytic mechanism. The PM6 and AM1/D levels of theory were treated to the QM region of the wild-type complex. The first step reaction could be found in both levels of theory. However, the reaction could not go to the second and third steps of the mechanism. For the E56A mutation system, the PM6 level of theory was treated to the QM region. The first step of the reaction was found, but the formaldehyde could not form a covalent bond with THF substrate. Therefore, the second and third steps of the reaction could not occur. These unsuccess mechanisms might be the effects of unfavorable conditions and the wrong reaction coordinate to the QM region of wild-type and E56A complex. To confirm the role of E56 and Y64 as a general acid and a general base in the retro-aldol mechanism, alteration of the wild-type system was performed. E56 was chosen as a general base and Y64 was selected as a general acid with a protonated form. The reaction could not be conducted. Many parts of the molecules in the QM region were broken. These results could refer to the key role of E56 and Y64 in the catalytic mechanism as mentioned in the wild-type system.

CHAPTER II

PROJECT II: Manuscript I

Structural dynamics and *in silico* design of pyrazolopyran‑based inhibitors against *Plasmodium* serine hydroxymethyltransferases

Pitchayathida Mee-udorn[a], Bodee Nutho[b], Romchalee Chootrakool[c], Somchart Maenpuen[d], Ubolsree Leartsakulpanich[e], Penchit Chitnumsub[e], and Thanyada Rungrotmongkol[a,c]∗

[a]Program in Bioinformatics and Computational Biology, Graduate School, Chulalongkorn University, Bangkok 10330, Thailand

[b]Department of Pharmacology, Faculty of Science, Mahidol University, Bangkok 10400, Thailand

[c]Biocatalyst and Environmental Biotechnology Research Unit, Department of Biochemistry, Faculty of Science, Chulalongkorn University, Bangkok 10330, Thailand

[d]Department of Biochemistry, Faculty of Science, Burapha University, Chonburi 20131, Thailand

[e]National Center for Genetic Engineering and Biotechnology, 113 Thailand Science Park, Bangkok 12120, Thailand

E-mail address: t.rungrotmongkol@gmail.com, thanyada.r@chula.ac.th

Phone: +66-2218-5426. Fax: +66-2218-5418

Structural dynamics and *in silico* design of pyrazolopyran-based inhibitors against *Plasmodium* serine hydroxymethyltransferases

Pitchayathida Mee-udorn[a], Bodee Nutho[b], Romchalee Chootrakool[c], Somchart Maenpuen[d], Ubolsree Leartsakulpanich[e], Penchit Chitnumsub[e], and Thanyada Rungrotmongkol[a,c]∗

[a]Program in Bioinformatics and Computational Biology, Graduate School, Chulalongkorn University, Bangkok 10330, Thailand

[b]Department of Pharmacology, Faculty of Science, Mahidol University, Bangkok 10400, Thailand

[c]Biocatalyst and Environmental Biotechnology Research Unit, Department of Biochemistry, Faculty of Science, Chulalongkorn University, Bangkok 10330, Thailand

[d]Department of Biochemistry, Faculty of Science, Burapha University, Chonburi 20131, Thailand
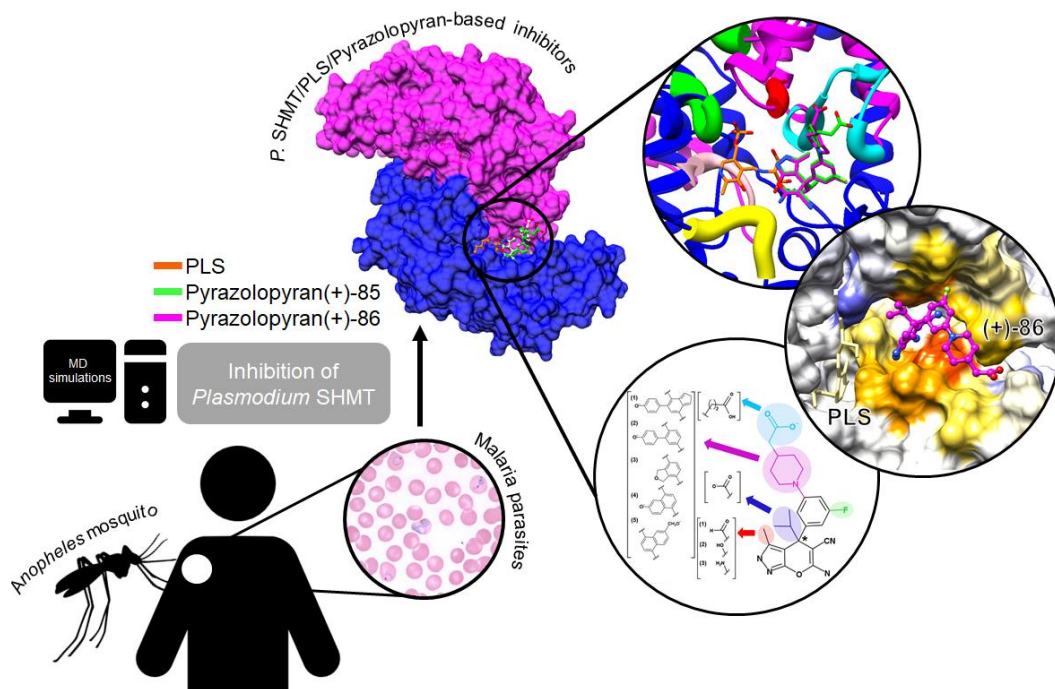
[e]National Center for Genetic Engineering and Biotechnology, 113 Thailand Science Park, Bangkok 12120, Thailand

E-mail address: t.rungrotmongkol@gmail.com, thanyada.r@chula.ac.th

Phone: +66-2218-5426. Fax: +66-2218-5418

Graphical Abstract

Abstract

The clinical efficacy of antimalarial drugs has been reduced due to resistance spreading over many parts of the world. Target-based approaches on attractive drug targets, such as *Plasmodium* serine hydroxymethyltransferases (SHMTs) exhibiting distinct structure and function as well as kinetic mechanisms from the human enzyme homologue, are highly useful methods to be used for bypassing the present resistance in the field. Herein, 500-ns molecular dynamics (MD) simulations were carried out to investigate the mode of action of pyrazolopyran(+)-85 and pyrazolopyran(+)-86 with the most attractive inhibition efficiency in *Plasmodium falciparum* and *P. vivax* SHMTs (in the Schiff base form of PLP-L-serine (PLS) bound enzyme). The binding free energy results indicated the binding affinity of pyrazolopyran(+)-86 to *Plasmodium* SHMTs that is more favorable than pyrazolopyran(+)-85 by ~2 kcal·mol^{-1}, supported by the stronger ligand-protein hydrogen bonding and the lower solvent accessibility within the enzyme active site. According to the per-residue decomposition free energy analysis, residues L124, G128, H129, L130, K139, N356, and T357 are essential for inhibitors binding. By the rational structure-based drug design, the isopropyl moiety on the pyrazolopyran core should be changed to the negatively charged group (*e.g.*, carboxylate group) for interacting with the positively charged residue R371. Alternatively, the phenolic compounds could be substituted with a phenyl or piperidine ring to promote hydrogen bond formation with the surrounding residues. Therefore, our findings presented here provide insights into the mode of inhibition of pyrazolopyran-based inhibitors and rational ideas for designing novel antimalarial drugs targeting *Plasmodium* SHMTs.

Keywords: Serine hydroxymethyltransferase, *Plasmodium falciparum*, *Plasmodium vivax*, pyrazolopyrans, computational simulations

1. Introduction

Malaria is a life-threatening disease caused by *Plasmodium* parasite. WHO estimated 241 million clinical cases and 627,000 deaths in 2020 [4]. Five *Plasmodium* parasite species cause malaria in humans, *P. falciparum*, *P. vivax*, *P. malariae*, *P. ovale*. and *P. knowlesi* [5-8]. *P. falciparum* and *P. vivax* culminate in the severe form of malaria worldwide [9, 49]. The malaria parasite is transmitted by female *Anopheles* mosquitoes, widespread in several major regions of Africa, America, South-East Asia, the Eastern Mediterranean, and the Western Pacific [4, 5]. Antimalarial drug resistances to the first-line drugs artemisinin, chloroquine and antifolate drugs have been reported in many parts of the world, especially in South-East Asia [4, 11-16, 50-53]. These mainly come from parasite mutations at either the drug targets or transporters [50-52]. To delay the development of resistance, new effective drugs against novel drug targets have been recently studied [53]. Target-based approach can be used to screen compounds with a better understanding of protein-ligand interactions. A more precise compound mimicking very similar interactions to the substrate can be designed so as parasites cannot bear to compromise via mutation thus drug resistance would be difficult to occur [16-20].

Various types of compounds have been proposed as promising drug candidates for tackling different targets of malaria parasites [21, 38, 39]. Recently, two pyrazolopyran-based inhibitors, namely pyrazolopyran(+)-85 and pyrazolopyran(+)-86 (**Fig. 2.1A**), were considered as the most attractive inhibitors targeting *Plasmodium* (*P. falciparum* and *P. vivax*) serine hydroxymethyl-transferases (SHMTs) [20], which are pyridoxal-5′-phosphate (PLP)-dependent enzymes (EC 2.1.2.1). SHMT catalyzes the reversible conversion of L-serine and (6*S*)-tetrahydrofolate (THF) to glycine and 5,10-methylenetetrahydrofolate (CH_2-THF) in the deoxythymidylate (dTMP) synthesis cycle (**Fig. 2 . 1B**) [19, 20, 22]. Important for dTMP synthesis in DNA replication, *Plasmodium* SHMT has been validated for its essential role in parasite cell growth and development [54]. Although a high similarity of *Plasmodium* and human SHMT active site is observed (80%), the overall structure, kinetic mechanisms, biochemical and biophysical properties are significantly different [42, 55-58]. These make *Plasmodium* SHMT attractive as a new antimalarial drug target. Both pyrazolopyran(+)-85 and (+)-86, occupying the

space of THF substrate, effectively inhibited *Pf*SHMT with the half-maximal inhibitory concentration (IC_{50}) values of 90 ± 4 and 97 ± 1 nM, respectively [20].
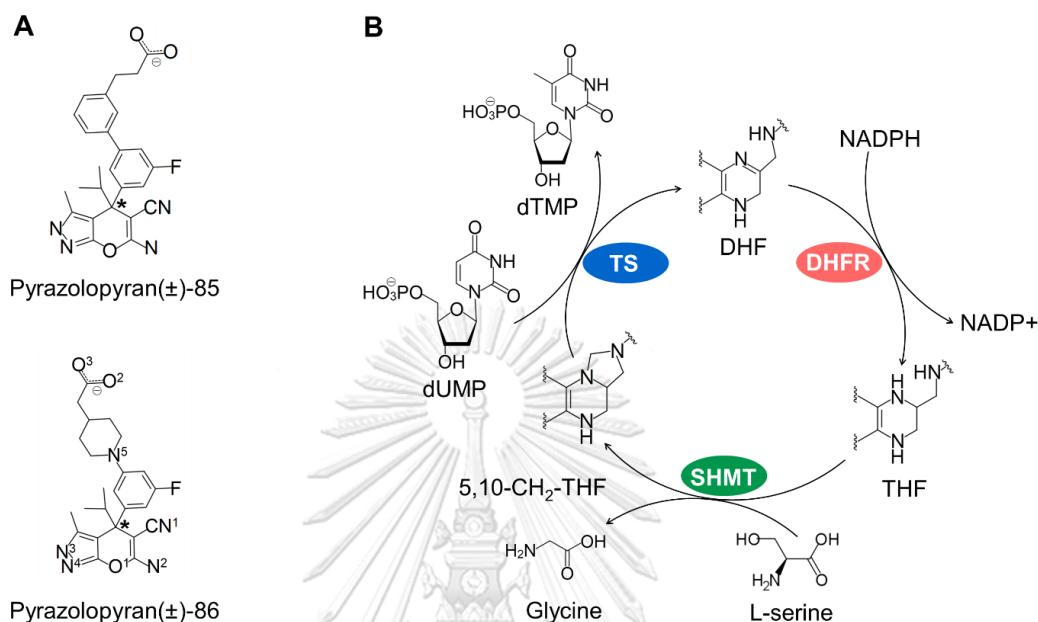

Fig. 2.1 (**A**) Chemical structures of pyrazolopyran($\pm$)-85 and ($\pm$)-86, the competitive inhibitors of THF-dependent SHMT reaction. The asterisk (*) indicates a chiral center of enantiomers. (**B**) The schematic representation of the enzymes involved in dTMP biosynthesis, including thymidylate synthase (TS), dihydrofolate reductase (DHFR) and serine hydroxymethyl-transferase (SHMT), and their relevant substrates of *Plasmodium* sp.

The 2.3 and 2.1 Å cocrystal structures of *Pv*SHMT/Gly/pyrazolopyran(+)-85 (PDB entry 5GVN [20]) and *Pv*SHMT/Gly/pyrazolopyran(+)-86 (PDB entry 5YFZ [59]) ternary complexes reveal several crucial residues such as E56, Y63, L124, G128 and K139, which are involved in the binding of pyrazolopyran(+)-85 and (+)-86 [20, 59]. Although the structure elucidation can explain how pyrazolopyran-based derivatives inhibit *Plasmodium* SHMTs, these complex structures may not represent an overall trajectory direction of the SHMT reactions as they only mimic a reverse direction of the reactions. In the present study, the molecular dynamics (MD) simulations on the pyrazolopyran(+)-85 and (+)-86 binding with *Pf*SHMT and *Pv*SHMT in the Schiff base form of PLP-L-serine (PLS) bound enzyme were carried out to investigate the

structural dynamics and mode of actions of both inhibitors in the forward reaction. The atomistic details of *Plasmodium* SHMT inhibition could shed light on a future rational design of novel antimalarial drugs.

2. Materials and methods

2.1. Preparation of *Plasmodium* SHMT structures

The superimposed structures of SHMTs from *Pv*SHMT/D-serine/folinic acid (PDB entry 4OYT [42]) and *Pf*SHMT/PLP (PDB entry 4O6Z [55]) in **Fig. 2 .2A** showed high structural similarity on protein folding with the root-mean-square deviation (RMSD) value of 0.48 Å, and they shared 97% amino acid identity in the binding pocket (**Fig. 2.2C**). Thus, in the present study, the complexes of *Plasmodium* SHMT/PLS/inhibitors were prepared according to *Pv*SHMT structure. To obtain the *Pv*SHMT/PLS/inhibitor complexes of (+)-85 and (+)-86 **(Fig. 2 .2B)**, *Pv*SHMT/Gly/pyrazolopyran(+)-85 and (+)-86 cocrystal structures (PDB entries 5GVN and 5YFZ, respectively [20, 59]) were superimposed with *Pv*SHMT/PLS binary complex (PDB entry 4PFN [42]). For the *Pf*SHMT systems, *Pf*SHMT/PLP binary complex (PDB entry 4O6Z [55]) was superimposed with each prepared *Pv*SHMT/PLS/inhibitor complex of (+)-85 and (+)-86 to get *Pf*SHMT/PLS/inhibitor complexes of (+)-85 and (+)-86 structure coordinates. The binding pocket of pyrazolopyrans and PLS cofactor is located in the space surrounded by the five loops [42, 55], where the inhibitors are competitive toward the THF substrate to bind the folate-binding space (**Fig. 2 .2, A and B**). Note that only two subunit chains (*i.e.* chains A and B for *Pv*SHMT and chains C and D for *Pf*SHMT), which represent a native homodimer of *Plasmodium* SHMT [20, 42, 55], were selected for further investigation.

The partial atomic charges of the three ligands—PLS in the protonated ketoenamine form [40], pyrazolopyran(+)-85 and (+)-86—were calculated with HF/6-31G(d) level of theory using Gaussian09 program [60], as standard procedure [43, 44]. To assign bonded and non-bonded parameters, the AMBER ff14SB force field [61] was applied for the protein, and ligands were treated with a generalized AMBER force field version 2 (GAFF2) [62] using the Antechamber module of AMBER16 [46]. The protonation states of all ionizable residues were assigned at pH 7.0 using the PROPKA 3.1 program in PDB2PQR server [63]. Then, the prepared structures were

energy-minimized using 2,500 steps of steepest descents (SD) followed by 2,500 steps of the conjugate gradient (CG) method. The minimized structures were solvated by ~23,000 TIP3P water molecules in a truncated octahedral box with 10 Å space cutoff and neutralized by the addition of Na^+ ions. Note that the water molecules from the crystal structure were retained. Next, the solvated models were energy-minimized with a force constant of 50.0 kcal/$\cdot$mol$^{-1}\cdot$Å^2 to restrain the protein-heavy atoms using the same iterations of SD and CG methods described above before the whole protein-ligand system minimization.
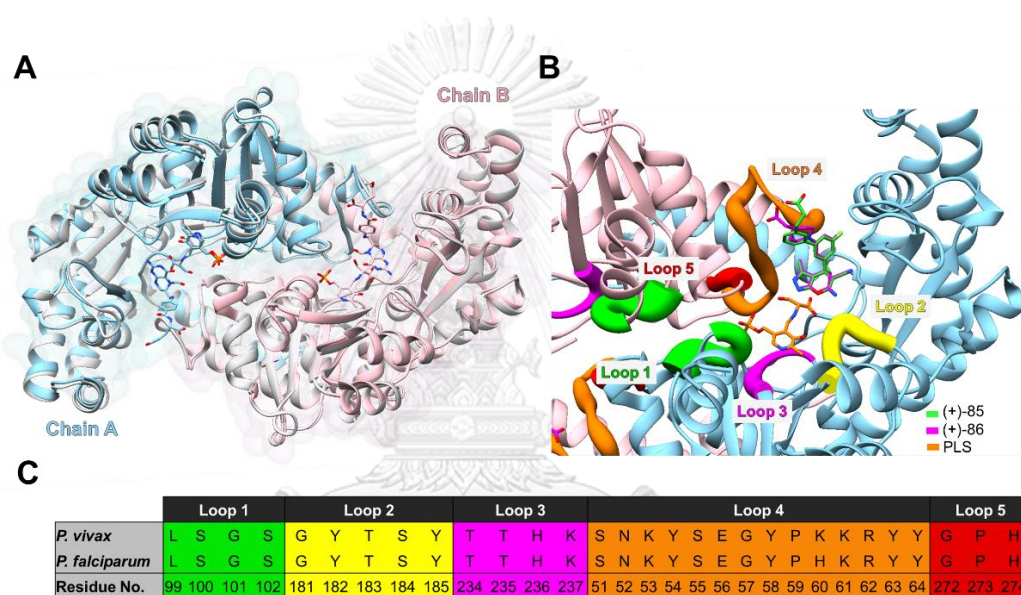

	Loop 1				Loop 2					Loop 3				Loop 4														Loop 5		
P. vivax	L	S	G	S	G	Y	T	S	Y	T	T	H	K	S	N	K	Y	S	E	G	Y	P	K	K	R	Y	Y	G	P	H
P. falciparum	L	S	G	S	G	Y	T	S	Y	T	T	H	K	S	N	K	Y	S	E	G	Y	P	H	K	R	Y	Y	G	P	H
Residue No.	99	100	101	102	181	182	183	184	185	234	235	236	237	51	52	53	54	55	56	57	58	59	60	61	62	63	64	272	273	274

Fig. 2.2 (**A**) The overlaid structures of *Pv*SHMT/D-serine/folinic acid and *Pf*SHMT/PLP complexes (PDB entries 4OYT and 4O6Z, respectively [42, 55]), where chains A and B of *Pv*SHMT are shown in light blue and pink, while chains C and D of *Pf*SHMT are shaded in grey. (**B**) The modeled structures of *Pv*SHMT/PLS/pyrazolopyrans in which the two competitive inhibitors pyrazolopyran(+)-85 and (+)-86 accommodate in the binding pocket containing the five loops: Loop 1 (green), Loop 2 (yellow), Loop 3 (magenta), Loop 4 (orange) and Loop 5 (red). (**C**) The amino acid sequence alignment of *Pv*SHMT and *Pf*SHMT binding pockets.

2.2. Molecular dynamics simulations and analysis

MD simulations of all four *Plasmodium* SHMT/PLS/pyrazolopyrans complexes were performed under the periodic boundary condition using the PMEMD.cuda module implemented in AMBER16 [46] for 500 ns with a 12 Å distance cutoff for non-bonded interactions. The particle mesh Ewald (PME) method [64, 65] was employed for long-range electrostatic interactions. All covalent bonds containing hydrogen atoms were constrained using the SHAKE algorithm [66, 67]. The systems were heated up from 10.0 to 298.15 K in 100 ps, and further equilibrated at 298.15 K for 100 ps. Subsequently, the simulations were carried out using *NPT* ensemble with 1 atm pressure at 298.15 K for 500 ps. Afterward, the systems with full MD simulations were conducted for 500 ns, using integration time step of 2 fs. A total of 50,000 MD snapshots with an equal time spacing throughout the MD simulations were collected. The MD trajectories from the last 100 ns of the simulated systems were extracted for further structural analyses using the CPPTRAJ module [68] of AMBER16 [46]. In addition, the per-residue decomposition free energy ($\Delta G_{\text{bind}}^{\text{residue}}$) relied on the MM/GBSA method [69, 70] and the solvated interaction energies (SIE)-based binding free energy (ΔG_{SIE}) [71, 72] of the complexes were calculated using the MMPBSA.py module [73] of AMBER16 [46] and the sietraj software [71, 72], respectively.

2.3. Molecular docking

Based on the rational drug design approach, using the *Pv*SHMT/PLS/(+)-86 template, eighty-nine analogs of pyrazolopyran(+)-86 were designed and evaluated by $\Delta G_{\text{bind}}^{\text{residue}}$ analysis and ligand-protein hydrogen bonding of MD simulations (further discussion in **Results** section 3 and 4). Charged and bulky heterocyclic groups were introduced to pyrazolopyran(+)-86 template to improve protein-ligand interactions. The binding affinity toward *Pv*SHMT/PLS was assessed by molecular docking of the designed analogs to the 50 MD snapshots of the *Pv*SHMT/PLS/(+)-86 system in the absence of (+)-86. First, each analog with 20 different poses was docked into the binding pocket for pyrazolopyran(+)-86 of each *Pv*SHMT/PLS MD snapshot using the AutoDock VinaXB software [74] with a cubical grid box of 20 × 20 × 20 Å. The pose which had the lowest docking score (ΔG_{vinaXB}) with a similar orientation to the core structure of pyrazolopyran(+)-86

was chosen for analysis. The average ΔG_{vinaXB} of each ligand, as well as pyrazolopyran(+)-85 and (+)-86 was then calculated from the 50 docking scores (**Table A1**).

3. Results and Discussion

3.1. Simulated *Plasmodium* SHMTs with pyrazolopyran-based inhibitors

To determine the conformation stability of the four simulated SHMTs of *Pv*SHMT and *Pf*SHMT bound with PLS and two pyrazolopyran-based derivatives (+)-85 (a terminal aromatic ring) and (+)-86 (an N-linked piperidine) in aqueous solution, the RMSD for protein backbone atoms of *Plasmodium* SHMTs relative to those of initial structures were calculated and plotted *versus* simulation time in **Fig. 2 .3, A** and **B**. The RMSD values of *Pv*SHMT and *Pf*SHMT complexes gradually increased at the first ~150 ns and then slightly fluctuated by ~1.7 to 2.2 Å for *Pv*SHMT systems and ~1.5 to 1.9 Å for *Pf*SHMT systems until reaching 500 ns. The results indicated that all the complexes tended to reach equilibrium after ~200 ns. Likewise, the total number of intermolecular H-bonds between the two ligands (PLS and pyrazolopyran inhibitor) and SHMT residues for all of the systems was relatively constant during 200-500 ns, supporting the equilibrium convergence (**Fig. 2.3, C** and **D**). It was noted that the *Pf*SHMT complexes had a slightly higher number of H-bonds (~25 ± 2) than *Pv*SHMT complexes (~22 ± 3) during the 500-ns simulation time. This implied despite the high sequence identity of the binding pocket (~97%) between the two *Plasmodium* species, the pocket space is somewhat different. These may be resulted from their oligomeric homodimer (further discussion in **the Inhibitory efficiency section**). Since the equilibrium was reached after 200 ns, the MD trajectories from the last 100 ns of each system were extracted and analyzed to comprehend the structural dynamics and binding affinity of pyrazolopyran-based inhibitors toward *Plasmodium* SHMTs using dynamic cross-correlation map (DCCM), the ΔG_{SIE}, the $\Delta G_{\text{bind}}^{\text{residue}}$, the percentage of H-bond occupancy and the solvent-accessible surface area (SASA), as discussed in the following sections.
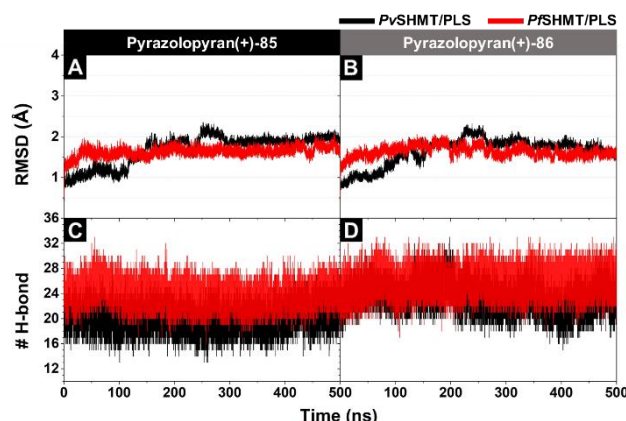
Fig. 2.3 Backbone RMSD and the number of intermolecular hydrogen bonds (#H-bond) of *Plasmodium* SHMTs bound with PLS and pyrazolopyran-based inhibitors, (**A and C**) pyrazolo-pyran(+)-85 and (**B and D**) pyrazolopyran (+)-86, along 500-ns MD simulations.

3.2. Protein motion associated with ligand binding

To assess the binding affinity of pocket residues toward the ligand, a DCCM was employed to create a two-dimensional matrix representation of time-correlated information among the protein residues from MD simulations [75]. Typically, the DCCM analysis gives the level of correlation between alpha-carbon (C_α) atoms that could reflect an influence of each residue imposed on the ligand [76-78]. The correlation in the DCCM plot is designated between +1 to −1 in which a positive correlation is for a residue motion moving along the direction of binding motion, whereas a negative correlation or anti-correlation motion is for an opposite movement, labeled as a red and blue patch, respectively, in **Fig. 2.4**. Red diagonal line in the DCCM plot represents a perfect positive correlation of each residue itself. Analysis of the DCCM plots for pyrazolopyran(+)-85 and (+)-86 binding to *Plasmodium* SHMT/PLS complexes showed a high-density pattern of residue motions in a positive correlation (red color) centered along the diagonal line. However, a significant increase of anti-correlated movements (a dense blue patch) was observed for residues located in Loop 2 (residues 181 to 185) and Loop 4 (residues 51 to 64) of *Pv*SHMT/PLS/pyrazolopyran(+)-85 complex, as shown in red and blue empty boxes, respectively, in **Fig. 2.4A**. The anti-correlated movement of these residues could definitely affect the binding affinity of pyrazolopyran(+)-85 to *Pv*SHMT/PLS (discussed later). The finding that the binding of pyrazolopyran(+)-85 and (+)-86 could induce similar positive correlated movement

of residues in most regions of the binding pocket demonstrates a favorable environment of *Pv*SHMT and *Pf*SHMT for these inhibitors.
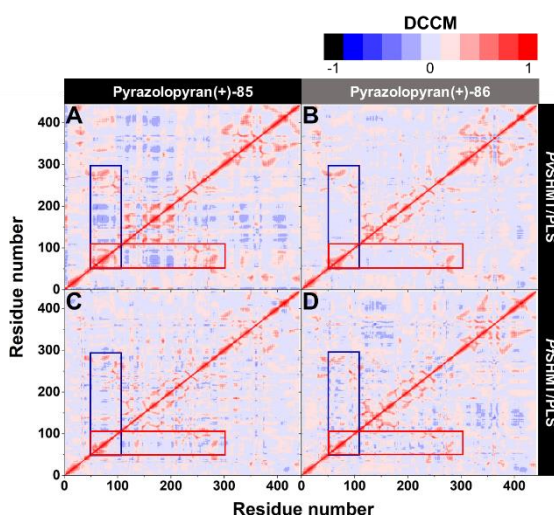

Fig. 2 . 4 DCCM plots of the complexes of (**A**) *Pv*SHMT/PLS/(+)85, (**B**) *Pv*SHMT/PLS/(+)86, (**C**) *Pf*SHMT/PLS/(+)85, and (**D**) *Pf*SHMT/PLS/(+)86, where the areas of the correlated and anti-correlated motions are shaded in red and blue colors, respectively. Note that the regions of red and blue rectangles involve the residues within the enzyme binding pocket (Loop 1 to Loop 5, defined in **Fig. 2.2B**).

3.3. Inhibitory efficiency of pyrazolopyrans

To analyze the binding affinity of protein–ligand complex, the ΔG_{SIE} [71, 72] of the two pyrazolopyran inhibitors with *Pv*SHMT/PLS and *Pf*SHMT/PLS complexes were calculated from 1,000 snapshots extracted from the last 100-ns simulation shown in **Fig. 2.3**. The ΔG_{SIE} function along with their molecular mechanics energy (ΔE_{MM}) and constants was described by **Equation 2.1** [72], where ΔE_{vdW} and ΔE_{ele} are the van der Waals interaction and electrostatic energies in the bound state, respectively, ΔG_{bind}^{R} is the change in the reaction field energy between the free and bound states, calculated by solving the Poisson equation [79, 80], ΔMSA is the change in molecular surface area upon binding, α represents the global proportionality coefficient relating to the loss of configurational entropy, γ represents the molecular area coefficient, and C represents a constant value.

$$\Delta G_{\text{SIE}} \;=\; \alpha \cdot [\Delta E_{\text{vdW}} + \Delta G_{\text{bind}}^{\text{R}} + \Delta E_{\text{ele}} + \gamma \cdot \Delta\text{MSA}] + \text{C} \qquad \textbf{Equation 2.1}$$

From the result in **Table 2.1**, ΔE_{vdW} was the primary stabilizing force in the complex formation for all of the systems (ΔE_{vdW} of $\sim$ –52 to –57 kcal·mol^{-1}) rather than the electrostatic interactions (ΔE_{ele} of $\sim$ –19 to –45 kcal·mol^{-1}). The relative lower ΔG_{SIE} values in the *Pv*SHMT complexes indicated the more favorable binding affinity of both inhibitors to *Pv*SHMT. In addition, pyrazolopyran(+)-86 exhibited a stronger binding affinity against both *Plasmodium* SHMTs (–12.22 kcal·mol^{-1} for *Pv*SHMT and –11.05 kcal·mol^{-1} for *Pf*SHMT) than (+)-85 (–10.57 and –9.72 kcal·mol^{-1}). These predicted binding free energies were in a similar range to the experimental binding free energy (ΔG_{exp}) of both inhibitors toward *Pf*SHMT ($\sim$ –10 kcal·mol^{-1}) [20]. In summary, the two inhibitors bind well within the ligand-binding pocket of *Pv*SHMT and *Pf*SHMT, with a slight preference for pyrazolopyran(+)-86 over (+)-85.

Table 2.1

The ΔG_{SIE} and its energy components for *Pv*SHMT and *Pf*SHMT in complex with pyrazolopyran(+)-85 and (+)-86. The ΔG_{exp} of *Pf*SHMT complexes is estimated from the reported IC_{50} [20] using the equation $\Delta G_{exp} \approx -RT\ln(IC_{50})$, where R is the gas constant (1.987×10^{-3} kcal·K^{-1}·mol^{-1}), and T is the temperature in Kelvin.

Energy components (kcal·mol^{-1})	*Pv*SHMT/PLS		*Pf*SHMT/PLS	
	(+)-85	(+)-86	(+)-85	(+)-86
ΔE_{vdW}	-56.49 ± 0.34	-57.28 ± 0.32	-57.23 ± 0.29	-52.22 ± 0.34
ΔE_{ele}	-19.43 ± 1.22	-23.33 ± 1	-40.65 ± 0.9	-45.05 ± 1.01
$\gamma \cdot \Delta MSA$	-13.75 ± 0.06	-13.38 ± 0.04	-14.04 ± 0.07	-13.24 ± 0.04
$\Delta G_{bind}^{residue}$	16.36 ± 1.16	4.96 ± 1.60	46.72 ± 1.28	32.60 ± 0.92
C		-2.89		
α		0.10		
ΔG_{SIE}	-10.57 ± 0.1	-12.22 ± 0.12	-9.72 ± 0.11	-11.05 ± 0.09
ΔG_{exp} [20]	-	-	-9.99	-9.95

3.4. Key residues upon inhibitors binding

To identify and evaluate the key residues critical for binding affinity of pyrazolopyran analogs (+)-85 and (+)-86, a $\Delta G_{bind}^{residue}$ based on the MM/GBSA method was calculated for each residue in the binding pocket of *Plasmodium* SHMT. In our case shown in **Fig. 2.5, A-H**, the residues with $\Delta G_{bind}^{residue}$ less than −1.0 kcal·mol^{-1} were defined as stabilizing residues, while those with $\Delta G_{bind}^{residue}$ higher than 1.0 kcal·mol^{-1} as destabilizing residues. The thirteen residues at the ligand- binding pocket of *Pf*SHMT and *Pv*SHMT were identified for their contributions in

pyrazolopyran binding including Y63, L124, G128, H129, L130, K139, T183, S184, F266, N356, T357, V365 and R371. The residues Y63 and F266 were previously reported to play a crucial role in ligand binding by providing hydrophobic interaction to pyrazolopyran(+)-85 and (+)-86 [20, 42, 55]. Our results here also showed that these residues Y63 and F266 have a favorable contribution to the binding of pyrazolopyran(+)-85 in *Pf*SHMT/PLS/(+)-85 complex with the $\Delta G_{\text{bind}}^{\text{residue}}$ of –4.11 and –1.14 kcal·mol^{-1}, respectively. Whereas the weaker contributions of Y63 and F266 to pyrazolopyran(+)-86 were detected in *Pv*SHMT/PLS/(+)-86 with the $\Delta G_{\text{bind}}^{\text{residue}}$ of –0.79 and –0.31 kcal·mol^{-1}, respectively. However, the apparent energy contributions from both residues were not observed in *Pf*SHMT/PLS/(+)-86 and *Pv*SHMT/PLS/(+)-85. This is based on the fact that the residues Y63 and F266 were able to freely move in or out from the inhibitor during MD simulation, resulting in the loss of the interactions as previously found in the X-ray structure. Hence, the results suggest that Y63 and F266 can adopt different conformations within the pocket space upon ligand binding. Other key residues T183 and S184, which were previously described to play an important role in PLS and THF binding [42, 55], exhibited a favorable contribution to pyrazolopyran(+)-85 at core structure (**Fig. 2.5, E and G**) with the $\Delta G_{\text{bind}}^{\text{residue}}$ of –1.01 and –0.53 kcal·mol^{-1} in *Pv*SHMT/PLS, and –1.15 and –1.01 kcal·mol^{-1} in *Pf*SHMT/PLS systems. However, a less contribution of T183 and S184 to pyrazolopyran(+)-86 was observed in *Pv*SHMT and *Pf*SHMT complexes with the $\Delta G_{\text{bind}}^{\text{residue}}$ of –0.17 and –0.05 kcal·mol^{-1}, and –0.69 and –0.68 kcal·mol^{-1}, respectively. The results revealed that the different part of pyrazolopyran(+)-85 and (+)-86 (heterocyclic and carboxylate groups) can affect the interaction at ligand core structure to the residues of *Plasmodium* SHMTs. Among other key binding residues, V365 provides a favorable interaction for the pyrazolopyran analogs in the *Pv*SHMT complex systems with the $\Delta G_{\text{bind}}^{\text{residue}}$ of –0.36 and –1.08 kcal·mol^{-1} for pyrazolopyran(+)-85 and (+)-86), respectively. As V365 is located on the surface loop close to a folate glutamate moiety in *Pv*SHMT/PLP-D-Ser/folinic acid (PDB entry 4OYT [42]), the position of V365 is somewhat close to a carboxyl substituent of the pyrazolopyran analogs in *Pv*SHMT indicating that this substituent could be modified for enhanced binding affinity of the pyrazolopyran analogs in *Plasmodium* SHMT.

Opposite to others pocket residues, our result showed that R371 provides unfavorable interactions to pyrazolopyran(+)-85 with $\Delta G_{\text{bind}}^{\text{residue}}$ value of 1.59 and 1.64 kcal·mol^{-1} for

*Pv*SHMT/PLS and *Pf*SHMT/PLS systems, respectively (**Fig. 2.5, A** and **C**). This could be due to the presence of β-hydroxymethyl group of PLS that may induce steric hindrance to the isopropyl group of (+)-85 thus pushing it toward the positively charged guanidinium side-chain of R371 [81]. This repulsive force of R371 was not observed in the binding of (+)-86 with an N-linked piperidine derivative which is more flexible than (+)-85 with a terminal aromatic ring. Apart from the residues mentioned above, a number of residues favorably contributed in all four *Plasmodium* complex systems include L124, G128, H129, L130, K139, N356, and T357. It was worth to mention that the conserved residue L124 [42, 55, 59] showed the lowest $\Delta G_{\text{bind}}^{\text{residue}}$ value of –3.97, –2.77, –2.70 and –3.22 kcal·mol^{-1} for *Pv*SHMT/PLS/(+)-85, *Pv*SHMT/PLS/(+)-86, *Pf*SHMT/PLS/(+)-85 and *Pf*SHMT/PLS/(+)-86, respectively. Consistent to the structures of *Pv*SHMT/pyrazolopyran complexes [20, 42], L124 provides van der Waals interactions to the *meta*-fluoro-substituted phenyl ring. In addition to L124, the residues G128 and T357 are favorably associated in binding of pyrazolopyran(+)-85 and (+)-86 and several inhibitors [19, 20]. These three residues also displayed a very high percentage of H-bond occupancy (~83 to 100%) as shown in **Fig. 2.5, I-L**. Taken together, the critical pocket residues of *Pv*SHMT and *Pf*SHMT for both stable and unfavorable binding of pyrazolopyran(+)-85 and (+)-86 were here evaluated and identified based on the $\Delta G_{\text{bind}}^{\text{residue}}$.
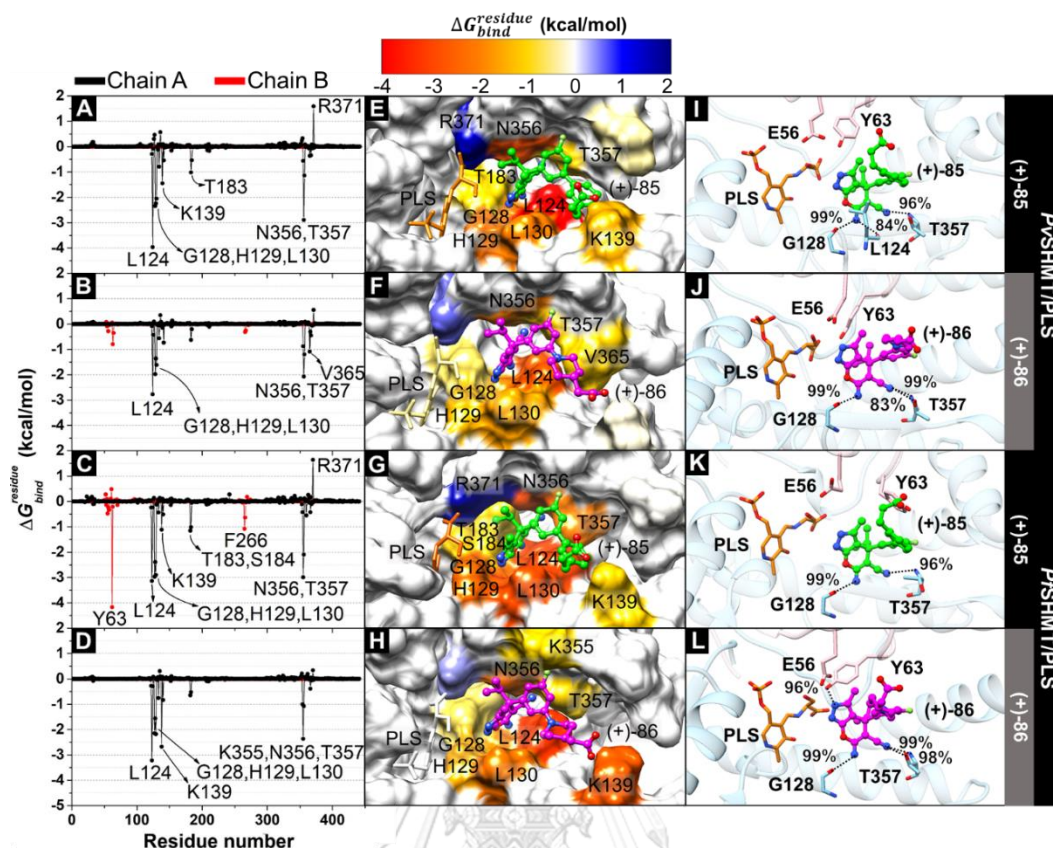
Fig. 2.5 (**A-D**) $\Delta G_{\text{bind}}^{\text{residue}}$ for *Pv*SHMT/PLS and *Pf*SHMT/PLS bound with pyrazolopyran(+)-85 and (+)-86. (**E-H**) The important amino acids and PLS involved in ligand binding, which were colored according to their $\Delta G_{\text{bind}}^{\text{residue}}$ values. (**I-L**) Binding patterns of pyrazolopyran(+)-85 and (+)-86 complexes are drawn from the last MD snapshot, where black dashed lines represent H-bonds along with their percentage of H-bond occupancy for the key binding residues.

3.5. Protein-inhibitor hydrogen bonding

H-bond interaction has been known as an essential factor beneficial for ligand binding affinity to a protein target [42, 55, 82, 83]. H-bonding can be drawn from crystal structures based on H-donor and acceptor distance; however, it cannot be distinguished among other binding interactions namely van der Waals, salt bridge and so on, from the protein solution. Here, H-bond analysis with the CPPTRAJ module [68] of the AMBER16 program [46] was employed to calculate a number and percentage of H-bond occupancy for the binding of pyrazolopyran(+)-85 and (+)-86 to *Pv*SHMT/PLS and *Pf*SHMT/PLS complexes from the last 100 ns of the MD

simulations (**Fig. 2.6**). Pyrazolopyran(+)-86 binds to both *Pv*SHMT and *Pf*SHMT with ~23 and ~26 H-bonds compared to (+)-85 having ~21 and ~24 H-bonds, as shown in **Fig. 2.3, C and D**. This result also suggested that pyrazolopyran(+)-86 has more favorable binding to *Plasmodium* SHMTs over (+)-85 thus in part explaining a longer half life of (+)-86 [20]. We also observed that most of the high percentage of H-bond occupancy ($\geq$80%) (**Figs. 2.5, I-L and 2.6**) were derived from the interactions at the pyrazolopyran-core structure with E56, L124, G128 and T357, *i.e.*, OE2(E56)···H-N^3, O(L124)···H-N^2, O(G128)···H-N^2, N^1···H-N(T357) and N^1···H-OG1(T357). These four residues play a vital role in the pyrazolopyran binding consistent with the results from $\Delta G_{\text{bind}}^{\text{residue}}$ and the X-ray structures of *Pv*SHMT [20-21]. Particularly, L124 and G128 formed a strong H-bond interaction to the pterin moiety of pyrazolopyran(+)-85 and (+)-86 in *Pv* and *Pf*SHMT complexes with >45% and >99% occupancies, respectively. Moreover, T357, the key residue which formed H-bonds with N^1 and N^2 of the pyrazolopyran-core structure, showed various percentages of H-bond occupancies (from 0 to 100% in **Fig. 2.6**) in different complexes. Interestingly, the percentages of H-bond occupancies of N^1···H-OG1(T357) and N^2···H-OG1(T357) were increased when the percentage of H-bond occupancy of a nearby residue, O(L124)···H-N^2 was over 50% and 80%, respectively. This observation indicated that L124 and T357 stabilized the pyrazolopyran-core at N^1 and N^2 positions. Additionally, E56, known to play a function in the SHMT catalytic mechanism (equivalent to E75 in rabbit and human cytosolic SHMT and E74 in sheep cytosolic SHMT) [33, 34], exhibited the moderate percentage of H-bond occupancy (~62%) in *Plasmodium* SHMT complexed with pyrazolopyran(+)-86. At the same time, Y63 stabilized pyrazolopyran(+)-85 binding at O^2 and O^3 of the carboxylate side chain with the percentage of H-bond occupancies of ~11% and ~15% for *Pv*SHMT/PLS and ~45% and ~49% for *Pf*SHMT/PLS, respectively. The H-bond preference of Y63 to pyrazolopyran(+)-85 over (+)-86 is likely due to a π-π interaction between a terminal aromatic ring of (+)-85 and Y63 arranging the carboxyl moiety to interact with the hydroxyl side chain of Y63 (see **Fig. 2.1A**). For the H-bond interaction between *Plasmodium* SHMTs and PLS molecule (**Fig. A1**), D208, H129 and R371 made a strong H-bonding with ~85%, ~96% and ~84% occupancies to the pyridyl nitrogen, hydroxyl and carboxyl functional groups of PLS, respectively. Thus, these three residues were crucial for PLS stabilization supported by the crystal structure of *Plasmodium* SHMTs [42, 55].
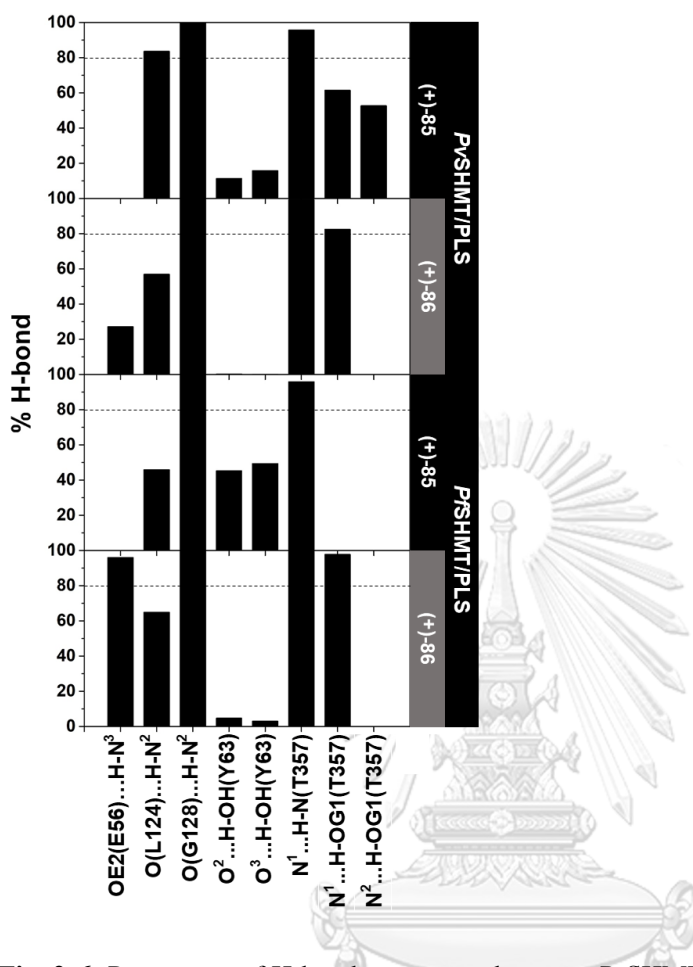
Fig. 2.6 Percentage of H-bond occupancy between *Pv*SHMT/PLS and *Pf*SHMT/PLS complexes with pyrazolopyran(+)-85 and (+)-86 bound over the last 100 ns with ≥ 40% cut-off. The standard geometric criteria of H-bonding are: (*i*) the distance between the donor and acceptor atoms is below 3.5 Å; and (*ii*) the angle between the donor, hydrogen and the acceptor atoms is over 120° [83].

3.6. Solvent accessibility of binding pocket

To determine the water accessibility of the binding pocket of *Plasmodium* SHMTs after complex formation with pyrazolopyran(+)-85 and (+)-86 inhibitors, we calculated the SASA value of the surrounding residues located within 5 Å sphere of the inhibitor in the complex based on an assumption that the lower SASA values refer to the higher the binding affinity of inhibitors toward protein. **Fig. 2.7** highlighted that the SASAs values at the ligand-binding pocket of

pyrazolopyran(+)-85 and (+)-86 in both *Plasmodium* SHMTs were found in the range of ~390 to 570 Å^2. However, pyrazolopyran(+)-86 bound to the *Pv*SHMT and *Pf*SHMT with the lower SASA values of 442 ± 80 and 393 ± 57 Å^2, respectively, suggesting that (+)-86 was well packed in the binding pockets, compared to (+)-85 (572 ± 85 and 547 ± 68 Å^2). Again, this result supported the higher binding affinity of pyrazolopyran(+)-86 toward *Plasmodium* SHMTs (see also **Inhibitory efficiency** section above).
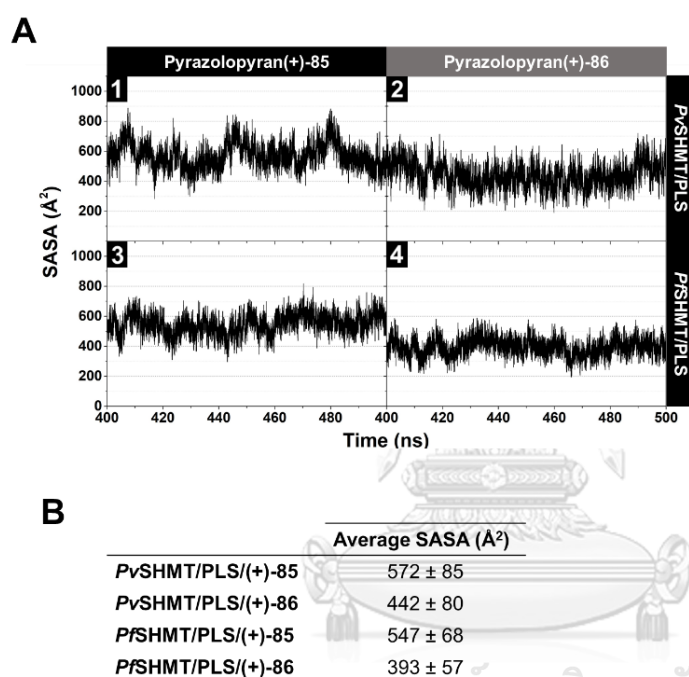
Fig. 2.7 (**A**) SASA along the last 100 ns of (**A1**) *Pv*SHMT/PLS/(+)-85, (A2) *Pv*SHMT/PLS/(+)-86, (**A3**) *Pf*SHMT/PLS/(+)-85, (A4) *Pf*SHMT/PLS/(+)-86. (**B**) Average SASA (the data are shown as mean ± standard deviation) within 5-Å sphere of pyrazolopyran(+)-85 and (+)-86 for *Pv*SHMT/PLS and *Pf*SHMT/PLS.

3.7. Rational inhibitor design

Our *in silico* investigation of pyrazolopyran(+)-based ligand binding in *Pv*SHMT and *Pf*SHMT rendered many vital factors for the mode of inhibition, which is challenging for rational design approaches in the development of more effective inhibitors. First, changing the methyl group at pyrazolopyran core structure (**Fig. 2.8A, red**) to the polar moiety (*e.g.*, aldehyde,

hydroxyl, or amide group) could promote H-bonding with the surrounding residues Y63 and Y64. Second, an introduction of the negatively charged group (*e.g.*, carboxylate group) to substitute an isopropyl moiety of pyrazolopyran core (**Fig. 2 . 8A, blue**) might enhance the electrostatic interaction with R371, and consequently decrease the unfavorable $\Delta G_{bind}^{residue}$ of this residue, as shown in **Fig. 2.5**. Third, a substitution of a phenyl group of pyrazolopyran(+)-85 or a piperidine ring of (+)-86 by other heterocyclic groups (*e.g.*, (1) pyridine, (2) pyrimidine, (3) pyran, (4) morpholine or (5) others as shown in **Fig. 2 .8A, magenta**) mostly tended to interact with the surrounding residues (L124, F134, C364, and V365). The backbone –NH of these nearby residues might form H-bonding networks with the pyridine and pyrimidine nitrogen, or the pyran and morpholine oxygen. Nonetheless, *meta*-fluoro moiety (**Fig. 2.8A, green**) should be retained as it exhibited favorable interactions with the surrounding residues K355, N356 and T357 (**Fig. 2.5E-H**). The H-bond analysis and $\Delta G_{bind}^{residue}$ calculation (**Fig. 2 .5** and **2 .6**) also suggested that the carboxyl group at the terminal end of pyrazolopyran(+)-85 (**Fig. 2 .8A, light blue**) could be an important moiety to interact with Y63 and K139 [20].

Based on the rational idea mentioned above, the newly designed eighty-nine pyrazolopyran(+)-86 derivatives were further investigated by molecular docking to the 50 snapshots of *Pv*SHMT/PLS/(+)-86 complex, the highest binding affinity system. The docking results were summarized in **Table A1**, and the analogs with an average docking energy of < -12.5 kcal·mol^{-1} were selected for analysis (**Fig. 2 .8B**). The newly eighty-nine designed compounds were named by the position of the four modified parts (R1 to R4). The original pyrazolopyran(+)-86 template was named "1111". Then, the first, second, and so on of R1 modification was named "2111", "3111", ... as shown in **Table A1**. The result on **Table A1** showed that at least one position modification on pyrazolopyran core with small groups slightly affected their binding affinity compared to (+)-85 and (+)-86. However, the substitution of the piperidine ring with some negatively bulky groups (*e.g.*, compounds 11137 and 11139) showed an enhanced binding affinity over pyrazolopyran(+)85 and (+)-86 by approximately 2 kcal·mol^{-1}. Likewise, a substitution of isopropyl moiety by a carboxyl group in combination with a bulky substitution on the piperidine ring as shown in compounds 12135, 12137, 12138, 12139, and 12140 (**Table A1**) could enhance the interactions of such analogs toward *Pv*SHMT (a docking energy of ~ -13 kcal·mol^{-1}). Although most modifications of the pyrazolopyran derivatives did not provide any

significant difference in the docking score, the compound 12235 with three substitutions exhibited the most preferable docking score of -13.47 ± 0.61 kcal·mol^{-1}. In addition to verifying the promising compounds to be used as the effective *Plasmodium* SHMT inhibitors, molecular docking study of the eight compounds was performed on human cytosolic and mitochondrial SHMT (hcSHMT [84] and hmSHMT [85], respectively). The results revealed that the eight newly designed compounds better interacted with *Plasmodium* SHMT than with human SHMT by ~2-folds (**Fig. A2**). These results suggested that the eight newly designed compounds 11137, 11139, 12135, 12137, 12138, 12139, 12140 and 12235 could be promising inhibitors against *Plasmodium* SHMTs and are worth for further investigation on enzyme inhibition efficacy. Moreover, *in vitro* and/or *in vivo* evaluation of the eight designed compounds on *Plasmodium* and human SHMTs should be further carried out to confirm the selectivity of ligands to a specific protein.
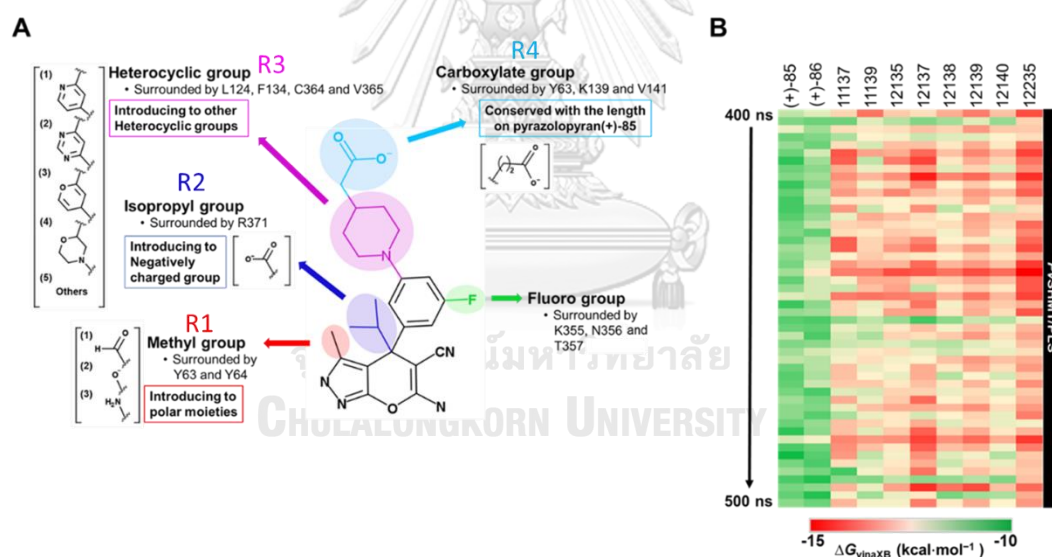
Fig. 2.8 (**A**) 2D illustration of protein-ligand interactions and the rational design of the possible modified fragments of the pyrazolopyran(+)-86. (**B**) The predicted binding affinity of newly designed pyrazolopyrans toward *Pv*SHMT/PLS with averaged docking energy ≤ -12.5 kcal·mol^{-1} from docking study on the 50 MD snapshots (chemical structures in **Table A1**). The red color showed better binding affinity of compounds, while the green color showed weak binding affinity of compounds.

4. Conclusions

In this study, all-atom MD simulations to explore the protein–ligand interactions and binding affinity of pyrazolopyran(+)-85 and (+)-86 toward *Pv*SHMT and *Pf*SHMT in the forward reaction in an aqueous solution were carried out. High conformation stability of all four complexes of *Plasmodium* SHMT/PLS and pyrazolopyran(+)-85 and (+)-86 was observed throughout MD simulations. The SIE-based binding free energy results revealed that van der Waals interaction was the primary driving force used for forming the complex between *Plasmodium* SHMTs and both pyrazolopyran inhibitors rather than electrostatic interaction. In addition, pyrazolopyran(+)-86 exhibited a higher binding efficiency for both *Plasmodium* SHMTs than (+)-85, as supported by the higher percentage of H-bond occupancy and the lower SASAs. The active site residues L124, G128, H129, L130, K139, N356, and T357 preferentially interacted with the two inhibitors. In particular, the residues L124, G128, and T357 provided prominent interactions with the pyrazolopyran inhibitors. Eventually, structure-based drug design suggested that the isopropyl moiety and the bulky heterocyclic fragments could be substituted with the negatively charged group (e.g., carboxylate), to fulfill interactions with the positively charged R371, and the piperidine ring, to enhance H-bonding with the surrounding residues, respectively. In summary, the computational information presented here can be helpful for the future design and development of antimalarial drugs targeting *Plasmodium* SHMTs.

Acknowledgments

CONCLUSIONS OF PROJECT II

1. The crystal structure of *Plasmodium vivax* SHMT (Sal-1) with pyrazolopyran(+)-85 and (+)-86 bound were retrieved from the PDB database (PDB entries 5GVN [20] and 5YFZ [59]). The *Plasmodium vivax* SHMT strain Sal-1 was reported as a wild-type strain [86]. The resolution of the crystal structures was in an acceptable range (2.30 Å for 5GVN and 2.16 Å for 5YFZ). The Ramachandran plot in UCSF Chimera 1.4 program [87] showed most residues of 5GVN and 5YFZ were in the allowed region (**Fig. S2.1, A and B**). For the crystal structure of *P. falciparum* SHMT, there was only one PDB file (4O6Z [55]) with PLP bound. The resolution was 2.98 Å, which was in an acceptable range. Moreover, the Ramachandran plot in **Fig. S2.1C** showed that most residues of the *Pf*SHMT structure were in the allowed region. These results indicated the acceptable conformations of crystal structures of *Pv*SHMT and *Pf*SHMT, which were used as studied complexes in this project.
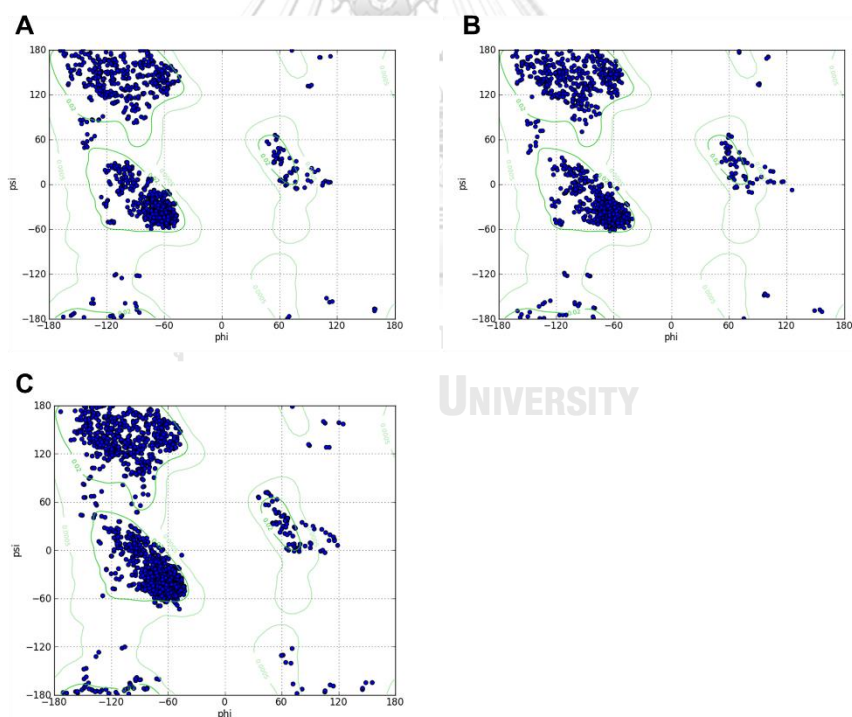
Fig. S2.1 The Ramachandran plot in the UCSF Chimera 1.4 program visualizer [87] of (**A**) *Pv*SHMT/Gly/pyrazolopyran(+)-85 (PDB entries 5GVN [20]), (**B**) *Pv*SHMT/Gly/(+)-86 (PDB entries 5YFZ [59]), and (**C**) *Pf*SHMT/PLP (PDB entries 4O6Z [55]).

2. The overlaid structures of *Plasmodium falciparum*, *P. vivax* and human cytosolic SHMT (hcSHMT) in **Fig. S2.2A** showed the similar conformation of these three SHMT structures with the RMSD of 0.705 Å (< 2 Å). However, main different part (flap motif) was observed on hcSHMT [57]. The pairwise alignment of the amino acid in the binding pocket showed 73.3% of sequence similarity between the *Plasmodium* SHMTs and hcSHMT (**Fig. S2.2B**). These results indicated the main difference, especially in the binding pocket between *Plasmodium* SHMT and hcSHMT, which could affect the specific inhibitor development for *Plasmodium* SHMTs.

	Loop 1				Loop 2					Loop 3				Loop 4														Loop 5		
P. vivax	L	S	G	S	G	Y	T	S	Y	T	T	H	K	S	N	K	Y	S	E	G	Y	P	K	K	R	Y	Y	G	P	H
P. falciparum	L	S	G	S	G	Y	T	S	Y	T	T	H	K	S	N	K	Y	S	E	G	Y	P	H	K	R	Y	Y	G	P	H
Residue No.	99	100	101	102	181	182	183	184	185	234	235	236	237	51	52	53	54	55	56	57	58	59	60	61	62	63	64	272	273	274
hcSHMT	Y	S	G	S	G	T	S	C	Y	T	T	H	K	N	N	K	T	S	E	G	Y	P	G	Q	R	Y	Y	G	P	H
Residue No.	118	119	120	121	201	202	203	204	205	254	255	256	257	70	71	72	73	74	75	76	77	78	79	80	81	82	83	303	304	305

Fig. S2.2 (A) The superimposition of crystal structures of *Plasmodium falciparum* (brown), *P. vivax* (blue), and human cytosolic (pink) SHMTs with the RMSD of 0.705 Å. (**B**) The amino acid sequence alignment of *Pv*SHMT and *Pf*SHMT and hcSHMT binding pockets. It should be noted that red color indicated the different amino acid between *Pf*SHMT and *Pv*SHMT, and blue color indicated the different amino acid between *Pf*SHMT, *Pv*SHMT and hcSHMT.

3. With the limitation of time and financial support, *in vitro* and/or *in vivo* studies cannot perform to test the eight newly designed compounds on *Pv*SHMTs and human SHMTs in this present study. Alternatively, *in silico* molecular docking was performed using the AutoDock VinaXB program. The molecular docking results showed that the eight designed compounds could bind

well within the active site of *Plasmodium* SHMT rather than that of human SHMTs, as shown in **Fig. A2** in **APPENDIX A** section. *Pv*SHMT/PLS/modified ligand complexes exhibited the lower binding free energy (ΔG_{vinaXB}) by approximately 4 kcal·mol^{-1} (~2-fold decrease) compared to human SHMTs. These findings suggested the high selectivity of eight newly modified compounds to *Plasmodium* SHMT.

4. The core structure of pyrazolopyran(+)-85 and (+)-86 in **Fig. S2.3** was the main part that exhibited the strong interaction to the residues in the binding pocket of *Plasmodium* SHMTs with the lower $\Delta G_{bind}^{residue}$ L124, G128, H129, L130, K139, N356, and T357 (**Fig. 2.5**) and of >80% of H-bond occupancies (**Fig. 2.6**). However, the modification some parts of the pyrazolopyran inhibitor could affect the binding affinity to *Plasmodium* SHMT. Changing the isopropyl group (R2) to carboxylate group together with the modification of the heterocyclic part (R4) (**Fig. 2.8A**) to the bigger bulky group could promote the strongest binding affinity of the new designed compounds to *Plasmodium* SHMT as showed in **Table S1** in **APPENDIX A** section. It should be noted that the evaluation of the newly designed compounds was investigated by the molecular docking method, which exhibited the ranking of binding energy of each molecule compared to pyrazolopyran(+)-86 reference ligand.
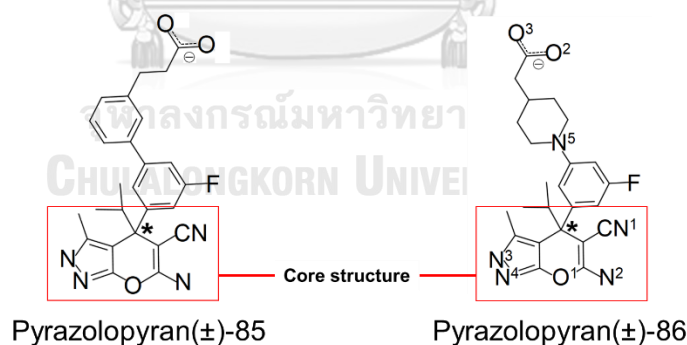
Fig. S2.3 The core structure of pyrazolopyran(+)-85 and (+)-86 which exhibited the strong interaction to the residues in the binding pocket of *Plasmodium* SHMTs.

CHAPTER III

PROJECT III: MANUSCRIPT II

in silico and in vitro potential of FDA-approved drugs for antimalarial drug discovery against Plasmodium serine hydroxymethyltransferases

Pitchayathida Mee-udorn[a], Kochakorn Phiwkaow[b], Ruchanok Tinikul[c], Kamonpan Sanachai[d], Somchart Maenpuen[b], and Thanyada Rungrotmongkol[a,e]*

[a]Program in Bioinformatics and Computational Biology, Graduate School, Chulalongkorn University, Bangkok 10330, Thailand

[b]Department of Biochemistry, Faculty of Science, Burapha University, Chonburi 20131, Thailand

[c]Department of Biochemistry and Center for Excellence in Protein and Enzyme Technology, Faculty of Science, Mahidol University, Bangkok 10400, Thailand

[d]Department of Biochemistry, Faculty of Science, Khon Kaen University, Khon Kaen 40002, Thailand

[e]Center of Excellence in Biocatalyst and Sustainable Biotechnology, Department of Biochemistry, Faculty of Science, Chulalongkorn University, Bangkok 10330, Thailand

E-mail address: t.rungrotmongkol@gmail.com, thanyada.r@chula.ac.th

Phone: +66-2218-5426. Fax: +66-2218-541

Prepared manuscript for submission to the journal "Journal of Biomolecular Structure and Dynamics"

in silico and *in vitro* **potential of FDA-approved drugs for antimalarial drug discovery against *Plasmodium* serine hydroxymethyltransferases**

Pitchayathida Mee-udorn[a], Kochakorn Phiwkaow[b], Ruchanok Tinikul[c], Kamonpan Sanachai[d], Somchart Maenpuen[b], and Thanyada Rungrotmongkol[a,e]*

[a]Program in Bioinformatics and Computational Biology, Graduate School, Chulalongkorn University, Bangkok 10330, Thailand

[b]Department of Biochemistry, Faculty of Science, Burapha University, Chonburi 20131, Thailand

[c]Department of Biochemistry and Center for Excellence in Protein and Enzyme Technology, Faculty of Science, Mahidol University, Bangkok 10400, Thailand

[d]Department of Biochemistry, Faculty of Science, Khon Kaen University, Khon Kaen 40002, Thailand

[e]Center of Excellence in Biocatalyst and Sustainable Biotechnology, Department of Biochemistry, Faculty of Science, Chulalongkorn University, Bangkok 10330, Thailand

E-mail address: t.rungrotmongkol@gmail.com, thanyada.r@chula.ac.th

Phone: +66-2218-5426. Fax: +66-2218-541

Graphical Abstract

Abstract

Malaria has spread in many countries with a 12% increase in death cases after the COVID-19 pandemic. Over the Greater Mekong subregion, malaria is one of the harass diseases with a highly drug-resistant rate. Serine hydroxymethyltransferase (SHMT), the key enzyme in the deoxythymidylate (dTMP) synthesis pathway, was reported as a promising antimalarial drug target because of its conserved binding pocket. In this study, 2,509 FDA-approved drugs were screened by the molecular docking approach using the seven structures of *Plasmodium* SHMTs. Eight compounds exhibited a significantly lower binding energy than the known SHMT inhibitor pyrazolopyran(+)-86, THF and antimalarial drugs ~ 4 to 10 kcal/mol. Then, the enzyme-based assay was performed to investigate the eight candidates. The result suggested that amphotericin B was the best competitive inhibitor for His_6-*Pf*SHMT with IC_{50} of 106 ± 1 μM. Therefore, the 500-ns MD simulation of *Pf*SHMT/PLS/amphotericin B was performed. The backbone RMSD of the protein-ligand complex indicated stability during the simulations, supported by the R_g, the H-bond interaction, and the number of atom contacts. The great binding affinity of amphotericin B was indicated by the solvated interaction energy (ΔG_{SIE}) calculation to *Pf*SHMT (~ −10.5 kcal/mol), supported by the strong ligand-protein interactions ($\geq$80% occurrences) within the enzyme active site (*i.e.*, Y63, L124, L130, F134, V141, K251, D258, S263, and V365) predicted by the pharmacophore modeling method. Therefore, our findings presented here identified the new *Plasmodium* SHMT inhibitor with known inhibitory activity and the experimental and computational information provided a core structure that differs from the previous SHMT inhibitors which could be a rational idea for novel antimalarial drug design.

Keywords: *Plasmodium* SHMT, Drug repurposing, Malaria, Molecular docking, Molecular Dynamics simulations, Enzyme-based assay

1. Introduction

Malaria is a mosquito-borne disease that commonly infects humans by five species of *Plasmodium*, *i.e.*, *P. falciparum*, *P. vivax, P. malariae*, *P. ovale*, and *P. knowlesi* [5-8]. Two of these species: *P. falciparum* and *P. vivax*, account for the severe form of malaria worldwide [9, 49]. In 2020, there were 241 million clinical malaria cases and 627,000 deaths estimated by WHO (a 12% increase from 2019 after the COVID-19 pandemic) [4]. The available treatments, particularly for *P. falciparum* and *P. vivax* malaria, are artemisinin-based combination therapy (ACT) and chloroquine [88, 89]. However, antimalarial drug resistance to the first-line treatment drugs and other antimalarial drugs currently used has been reported in many parts of the world, especially in the Greater Mekong subregion [6, 11, 12]. Therefore, the discovery of new drugs and new targets became considerable.

Serine hydroxymethyltransferase (SHMT) is the crucial enzyme in the deoxythymidylate (dTMP) synthesis pathway, which catalyzes the reversible conversion of L-serine and (6S)-tetrahydrofolate (THF) to glycine and 5,10-methylenetetrahydrofolate (CH_2-THF) [19, 20, 22]. SHMT was reported as the novel antimalarial drug target because of its conserved folate-binding pocket in five loops (**Fig. 3.1, A and B**) which is considered the target for novel inhibitors [42, 59, 90]. Hence, drug resistance caused by protein mutation should occur at a low rate on this enzyme. In addition, inhibition of SHMT expression or function could be lethal to the *Plasmodium* parasites [42]. In this respect, the discovery of *Plasmodium* SHMT inhibitors could provide ideas for novel antimalarial drug development.

The traditional drug development for the *Plasmodium* SHMT target might take many years and high costs to complete the process [29]; therefore, drug repurposing could be a suitable strategy to reduce time and investment in novel drug discovery [29, 30]. Drug repurposing or drug reprofiling is a rapid process to identify new uses for approved drugs (e.g., FDA-approved drugs) that are outside the scope of the original medical indication [91]. The risk of failure from the drug repurposing method is lower than the traditional process because the repurposed drug has already been found to be sufficiently safe in preclinical models and humans [92]. Drug repurposing could be performed by various methods, computational or experimental approaches. In the present study, the combination of structure-based computational and experimental processes is carried out to explore new antimalarial drugs from FDA-approved drugs targeting

Plasmodium SHMTs. The molecular docking method is used to screen new potent antimalarial drugs from the Drugbank database [93] against *P. vivax* SHMT (*Pv*SHMT) and *P. falciparum* SHMT (*Pf*SHMT). The hit compounds are then selected to investigate the inhibitory effect on *Pf*SHMT by enzyme-based assay. Finally, the structural dynamics and mode of action of the most potent compound are studied by all-atom molecular dynamics (MD) simulations for 500 ns. The experimental data and atomistic details of new potent *Plasmodium* SHMT inhibitors could be helpful for future drug discovery of a novel antimalarial treatment.

		Loop 1			Loop 2					Loop 3				Loop 4													Loop 5		
P. vivax	L	S	G	S	G	Y	T	S	Y	T	T	H	K	S	N	K	Y	S	E	G	Y	P	K	K	R	Y	Y	G	P	H
P. falciparum	L	S	G	S	G	Y	T	S	Y	T	T	H	K	S	N	K	Y	S	E	G	Y	P	H	K	R	Y	Y	G	P	H
Residue No.	99	100	101	102	181	182	183	184	185	234	235	236	237	51	52	53	54	55	56	57	58	59	60	61	62	63	64	272	273	274
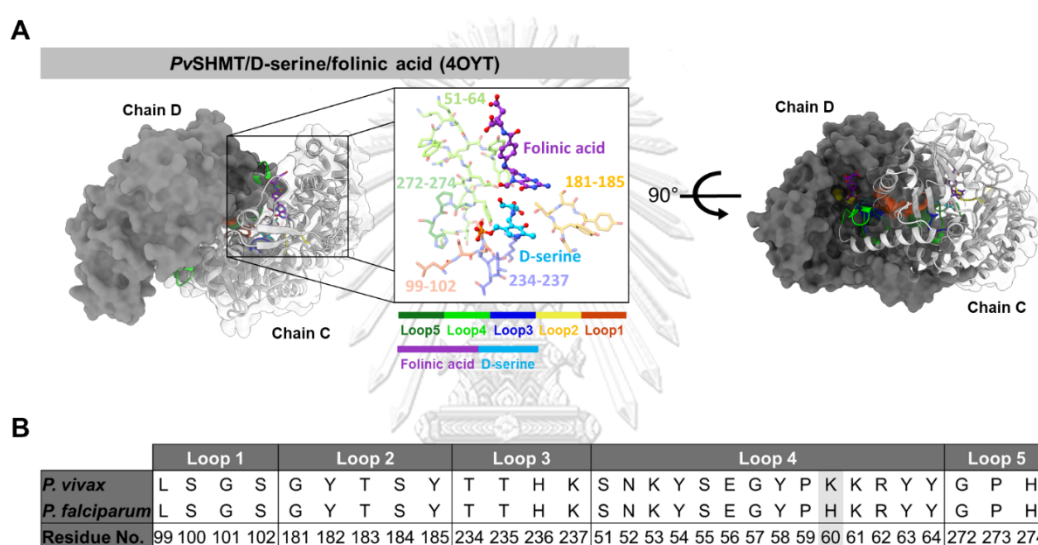
Fig. 3.1 *Plasmodium vivax* SHMT (*Pv*SHMT) structure with folinic acid and D-serine bound (PDB entry 4OYT [42]), where chains C and D are visualized as ribbons and surface diagram, respectively (**A**). The amino acid sequence alignment of *Pv*SHMT and *P. falciparum* SHMT (*Pf*SHMT) binding pockets with 97% amino acid identity [42, 55] (**B**). Note that the different amino acids are shaded in gray.

2. Materials and methods

2.1. *Plasmodium* SHMT structures

In this study, seven structures of *Plasmodium vivax* (*Pv*) and *P. falciparum* (*Pf*) SHMTs were investigated. Five crystal structures from seven complexes of *Pv*SHMT and *Pf*SHMT were retrieved from protein databank (PDB), *i.e.*, *Pf*SHMT/pyridoxal-5'-phosphate (PLP), *Pv*SHMT/L-

serine Schiff base (PLS), *Pv*SHMT/D-serine/folinic acid, *Pv*SHMT/Gly/pyrazolopyran(+)-85 and *Pv*SHMT/Gly/pyrazolopyran(+)-86 (PDB entry 4O6Z [55], 4PFN [42], 4OYT [42], 5GVN [20] and 5YFZ [59], respectively). Another two structures (5YFZ/PLS/pyrazolopyran(+)-86 and 4O6Z/PLS/pyrazolopyran(+)-86) were averaged from the last 100-ns MD simulations of our previous work [45]. For further study, only two subunit chains were selected, *i.e.*, chains C and D for *Pf*SHMT and chains A and B for *Pv*SHMT, which represent a native homodimer of *Plasmodium* SHMTs [20, 42, 55].

2.2. Structure-based virtual screening

Based on the virtual screening approach, the 2,509 FDA-approved drugs from the Drugbank database [93] were screened to find the drugs repurposed for antimalarial treatment by molecular docking method using the AutoDock VinaXB program [74]. The validation of the docking study was carried out by re-docking all ligands (folinic acid, pyrazolopyran(+)-85, and pyrazolopyran(+)-86) into the substrate-binding cleft (Loop 1 to Loop 5) of the five *Plasmodium* SHMT crystal structures retrieved from PDB and two structures from MD simulations. The cubical grid box of 30 × 30 × 30 Å was created to cover the representative chain (chain A for *Pv*SHMT and chain C for *Pf*SHMT). The molecular docking was performed with 20 docking poses for each compound. Then, the docking scores were ranked from the smallest to the largest. The pose which exhibited the lowest docking score in the seven complexes was selected for further analysis. Note that the results from the molecular docking method were visualized by the Discovery Studio Visualizer 2021 [47] and the UCSF Chimera version 1.16 [87].

2.3. Preparation and activity assay of the recombinant six-histidine tagged *Plasmodium falciparum* SHMT (His$_6$-*Pf*SHMT)

The recombinant His$_6$-*Pf*SHMT was prepared as described previously [94, 95] with slight modification. In brief, the pET100/D-*pfshmt* overexpression to produce the recombinant His$_6$-*Pf*SHMT was carried out in *Escherichia coli* BL21 (DE3) at 16 °C in ZY autoinduction medium system. Unless otherwise specified, the purification of the recombinant His$_6$-*Pf*SHMT was carried out at 4 °C. The cell paste harboring the recombinant His$_6$-*Pf*SHMT was resuspended in a buffer

A (50 mM HEPES, pH 7.45 containing 200 mM NaCl and 10% glycerol) containing 10 mM imidazole, 10 μM PLP and 100 μM PMSF, and was then lysed by ultrasonication. The crude extract obtained after three rounds of centrifugation at 35,000 ×g for 60 min was purified to homogeneity by affinity chromatography using Ni-chelating Sepharose column pre-equilibrated with buffer A containing 10 mM imidazole. The column was washed sequentially with buffer A containing 10- and 100-mM imidazole, respectively. The column was then eluted with buffer A containing a linear gradient of 100-300 mM imidazole. Fractions containing His$_6$-*Pf*SHMT were pooled and then added with excess PLP before concentration by ultrafiltration technique. The concentrated enzyme solution was exchanged into buffer B (50 mM HEPES, pH 7.45 containing 1 mM DTT and 0.5 mM EDTA) by gel-filtration chromatography using a Sephadex G-25 column. The collected eluent was concentrated by ultrafiltration technique and then added with twofold excess PLP before storage at -80 °C.

The activity of His6-*Pf*SHMT was measured at 25 °C by the enzyme-coupled assay method using NADP+-dependent 5,10-methylenetetrahydrofolate dehydrogenase (MTHFD) as a coupling enzyme [95]. The typical assay reaction was carried out in buffer C (50 mM HEPES, pH 7.5 containing 1 mM DTT and 0.5 mM EDTA) containing 0.2 mM THF, 3 mM L-serine, 0.25 mM NADP+, 10 μM MTHFD, and 1 μM His6-*Pf*SHMT. The assay reaction was monitored for NADPH production at 375 nm and one unit of SHMT activity is defined as 1 μmol of NADPH produced per min at pH 7.5 and 25 °C.

2.4. Screening of *Pf*SHMT inhibitors

Eight candidate compounds – amphotericin B, dihydroergocristine mesylate, rifabutin, rifaximin, nystatin, tubocurarine, digitoxin, and digoxin – obtained from molecular docking approaches were examined for their ability to inhibit the His$_6$-*Pf*SHMT activity. The enzyme inhibition assays were performed similar to the enzyme activity assay described above, except that 100 μM of each compound was also added into the reaction. The initial rate of each reaction was measured and compared to the control reaction. It should be noted that the concentration of DMSO (a solvent used for solubilizing compound) in all inhibition assays was fixed at 1% (v/v), which did not affect the His$_6$-*Pf*SHMT activity within 3 h (**Fig. B1**).

2.5. Determination of the half maximal inhibitory concentration (IC$_{50}$) value for *Pf*SHMT inhibitors

According to the results obtained from inhibition assay screening, it was found that dihydroergocristine mesylate, digoxin, rifabutin, and amphotericin B were able to inhibit the His$_6$-*Pf*SHMT activity for about 20-50%. Unfortunately, these compounds and the other rest, except amphotericin B, at a concentration >100 µM was insoluble in the assay reaction. Therefore, only amphotericin B was further analyzed for determination of the IC$_{50}$ value.

To determine the IC$_{50}$ value for amphotericin B, the His$_6$-*Pf*SHMT activity was measured at various concentrations of amphotericin B (20, 50, 100, 120, 150, and 172 µM) and compared to the control reaction. The remaining activity of each reaction was determined and plotted against concentration of each compound added into the reaction. The IC$_{50}$ value can be estimated from the curve plot fitted by an equation ([Y = Bottom + (Top − Bottom)/(1 + 10^((LogIC50-X)*HillSlope))]) in GraphPad Prism 7.0 using a symmetrical sigmoidal distribution with variable slope (four-parameter dose response fit), where top and bottom values represented the constraint values at upper and lower limits, and X denotes the concentration of amphotericin B.

2.6. Kinetics of His$_6$-*Pf*SHMT inhibition by amphotericin B

To elucidate the kinetic mechanism of His$_6$-*Pf*SHMT inhibition by amphotericin B, various concentrations of amphotericin B (20 to 172 µM) were added into the enzyme assay reaction. The initial rates were measured at different concentrations of amphotericin B and varying concentrations of one substrate (L-serine, 0.1 to 6.4 mM; or THF, 0.005 to 0.2 mM) at a fixed concentration of another substrate (L-serine, 3 mM; or THF, 0.2 mM). The double reciprocal plots of initial rates and substrates at different concentrations of inhibitor were analyzed using **Equations 3.1** and **3.2** for competitive and non-competitive inhibitions, respectively, where v and V represent the initial and maximum velocities, A and I are the substrate and inhibitor concentrations, K_A is the Michaelis constant for substrate, and K_{is} and K_{ii} are the inhibition constant obtained from the secondary plots of slope and intercept, respectively, versus inhibitor [96].

$$v = \frac{VA}{K_A\left(1 + \dfrac{I}{K_{is}}\right) + A} \qquad \text{(Equation 3.1)}$$

$$v = \frac{VA}{K_A\left(1 + \dfrac{I}{K_{is}}\right) + A\left(1 + \dfrac{I}{K_{ii}}\right)} \qquad \text{(Equation 3.2)}$$

2.7. Preparation of *Pf*SHMT structure for MD simulations

According to the enzyme inhibition assay, the *Pf*SHMT crystal structure (PDB entry 4O6Z [55]) was selected as the protein target for MD simulations. Amphotericin B, a hit compound with the lowest IC_{50} value and PLS from *Pv*SHMT/PLS (PDB entry 4PFN [42]), were then superimposed on another chain (chain B for *Pv*SHMT and chain D for *Pf*SHMT) for amphotericin B and two chains for PLS using the UCFS Chimera version 1.16 program [87]. As the standard procedure [43-45], the partial atomic charges of PLS in the protonated ketoenamine form [41] and amphotericin B were calculated with HF/6-31G(d) level of theory using the Gaussian09 program [60]. The AMBER ff19SB force field [97] was applied for the protein, and the generalized AMBER force field version 2 (GAFF2) [62] was treated to ligands using the Antechamber module of the AMBER20 program [98]. The protonation states of all ionizable groups in *Pf*SHMT were predicted at pH 7.0 using the PROPKA 3.1 program in PDB2PQR server [63]. The *Pf*SHMT/PLS/amphotericin B complex with the water molecules from the crystal structure was energy-minimized using 2,500 steps of steepest descents (SD) followed by 2,500 steps of the conjugate gradient (CG) approach. Then, the minimized structure was solvated by a truncated octahedral box of TIP3P water molecules with a 12 Å space cutoff and neutralized by the addition of Na+ ions. The solvated system was then energy-minimized by the above-described method with a force constant of 50.0 kcal/mol/Å^2 to restrain the protein-heavy atoms. Next, the whole complex was minimized without a forced constraint to relax the structure before the MD simulations.

2.8. Molecular dynamics simulations and analysis

From the previous study [45], the potent SHMT inhibitors (pyrazolopyran(+)-85 and pyrazolopyran(+)-86) were investigated against PvSHMT and PfSHMT by 500-ns MD simulations using the AMBER16 packaged program [46]. Subsequently, MD simulations of the chosen ligand (amphotericin B) in the PfSHMT/PLS complex was performed under the periodic boundary condition using the AMBER20 packaged program [98] for 500 ns with two replications. a 12 Å of distance cutoff was set for non-bonded interactions. The SHAKE algorithm [66, 67]was applied to all covalent bonds containing hydrogen atoms. The system was heated up from 10.0 to 298.15 K at 100 ps and then was equilibrated at 298.15 K for 100 ps. The simulation was carried out using an NPT ensemble with 1 atm pressure for 500 ps. Next, the MD simulation of a complex was conducted for 500 ns using an integration time step of 2 fs. Afterward, the MD trajectories at the last 100 ns were extracted for further structural analyses using the CPPTRAJ module [68] of the AMBER20 program [98]. H-bond interaction, the per-residue decomposition free energy ($\Delta G_{\mathrm{bind}}^{\mathrm{residue}}$) and the solvated interaction energies (SIE)-based binding free energy (ΔG_{SIE}) [71, 72] were calculated using the CPPTRAJ module [68], MMPBSA.py module [73] and the sietraj software [71, 72], respectively.

3. Results and Discussion

3.1. Molecular docking

Drug virtual screening by molecular docking method was used to evaluate the 2,509 FDA-approved drugs against $Plasmodium$ SHMTs for drug repurposing of antimalarial treatment. In this project, only the AutoDock VinaXB program [74] was used to screen the potential inhibitors of $Plasmodium$ SHMTs. The searching and scoring function were set by the providing program force field. The distance, angle, bond, and atom type of the system were mapped to the program library and predicted the binding energy of the compounds. For the AutoDock VinaXB program, the genetic algorithm (GA) and the force-field based scoring were applied for searching and scoring functions. The genetic algorithm was a searching method based on natural selection and the force-field based scoring was a scoring function based on the AMBER force field [99].

The library might be fit for some compound structures. Therefore, the screening of FDA-approved drugs should be further investigated by the other docking programs to get more accuracy results. However, the docking results showed that all drugs were docked at the same position of *Pv*SHMT/PLS and *Pf*SHMT/PLS complexes due to the high similarity in protein 3D structure and high identity of amino acid sequence in the binding pocket (see ***Plasmodium*** **SHMT structures** section above). The docking energy (ΔG_{vinaXB}) of 2,509 FDA-approved drugs were plotted in **Fig. 3.2A**. The compounds with a significantly different score from others of each complex were defined as outliers. The more negative outlier members were then ranked by the ΔG_{vinaXB}. The top twenty-five lowest ΔG_{vinaXB} values (~ –12 to –19 kcal/mol) of each SHMT complex were chosen to be visualized in **Fig. 3.2B**. The eleven of the top twenty-five hit compounds were found in all seven SHMT structures *i.e.*, digoxin (DB00390), acetyldigitoxin (DB00511), rifabutin (DB00615), nystatin (DB00646), amphotericin B (DB00681), tubocurarine (DB01199), rifaximin (DB01220), digitoxin (DB01396), dihydroergocornine (DB11273), lurbinectedin (DB12674), and dihydroergocristine (DB13345). The molecular weight of the considered compounds was ~560 to 920 g/mol (**Table B1**), more than that of THF by around two times (445.4292 g/mol [93]). However, the centroid position of eleven molecules was found at the nearby area of THF in the *Pf*SHMT binding pocket (**Fig. 3.2A, inset**). The ΔG_{vinaXB} was also less than the reference compounds; pyrazolopyran-based inhibitors, THF, and antimalarial drugs. Moreover, many parts of these compound structures consisted of hydroxy groups (**Table B1**). Therefore, binding affinity could be greater. However, with cost and limitation of time, only eight compounds in **Table 3.1**, *i.e.*, digoxin, rifabutin, nystatin, amphotericin B, tubocurarine, rifaximin, digitoxin, and dihydroergocristine, were selected for further *Plasmodium* SHMT inhibitory activity assay.
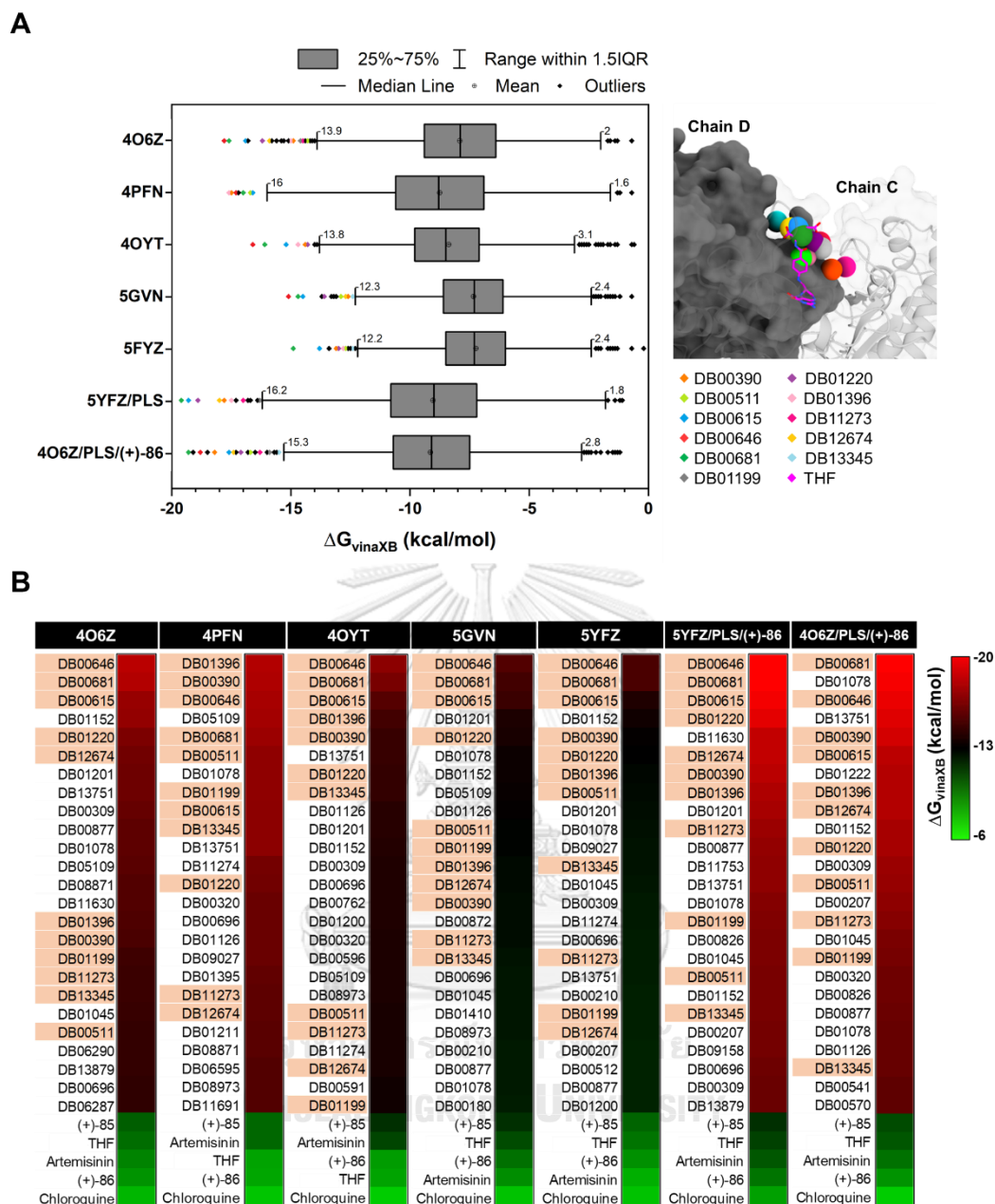
Fig. 3.2 (**A**) The docking energy ($\Delta G_{\mathrm{vinaXB}}$) of 2,509 FDA-approved drugs interacting with *Pv*SHMT and *Pf*SHMT complexes. Inset of **A** is centroids of eleven hit compounds compared to THF in *Pf*SHMT binding pocket (PDB entry 4O6Z [55]). (**B**) The heat map visualization of the twenty-five hit compounds which exhibited the lowest $\Delta G_{\mathrm{vinaXB}}$ in *Pv*SHMT and *Pf*SHMT complexes. Note that the highlighted name indicates the eleven potent compounds which were found in seven *Plasmodium* SHMT complexes.

Table 3.1 The eight potent compounds from molecular docking analysis for *Pf*SHMT inhibitory activity assay [93].

Name	Drug activity
Digoxin (DB00390)	• Treatment of mild to moderate heart failure • Treatment for ventricular response rate control in chronic atrial fibrillation
Rifabutin (DB00615)	• An antibiotic for mycobacterium avium complex disease in patients with HIV.
Nystatin (DB00646)	• A mixture of antifungal polyenes
Amphotericin B (DB00681)	• An antifungal for serious fungal infections and leishmaniasis
Tubocurarine (DB01199)	• A non-depolarizing neuromuscular blocking agent
Rifaximin (DB01220	• An antibiotic for gastrointestinal bacterial infections
Digitoxin (DB01396)	• A cardiac glycoside used for congestive cardiac insufficiency, arrhythmias, and heart failure
Dihydroergocristine (DB13345)	• An ergot alkaloid for delaying progressive mental decline in conditions like Alzheimer's

3.2. Screening of *Pf*SHMT inhibitors

To investigate the candidate compounds, including amphotericin B, dihydroergocristine mesylate, rifabutin, rifaximin, nystatin, tubocurarine, digitoxin, and digoxin, obtained from molecular docking approaches can be potential inhibitors of His_6-*Pf*SHMT, the enzymatic reaction was assayed in the presence of each compound (100 μM) and compared to the control reaction. The result in **Fig. 3.3A** showed that dihydroergocristine mesylate, digoxin, rifabutin, and amphotericin B can inhibit His_6-*Pf*SHMT activity for about 20‑50% relatively compared to the control reaction, while the rest compounds cannot. It was interesting to note that all compounds, except amphotericin B, get precipitated in the assay reaction when their concentrations were more

than 100 µM (data not shown). Therefore, only amphotericin B was further investigated to determine the IC_{50} value (see the next result).

As the rest compounds have limited in solubility only at 100 µM and shown less capability to inhibit His_6-PfSHMT than amphotericin B, we therefore investigate further if these compounds at 100 µM could exhibit time-course inhibition of His_6-PfSHMT activity. Our results shown in **Fig. A2** demonstrated that, after 1-to-3 h incubation, rifaximin can inhibit the His_6-PfSHMT activity as high as 60% relatively compared to the control reaction. While tubocurarine and digitoxin, and dihydroergocristine mesylate and rifabutin exhibited about 40% and 25% inhibition, respectively, after 3 h incubation. In contrast, digoxin and nystatin showed no any significant inhibition after 3 h incubation. The data indicated that rifaximin, tubocurarine, digitoxin, dihydroergocristine mesylate, and rifabutin were slow inhibitors for His_6-PfSHMT. It is interesting to note that even though nystatin has the chemical structure related to amphotericin B, it cannot inhibit the His_6-PfSHMT as similar as amphotericin B.

3.3. IC_{50} value of amphotericin B

The screening of His_6-PfSHMT inhibitors in the above section indicated that amphotericin B is a potent His_6-PfSHMT inhibitor that can be miscible in the assay reaction. Therefore, we measured His_6-PfSHMT at various concentrations of amphotericin B ranged from 20 to 172 µM and determined its IC_{50} value accordingly. The result in **Fig. 3.3B** showed that, based on the plot of % remaining activity versus the logarithm of amphotericin B concentration, the IC_{50} value of amphotericin B was 106 ± 1 µM. The concentration of each candidate compound was diluted from a very high concentration of stock (mM scale) for the enzyme inhibitory assay. It was started by 10 µM and increased to 100 µM. The remaining activity of *Plasmodium* SHMT suggested that concentration of 10 µM could not inhibit the activity of this enzyme. Therefore, the concentration of 100 µM and higher were studied in this project. The IC_{50} of the promising molecule, amphotericin B, was 106 ± 1 µM. It was higher than the IC_{50} of pyrazolopyran inhibitors from the previous work (90 ± 4 and 97 ± 1 nM for pyrazolopyran(+)-85 and (+)-86, respectively [20]). These might be results from the molecular weight of amphotericin B, which was 924.079 g/mole higher than that of pyrazolopyran inhibitors (~460 g/mole [93]). The

different %DMSO could affect the inhibitory result. In this study, 1% DMSO was used for the *Pf*SHMT inhibitory assay, while 5% DMSO was used in the pyrazolopyran inhibitory assay [20].
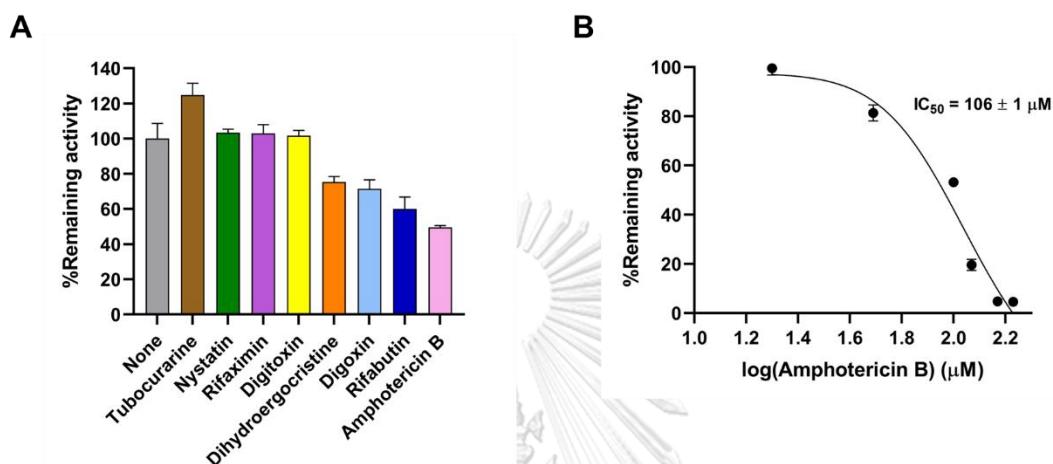
Fig. 3.3 (**A**) Screening of the His_6-*Pf*SHMT inhibitors. The activity of His_6-*Pf*SHMT was measured in the presence of 100 µM of each candidate compound, including tubocurarine, nystatin, rifaximin, digitoxin, dihydroergocristine mesylate, digoxin, rifabutin, and amphotericin B, relatively compared to the control reaction. Error bars represent standard deviations (S.D.) from three replications of the data. (**B**) The IC_{50} value of amphotericin B towards the His_6-*Pf*SHMT inhibition. The activity of His_6-*Pf*SHMT was measured in the presence of different concentrations of amphotericin B (20 to 172 µM), relatively compared to the control reaction. Error bars represent standard deviations (S.D.) from three replications of the data.

3.4. Inhibition mechanism of amphotericin B

The inhibition kinetics of amphotericin B towards His_6-*Pf*SHMT reactions were characterized in order to describe the inhibition mechanism of amphotericin B. The results in **Figure 4** demonstrated the double-reciprocal (primary) plots of e/*v* versus either L-serine **(Fig. 3.4A)** or THF **(Fig. 3.4B)**, respectively, at different concentrations of amphotericin B, which can be used to characterize type of the inhibition mechanism. The primary plot of e/*v* versus L-serine concentration at increasing concentrations of amphotericin B **(Fig. 3.4A)** showed the

pattern of converging lines that intersect on the left side of the *Y*-axis, indicative for non-competitive inhibition mechanism. Based on the primary plot, two inhibition constant values, K_{is} and K_{ii}, can be determined from the secondary plots of primary slopes **(Fig. 3.4A, inset 1)** and intercepts **(Fig. 3.4A, inset 2)** versus amphotericin B, respectively, which were estimated as 18 and 48 μM, respectively **(Table 3.2)**. In contrast, the primary plot of e/*v* versus THF concentration at increasing concentrations of amphotericin B **(Fig. 3.4B)** showed the intersecting lines on the *Y*-axis, which indicates the competitive inhibition mechanism. The secondary plot of primary slopes versus amphotericin B **(Fig. 3.4B, inset)** yielded the estimated K_{is} value of 59 μM **(Table 3.2)**. Based on amphotericin B structure, it could be explained that amphotericin B impede THF binding by competing with THF substrate to bind at the active site, while it is non-competitively with respect to L-serine substrate (**Fig. 3.4C**). The data suggest that amphotericin B can be a promising inhibitor for His_6-*Pf*SHMT. For the binding pocket of amphotericin B, it was predicted from the genetic algorithm (GA) of the AutoDock VinaXB program [99], which was located above the THF binding pocket of *Plasmodium* SHMT. However, some part of the THF binding pocket (loop4) exhibited the interaction with amphotericin B (**Fig. 3.4C**). This binding position of amphotericin B might interfere the THF binding on *Plasmodium* SHMT binding pocket. The performing of MD simulation along 500 ns of *Pf*SHMT/PLS/amphotericin B revealed the stability of amphotericin B on its binding site. The 10 snapshots from the last 100-ns MD simulation showed a similar position of amphotericin B on *Pf*SHMT surface (**Fig. 3.4C**). This could be referred to the correction of amphotericin B binding site on *Plasmodium* SHMT, which was suggested from the searching method of the AutoDock VinaXB program.
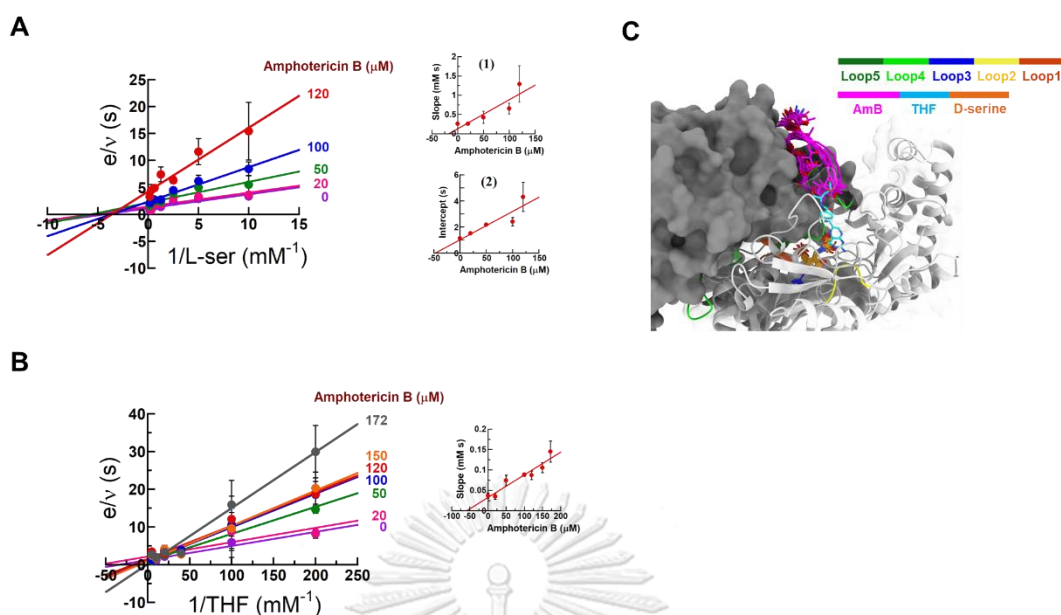
Fig. 3.4 Mechanism of His$_6$-*Pf*SHMT inhibitions by amphotericin B. The double-reciprocal (primary) plots of initial rates and (**A**) L-serine and (**B**) THF substrate at different concentration of inhibitor, amphotericin B (0-172 μM). Insets (**1**) and (**2**) of A are the secondary plots of slopes and intercepts obtained from the primary plot, respectively, versus amphotericin B. Inset of (**B**) is the secondary plot of slope obtained from the primary plot versus amphotericin B. The inhibition constant values obtained from these plots were summarized in **Table 3.2**. Error bars represent standard deviations (S.D.) obtained from three replications of the data. (**C**) The position of amphotericin B from the last 100-ns MD simulations compared to THF substrate in the binding pocket of *Pf*SHMT.

Table 3.2 The estimated inhibition constant values of amphotericin B for His$_6$-*Pf*SHMT inhibitions.

Varying substrate	Amphotericin B (μM)		Type of inhibition
	K_{is}	K_{ii}	
L-serine	18	48	Non-competitive
THF	59	ND	Competitive

ND, not determined

3.5. *Plasmodium* SHMT complexes stability

The root-mean-square deviation (RMSD) for the protein backbone atoms (*i.e.*, N, C, O, and CA) of *Pf*SHMT/PLS bound with amphotericin B was calculated along 500-ns MD simulations to determine complex stability in an aqueous solution. The backbone RMSD of *Pf*SHMT/PLS/amphotericin B complex (**Fig. 3.5, Top**) gradually increased at the first and then slightly fluctuated by ~1.0 to 1.8 Å in three replications. This result indicated that all the complexes reached equilibrium along with 500-ns MD simulations and the last 100 ns could be the most stable phase of these three replications for further analysis. However, the radius of gyration (R_g), the number of intermolecular hydrogen bonds (# H-bond), and the number of atom contacts (# atom contact) indicated the high conformational stability in replicate 1 which exhibited the strong contact of amphotericin B on *Pf*SHMT. Therefore, replicate 1 was then selected as the representative system for the next analysis below. It should be noted that other investigations were performed on the representative chain which exhibited a greater binding interaction to *Pf*SHMT.
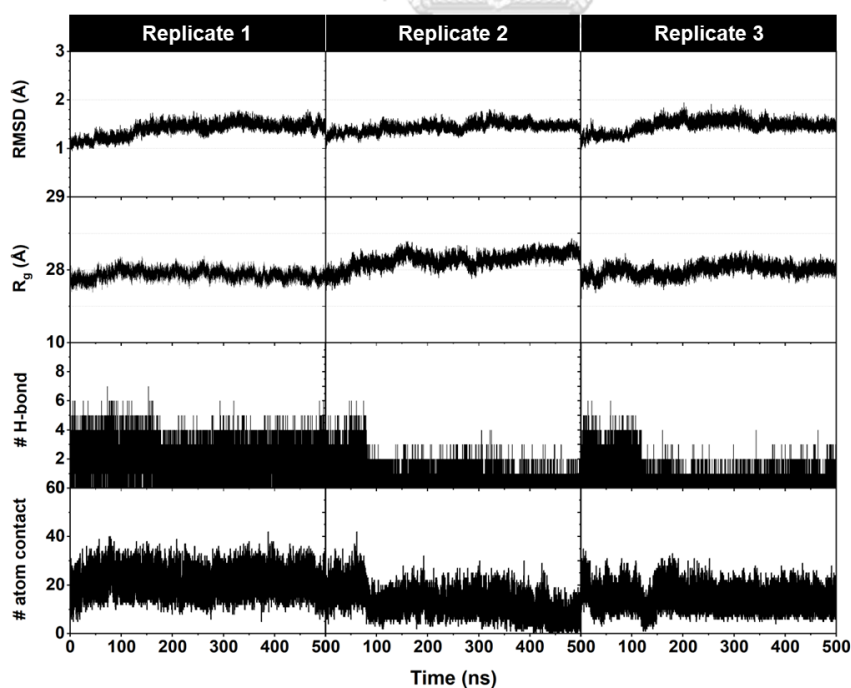
Fig. 3.5 The backbone root-mean-square deviation (RMSD), the radius of gyration (R_g), the number of intermolecular hydrogen bonds (# H-bond), and the number of atom contacts (# atom

contact) of the three replications of *Pf*SHMT/PLS/amphotericin B complex along with the 500-ns MD simulations.

3.6. Amphotericin B binding affinity

The solvated interaction energies (SIE)-based binding free energy (ΔG_{SIE}) was performed to analyze the binding affinity [71, 72] of amphotericin B on *Pf*SHMT/PLS complex. The calculation of the representative replication was conducted from the 100 snapshots extracted from the last 100-ns MD simulations. **Table 3.3** showed that the electrostatic energy (ΔE_{ele}) played an important role in the molecular complexation of *Pf*SHMT/PLS/amphotericin B (−55.31 ± 0.98 kcal/mol) rather than the van der Waals interaction (ΔE_{vdW}) (−46.74 ± 0.44 kcal/mol). In comparison to pyrazolopyran-based inhibitors which was in the same location as THF substrate on *Plasmodium* SHMT, the ΔE_{vdW} was a major driving force [45] in forming of *Plasmodium* SHMT/PLS/pyrazolopyran inhibitors. This different binding site resulted in the different main driving force of complexation between amphotericin B and pyrazolopyran-based inhibitors on *Plasmodium* SHMT. In summary, although the ΔG_{exp} of amphotericin B was not in a good range compared to pyrazolopyran(+)-86 [20], the ΔG_{SIE} predicted from the computational approach suggested a good binding affinity of amphotericin B within the ligand-binding pocket of *Plasmodium* SHMT.

To predict the interaction between amphotericin B and residues around the binding area on *Plasmodium* SHMT, a $\Delta G_{\text{bind}}^{\text{residue}}$ based on the MM/GBSA method was calculated for each residue. The result in **Fig. 3.6A** showed that there were thirteen key residues which exhibited the $\Delta G_{\text{bind}}^{\text{residue}}$ less than −0.5 kcal/mol, including Y58, P59, Y63, Y78, N95, F249, K251, N262, Q259, F266, P267, and V365. Most of these key residues were not reported with any important role involved in ligand binding. However, N262 exhibited the lowest $\Delta G_{\text{bind}}^{\text{residue}}$ to amphotericin B by −6.03 kcal/mol. For K251, the residue in the short loop of *Pf*SHMT relating to the flap motif of human SHMT [55], exhibited a strong interaction to amphotericin B by −3.15 kcal/mol. Moreover, Y63, F266 and V365, stabilizing key residues of THF and pyrazolopyran inhibitors [45, 55, 59], showed the $\Delta G_{\text{bind}}^{\text{residue}}$ of −0.73, −2.68 and −0.67 kcal/mol, respectively. For other key residues Y58, P59, Y78, G93, N95, F249, Q259 and P267 exhibited the $\Delta G_{\text{bind}}^{\text{residue}}$ of −2.97, −0.61,

–1.94, –0.90, –0.55, –0.64, –1.50 and –1.60 kcal/mol, respectively. However, C364 exhibited unfavorable interactions to amphotericin B with $\Delta G_{\text{bind}}^{\text{residue}}$ of 0.70 kcal/mol. These prediction results provided the thirteen critical pocket residues of *Pf*SHMT and other binding residues (**Fig. 3.B6**) which are quite different from the key stabilizing residues of THF and pyrazolopyran-based inhibitors. This could be the supportive information for novel inhibitor development targeting *Plasmodium* SHMT.

Table 3.3 The solvated interaction energies (ΔG_{SIE}) and its energy components for *Pf*SHMT in complex with PLS and amphotericin B.

Energy components (kcal/mol)	Replicate 1
ΔE_{vdW}	-46.74 ± 0.44
ΔE_{ele}	-55.31 ± 0.98
$\gamma \cdot \Delta\text{MSA}$	-9.17 ± 0.11
$\Delta G_{\text{bind}}^{\text{R}}$	32.39 ± 1.03
C	-2.89
α	0.10
ΔG_{SIE}	-11.15 ± 0.09
ΔG_{exp}	-5.42

Note: $\Delta G_{\text{bind}}^{\text{R}}$ is the change in the reaction field energy between the free and bound states, calculated by solving the Poisson equation [71, 72], ΔMSA is the change in the molecular surface area upon binding, α represents the global proportionality coefficient relating to the loss of configurational entropy, γ represents the molecular area coefficient, and C represents a constant value. The ΔG_{exp} is converted from the IC$_{50}$ value by the equation $\Delta G_{\text{exp}} \approx -RT\ln(\text{IC}_{50})$, where R is the gas constant (1.987×10^{-3} kcal/mol·K), and T is the temperature in Kelvin.
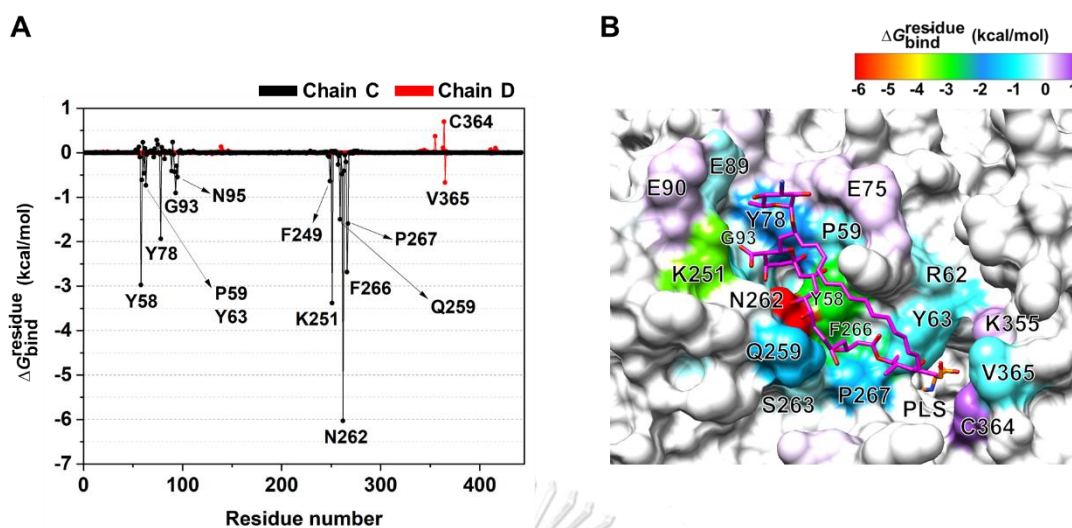
Fig. 3.6 (**A**) $\Delta G_{\text{bind}}^{\text{residue}}$ of *Pf*SHMT/PLS/amphotericin B on the representative chain with the energy cutoff of ± 0.5 kcal/mol. (**B**) The key residues of *Pf*SHMT involved in amphotericin B binding, which were colored according to their $\Delta G_{\text{bind}}^{\text{residue}}$ values.

3.7. Key residues around the amphotericin B binding site

To identify the key residues of *Pf*SHMT around the amphotericin B binding site, pharmacophore modeling was introduced in this work. Pharmacophore modeling was a computational method for the discovery of intermolecular interactions of active compounds with a specific biological target consisting of the H-bond donor (HBD), H-bond acceptor (HBA), hydrophobic interaction (H), and positive (PI) and negative (NI) ionizable groups [100, 101]. In this study, the 10,000 snapshots at the last 100-ns MD simulations of *Pf*SHMT/PLS/amphotericin B were used as a template to create a structure-based pharmacophore model. The 2D, 3D, and representative pharmacophore models (RPMs) in **Fig. 3.7A** indicated that hydrophobic interaction, H-bond contact, and a negative ionizable group were the critical pharmacophore features of *Pf*SHMT/PLS/amphotericin B complex. Y63 and V365 of *Pf*SHMT exhibited the hydrophobic interaction to amphotericin B, while Y78, E90, K251, D258 N262 and F266 showed the H-bond contact with amphotericin B. Y63, F266, and V365 were also previously reported as key residues in forming the interaction to pyrazolopyran-based inhibitors [42, 45, 55, 59]. Additionally, the interaction map (**Fig. B3**) with ≥20% occurrences also suggested high percentages of appearance and occurrences (≥80%) of *Pf*SHMT to amphotericin B including

Y78, K251, N262, F266, and V365. V365 showed hydrophobic interaction to amphotericin B with 94% appearances and occurrences, while a strong H-bond interaction was observed by K251, N262, and F266 (99% appearances and occurrences). For the negative ionizable group, only K251 exhibited 99% occurrences to *Pf*SHMT. These results indicated the preferable environment of *Pf*SHMT/PLS complex to amphotericin B.

The overlaid structure of human cytosolic SHMT (hcSHMT) and *Pf*SHMT showed similarities of structure conformation with RMSD of 0.705 Å (**Fig. 3.7B**). However, human SHMT showed the main part of the flap motif different from *Pf*SHMT. The flap motif or a unique β-hairpin structure of human SHMT including 13 amino acids (273VKSVDPKTGKEIL285), was located on top of the THF binding site [57]. This part is conserved only in the mammalian cytosolic SHMT. However, the superimposition of these two structures showed that the THF binding pocket of *Pf*SHMT was not involved in the flap motif of human SHMT. However, K251, the key residue upon the amphotericin B binding, was indicated as the residue in a short loop related to the flap motif of human SHMT [55]. The interaction of amphotericin B to *Pf*SHMT was involved in many residues (as mentioned above in the **Amphotericin B binding affinity** section). Therefore, only K251 might not affect the interaction of amphotericin B to *Pf*SHMT. The binding of amphotericin B could be specific to *Pf*SHMT and rather than human SHMT.
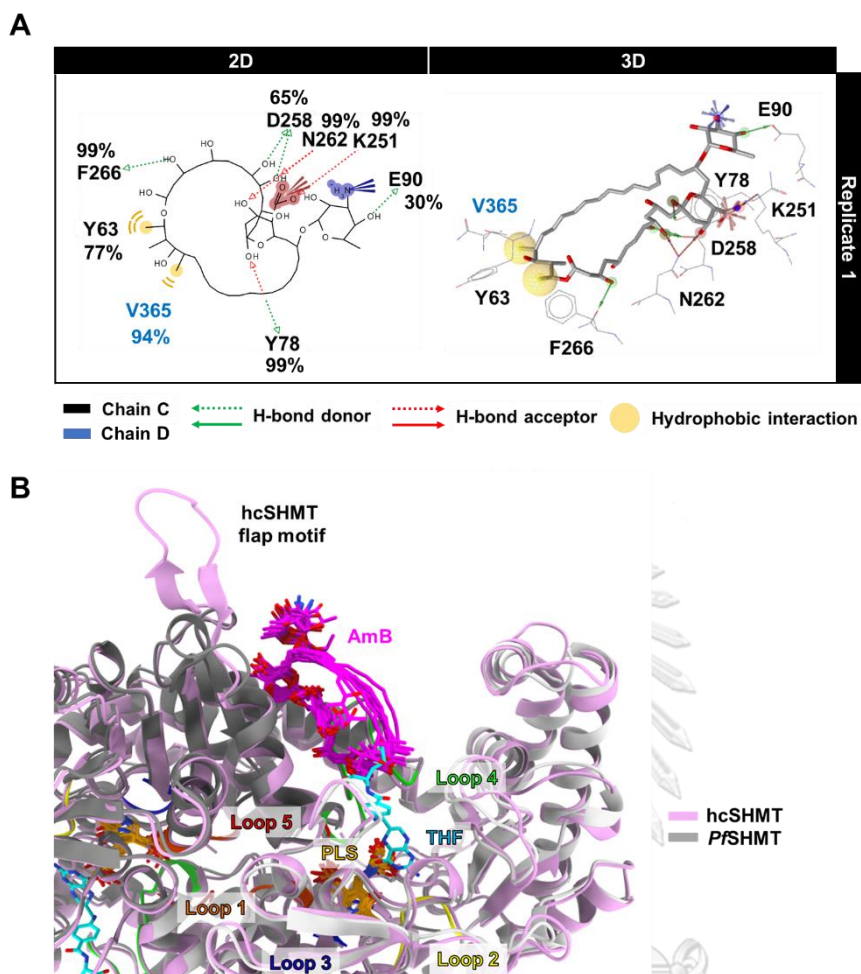
Fig. 3.7 (**A**) Pharmacophore models represented in the 2D and 3Dvisualizations of *Pf*SHMT/PLS/ amphotericin B derived from the last 100-ns MD simulation snapshots. Note that the percentage of occurrences ≥ 20% is labeled in 2D representation. (**B**) The overlaid structures of *Pf*SHMT/PLS/amphotericin B and human cytosolic SHMT (hcSHMT) with RMSD of 0.705 Å. The 10 conformations of amphotericin B in the binding site were extracted from the last 100-ns MD snapshot.

4. Conclusions

The screening of 2,509 FDA‑approved drugs on *Plasmodium* SHMT targets by the molecular docking approach using the AutoDock VinaXB program revealed that eleven hit compounds exhibited significantly lower ΔG_{SIE} than the known SHMT inhibitor pyrazolopyran(+)‑86 and antimalarial drugs artemisinin and chloroquine by approximately 4 to 10 kcal/mol in all seven complexes. However, only eight compounds, *i.e.*, digoxin, rifabutin, nystatin, amphotericin B, tubocurarine, rifaximin, digitoxin, and dihydroergocristine, were further investigated *Plasmodium* SHMT inhibitory assay. The experimental results suggested that amphotericin B was the best inhibitor by the lowest IC$_{50}$ value of 106 ± 1 μM. Moreover, the inhibition mechanism method indicated that amphotericin B could be a promising competitive inhibitor for His$_6$-*Pf*SHMT. To clarify the binding affinity and mode of action of *Pf*SHMT/PLS/amphotericin B, 500‑ns MD simulations were performed. The backbone RMSD suggested high conformational stability of *Pf*SHMT/PLS/amphotericin B complex along with 500‑ns simulations. However, the radius of gyration (R$_g$), the number of H‑bond interactions (# H‑bond) and the number of atoms contact analysis (# atom contact) within the enzyme active site indicated higher complex stability with more favorable binding interaction in replicate 1, which was then selected for further investigations. The solvated interaction energy (ΔG_{SIE}) prediction using 100 snapshots of the last 100‑ns simulations exhibited a preferable interaction of amphotericin B on the *Pf*SHMT/PLS complex than the ΔG_{exp} ~2‑folds, which was exceptional compared to pyrazolopyran(+)‑86. Additionally, the pharmacophore modeling and interaction map indicated that Y78, K151, N262, F266, and V365 were the essential binding residues to amphotericin B. Our findings presented here can identify a new promising inhibitor against *Plasmodium* SHMTs which is the FDA‑approved drug with known activity. Moreover, the experimental and computational results in this work could provide a new core structure which differs from the previous SHMT inhibitors.

Acknowledgments

จุฬาลงกรณ์มหาวิทยาลัย
CHULALONGKORN UNIVERSITY

CONCLUSIONS

This study was separated into three projects. The first project, an unclear catalytic mechanism of *Plasmodium* serine hydroxymethyltransferase (SHMT) was investigated following the retro-aldol proposed scheme by the combined quantum mechanics/molecular mechanics molecular dynamics (QM/MM MD) simulation using the AMBER16 program. E56 and Y64 were selected as a general base and a general acid which played important roles in the reaction. The wild-type and E56A mutations complexes were studied as complete and unfinished models for the SHMT catalytic mechanism, respectively. The PM6 and AM1/D levels of theory were applied to the QM part and the AMBER force field was treated to the MM part. The computational results revealed that the first step of catalytic mechanism was conducted. However, it could not move to other steps as proposed in the representative scheme. These might be the effects of unfavorable conditions and methods to the QM region of *Plasmodium* complex. Another level of theory should be applied with the faster calculation tool of QUICK module of the AMBER20 program.

The second study aims to investigate and clarify the structural dynamics and binding affinity of pyrazolopyran-based inhibitors, pyrazolopyran(+)-85 and pyrazolopyran(+)-86 on *Plasmodium* SHMTs by the MD simulation approach. The results of the 500-ns simulations suggested that pyrazolopyran(+)-85 and pyrazolopyran(+)-86 could bind well within the binding pocket of *Pv*SHMT and *Pf*SHMT. The solvated interaction energy (ΔG_{SIE}) exhibited the greater binding affinity of pyrazolopyran(+)-86 than pyrazolopyran(+)-85 by ~2 kcal/mol, supported by the stronger ligand-protein hydrogen bonding and the lower solvent accessibility within the enzyme active site. The per-residue decomposition free energy analysis also showed that residues L124, G128, H129, L130, K139, N356, and T357 are essential for inhibitor binding. These computational results could provide information for novel SHMT inhibitor design based on pyrazolopyran(+)-86 core structure. The rational structure-based drug design revealed that the isopropyl moiety on the pyrazolopyran core should be changed to the negatively charged group (e.g., carboxylate group) for interacting with the positively charged residue R371. Alternatively, the phenolic compounds could be substituted with a phenyl or piperidine ring to promote hydrogen bond formation with the surrounding residues. In this first part of our study, computational information provides insights into the mode of inhibition of pyrazolopyran-based

inhibitors and rational ideas for designing novel antimalarial drugs targeting *Plasmodium* SHMTs.

For the third study, the FDA-approved drugs from the Drugbank database were screened against *Plasmodium* SHMTs receptor using the molecular docking method. Eleven hit compounds were found in all studied complexes with lower binding energy than pyrazolopyran-based inhibitors, THF, and antimalarial drugs by approximately ~ 4 to 10 kcal/mol. However, only eight potent compounds, *i.e.*, digoxin, rifabutin, nystatin, amphotericin B, tubocurarine, rifaximin, digitoxin, and dihydroergocristine, were tested on *Pf*SHMT by the enzyme-based assay. Amphotericin B was suggested as the great competitive inhibitor with the lowest IC_{50} value of 106 ± 1 µM. Then was studied by the 500-ns MD simulation method to explore the structural dynamics and binding affinity of amphotericin B. The computational results indicated an exceptional binding affinity of amphotericin B -11.15 ± 0.09 kcal/mol on the *Pf*SHMT compared to those of pyrazolopyran(+)-86 (-11.05 ± 0.09 kcal/mol). Moreover, the pharmacophore modeling showed that Y78, K151, N262, F266, and V365 were key binding residues of *Pf*SHMT to amphotericin B with $\geq 80\%$ occurrences along the last 100-ns simulations. These findings could introduce a new core structure of *Plasmodium* SHMT inhibitor that differs from the previous SHMT inhibitors which could be a rational idea for novel antimalarial drug design.

จุฬาลงกรณ์มหาวิทยาลัย

CHULALONGKORN UNIVERSITY

RESEARCH LIMITATION

1. The QM/MM MD simulation of *Plasmodium* SHMT was performed by the Sander module of the AMBER16 program. This module required the parallel CPU for the calculation. Consequently, the simulation of SHMT catalytic mechanism was conducted for a very long time to finish one reaction.

2. The in vitro or/and in vivo test of the newly designed compounds based on pyrazolopyran inhibitor could not be investigated in this work because of time and cost limitations.

3. Acetyldigitoxin (DB00511), Dihydroergocornine (DB11273), and Lurbinectedin (DB12674), which exhibited a lower binding energy (ΔG_{vinaXB}) by the molecular docking method, were not investigated in this work because of the limitation of time and investment.

SUGGESTION FOR FUTURE STUDY

1. Further study of the *Plasmodium* SHMT should be performed by another method (*e.g.*, QUICK package in AMBER20 for HF and DFT calculations)

2. More ligand databases should be investigated by the structure-based virtual screening approach on *Plasmodium* SHMTs. For the molecular docking method, screening of compounds by other docking programs for the comparison of binding energy could provide greater information.

REFERENCES

1. Araújo, M.S., et al., *Natural Plasmodium infection in monkeys in the state of Rondônia (Brazilian Western Amazon)*. Malaria journal, 2013. **12**(1): p. 1-8.

2. O'Donoghue, P., *Haemoprotozoa: making biological sense of molecular phylogenies.* International Journal for Parasitology: Parasites and Wildlife, 2017. **6**(3): p. 241-256.

3. Garnham, P.C.C., *Malaria parasites and other Haemosporidia*. Malaria Parasites and other Haemosporidia. 1966, Davis, Philadelphia: Blackwell, Oxford, England.

4. Organization, W.H., *World malaria report 2020. 2020*, in *World Health Organization: Geneva*. 2020: Geneva.

5. Singh, B. and C. Daneshvar, *Human infections and detection of Plasmodium knowlesi.* Clinical microbiology reviews, 2013. **26**(2): p. 165-184.

6. Maeno, Y., et al., *Humans frequently exposed to a range of non-human primate malaria parasite species through the bites of Anopheles dirus mosquitoes in South-central Vietnam.* Parasites vectors, 2015. **8**(1): p. 1-7.

7. Amir, A., et al., *Invasion characteristics of a Plasmodium knowlesi line newly isolated from a human.* Scientific Reports, 2016. **6**(1): p. 1-8.

8. Groger, M., et al., *A systematic review of the clinical presentation, treatment and relapse characteristics of human Plasmodium ovale malaria.* Malaria journal, 2017. **16**(1): p. 1-16.

9. Geleta, G. and T. Ketema, *Severe malaria associated with Plasmodium falciparum and P. vivax among children in Pawe Hospital, Northwest Ethiopia.* Malaria research treatment, 2016. **2016**.

10. Organization, W.H., *International travel and health. Geneva: World Health Organization; 2019*. 2019.

11. Noisang, C., et al., *Molecular detection of drug resistant malaria in Southern Thailand.* Malaria journal, 2019. **18**(1): p. 1-11.

12. Tantiamornkul, K., et al., *The prevalence of molecular markers of drug resistance in Plasmodium vivax from the border regions of Thailand in 2008 and 2014.* International Journal for Parasitology: Drugs and Drug Resistance, 2018. **8**(2): p. 229-237.

13. Juge, N., et al., *Plasmodium falciparum chloroquine resistance transporter is a H+-coupled*

polyspecific nutrient and drug exporter. Proceedings of the National Academy of Sciences, 2015. **112**(11): p. 3356-3361.

14.   Su, X.Z., et al., *Plasmodium genomics and genetics: new insights into malaria pathogenesis, drug resistance, epidemiology, and evolution.* Clinical microbiology reviews, 2019. **32**(4): p. e00019-19.

15.   Cowell, A.N. and E.A. Winzeler, *The genomic architecture of antimalarial drug resistance.* Briefings in functional genomics, 2019. **18**(5): p. 314-328.

16.   Le Manach, C., et al., *Identification of a potential antimalarial drug candidate from a series of 2-aminopyrazines by optimization of aqueous solubility and potency across the parasite life cycle.* Journal of medicinal chemistry, 2016. **59**(21): p. 9890-9905.

17.   Marani, M., et al., *A pyrazolopyran derivative preferentially inhibits the activity of human cytosolic serine hydroxymethyltransferase and induces cell death in lung cancer cells.* Oncotarget, 2016. **7**(4): p. 4570.

18.   Imperatore, C., et al., *Exploring the antimalarial potential of the methoxy-thiazinoquinone scaffold: Identification of a new lead candidate.* Bioorganic chemistry, 2019. **85**: p. 240-252.

19.   Witschel, M.C., et al., *Inhibitors of plasmodial serine hydroxymethyltransferase (SHMT): cocrystal structures of pyrazolopyrans with potent blood-and liver-stage activities.* Journal of medicinal chemistry, 2015. **58**(7): p. 3117-3130.

20.   Schwertz, G., et al., *Antimalarial inhibitors targeting serine hydroxymethyltransferase (SHMT) with in vivo efficacy and analysis of their binding mode based on X-ray cocrystal structures.* Journal of Medicinal Chemistry, 2017. **60**(12): p. 4840-4860.

21.   Pang, C.K.T., et al., *Catalytic and ligand-binding characteristics of Plasmodium falciparum serine hydroxymethyltransferase.* Molecular biochemical parasitology, 2009. **168**(1): p. 74-83.

22.   Locasale, J.W., *Serine, glycine and one-carbon units: cancer metabolism in full circle.* Nature Reviews Cancer, 2013. **13**(8): p. 572-583.

23.   Nonaka, H., et al., *Design strategy for serine hydroxymethyltransferase probes based on retro-aldol-type reaction.* Nature communications, 2019. **10**(1): p. 1-10.

24.   Scaletti, E., et al., *Structural basis of inhibition of the human serine*

hydroxymethyltransferase SHMT2 by antifolate drugs. FEBS letters, 2019. **593**(14): p. 1863-1873.

25.   Jain, M., et al., *Metabolite profiling identifies a key role for glycine in rapid cancer cell proliferation.* Science, 2012. **336**(6084): p. 1040-1044.

26.   Asano, K., et al., *Metabolic and chemical regulation of tRNA modification associated with taurine deficiency and human disease.* Nucleic acids research, 2018. **46**(4): p. 1565-1583.

27.   Kufareva, I. and R. Abagyan, *Methods of protein structure comparison*, in *Homology modeling*. 2011, Springer. p. 231-257.

28.   Durrant, J.D. and J.A. McCammon, *Molecular dynamics simulations and drug discovery.* BMC biology, 2011. **9**(1): p. 1-9.

29.   Zhang, Z., et al., *Overcoming cancer therapeutic bottleneck by drug repurposing.* Signal transduction and targeted therapy, 2020. **5**(1): p. 1-25.

30.   Ahmad, S., S. Qazi, and K. Raza, *Translational bioinformatics methods for drug discovery and drug repurposing*, in *Translational Bioinformatics in Healthcare and Medicine*. 2021, Elsevier. p. 127-139.

31.   Rao, N.A., et al., *Structure–function relationship in serine hydroxymethyltransferase.* Biochimica et Biophysica Acta (BBA)-Proteins and Proteomics, 2003. **1647**(1-2): p. 24-29.

32.   Schirch, V. and D.M.E. Szebenyi, *Serine hydroxymethyltransferase revisited.* Current opinion in chemical biology, 2005. **9**(5): p. 482-487.

33.   Rao, J.V.K., et al., *The role of Glu74 and Tyr82 in the reaction catalyzed by sheep liver cytosolic serine hydroxymethyltransferase.* European Journal of Biochemistry, 2000. **267**(19): p. 5967-5976.

34.   Szebenyi, D.M.E., et al., *Serine Hydroxymethyltransferase: Role of Glu75 and Evidence that Serine Is Cleaved by a Retroaldol Mechanism.* Biochemistry, 2004. **43**(22): p. 6865-6876.

35.   Groenhof, G., *Introduction to QM/MM simulations.* Methods in Molecular Biology, 2013. **924**: p. 43-66.

36.   Nutho, B., A.J. Mulholland, and T. Rungrotmongkol, *Quantum mechanics/molecular mechanics (QM/MM) calculations support a concerted reaction mechanism for the Zika virus NS2B/NS3 serine protease with its substrate.* The Journal of Physical Chemistry B,

2019. **123**(13): p. 2889-2903.

37.   Fernandes, H.S., M.J. Ramos, and N.M.F.S.A. Cerqueira, *Catalytic mechanism of the serine hydroxymethyltransferase: a computational ONIOM QM/MM study.* ACS Catalysis, 2018. **8**(11): p. 10096-10110.

38.   Bentzinger, G., et al., *Enantiopure substituted pyridines as promising antimalarial drug candidates.* Tetrahedron, 2020. **76**(15): p. 131088.

39.   Okombo, J. and K. Chibale, *Insights into integrated lead generation and target identification in malaria and tuberculosis drug discovery.* Accounts of chemical research, 2017. **50**(7): p. 1606-1616.

40.   Santatiwongchai, J., D. Gleeson, and M.P. Gleeson, *Theoretical Evaluation of the Reaction Mechanism of Serine Hydroxymethyltransferase.* The Journal of Physical Chemistry B, 2018. **123**(2): p. 407-418.

41.   Soniya, K. and A. Chandra, *Free energy landscapes of prototropic tautomerism in pyridoxal 5'-phosphate Schiff bases at the active site of an enzyme in aqueous medium.* Journal of Computational Chemistry, 2018. **39**(21): p. 1629-1638.

42.   Chitnumsub, P., et al., *Structures of Plasmodium vivax serine hydroxymethyltransferase: implications for ligand-binding specificity and functional control.* Acta Crystallographica Section D: Biological Crystallography, 2014. **70**(12): p. 3177-3186.

43.   Nutho, B. and T. Rungrotmongkol, *Binding recognition of substrates in NS2B/NS3 serine protease of Zika virus revealed by molecular dynamics simulations.* Journal of Molecular Graphics and Modelling, 2019. **92**: p. 227-235.

44.   Nutho, B., et al., *Why Are Lopinavir and Ritonavir Effective against the Newly Emerged Coronavirus 2019? Atomistic Insights into the Inhibitory Mechanisms.* Biochemistry, 2020. **59**(18): p. 1769-1779.

45.   Mee-udorn, P., et al., *Structural dynamics and in silico design of pyrazolopyran-based inhibitors against Plasmodium serine hydroxymethyltransferases.* Journal of Molecular Liquids, 2022. **362**: p. 119737.

46.   Case, D.A., et al., *Amber, vol 16. University of California, San Francisco*. 2016.

47.   BIOVIA, D.S., *The Discovery Studio Visualizer*. 2021: San Diego: Dassault Systèmes.

48.   Kumar, S., et al., *The weighted histogram analysis method for free-energy calculations on*

biomolecules. I. The method. Journal of computational chemistry, 1992. **13**(8): p. 1011-1021.

49.   Organization, W.H., *International travel and health 2012: situation as on 1 January 2012.* 2012: World Health Organization.

50.   Ye, R., Y. Zhang, and D. Zhang, *Evaluations of candidate markers of dihydroartemisinin-piperaquine resistance in Plasmodium falciparum isolates from the China–Myanmar, Thailand–Myanmar, and Thailand–Cambodia borders.* Parasites & vectors, 2022. **15**(1): p. 1-9.

51.   Kuesap, J., et al., *Molecular Markers for Sulfadoxine/Pyrimethamine and Chloroquine Resistance in Plasmodium falciparum in Thailand.* The Korean Journal of Parasitology, 2022. **60**(2): p. 109.

52.   Sharma, M., et al., *Inhibition of Plasmodium falciparum phenylalanine tRNA synthetase provides opportunity for antimalarial drug development.* Structure, 2022.

53.   Shibeshi, M.A., Z.D. Kifle, and S.A. Atnafie, *Antimalarial drug resistance and novel targets for antimalarial drug discovery.* Infection and Drug Resistance, 2020. **13**: p. 4047.

54.   Pornthanakasem, W., et al., *Plasmodium serine hydroxymethyltransferase: indispensability and display of distinct localization.* Malaria journal, 2012. **11**(1): p. 1-9.

55.   Chitnumsub, P., et al., *The structure of Plasmodium falciparum serine hydroxymethyltransferase reveals a novel redox switch that regulates its activities.* Acta Crystallographica Section D: Biological Crystallography, 2014. **70**(6): p. 1517-1527.

56.   Pinthong, C., et al., *Distinct biochemical properties of human serine hydroxymethyltransferase compared with the Plasmodium enzyme: implications for selective inhibition.* The FEBS Journal, 2014. **281**(11): p. 2570-2583.

57.   Ubonprasert, S., et al., *A flap motif in human serine hydroxymethyltransferase is important for structural stabilization, ligand binding, and control of product release.* Journal of Biological Chemistry, 2019. **294**(27): p. 10490-10502.

58.   Maenpuen, S., et al., *Kinetic mechanism and the rate-limiting step of Plasmodium vivax serine hydroxymethyltransferase.* Journal of Biological Chemistry, 2015. **290**(13): p. 8656-8665.

59.   Schwertz, G., et al., *Potent inhibitors of plasmodial serine hydroxymethyltransferase*

(SHMT) featuring a spirocyclic scaffold. ChemMedChem, 2018. **13**(9): p. 931-943.

60.   Frisch, M.J., et al., *Gaussian 09, revision C. 01; Gaussian, Inc: Wallingford, CT, 2010.* 2010.

61.   Maier, J.A., et al.,*ff14SB: Improving the Accuracy of Protein Side Chain and Backbone Parameters from ff99SB.* Journal of Chemical Theory and Computation, 2015. **11**(8): p. 3696-3713.

62.   Wang, J., et al., *Development and testing of a general amber force field.* DA Journal of Computational Chemistry, 2004. **25**(9): p. 1157-1174.

63.   Dolinsky, T.J., et al., *PDB2PQR: an automated pipeline for the setup of Poisson–Boltzmann electrostatics calculations.* Nucleic acids research, 2004. **32**(suppl_2): p. W665-W667.

64.   Essmann, U., L. Perera, and M.L. Berkowitz, *A smooth particle mesh Ewald method.* The Journal of Chemical Physics, 1995. **103**(19): p. 8577-8593.

65.   Darden, T., D. York, and L. Pedersen, *Particle mesh Ewald: An N ·log(N) method for Ewald sums in large systems.* The Journal of Chemical Physics, 1993. **98**(12): p. 10089-10092.

66.   Ryckaert, J.P., G. Ciccotti, and H.J.C. Berendsen, *Numerical integration of a System with Constraints: of the Cartesian Equations of Motion Molecular Dynamics of n-Alkanes.* Journal of Computational Physics, 1977. **23**: p. 327-41.

67.   Miyamoto, S. and P.A. Kollman, *SETTLE: an analytical version of the shake an RATTLE algorithms for molecular simulation.* The Journal of Computational Chemistry 1992. **13**: p. 952-962.

68.   Roe, D.R. and T.E. Cheatham 3rd, *PTRAJ and CPPTRAJ: Software for Processing and Analysis of Molecular Dynamics Trajectory Data.* Journal of Chemical Theory and Computation, 2013. **9**: p. 3084-3095.

69.   Massova, I. and P.A. Kollman, *Combined molecular mechanical and continuum solvent approach (MM-PBSA/GBSA) to predict ligand binding.* Perspectives in Drug Discovery and Design, 2000. **18**(1): p. 113-135.

70.   Kollman, P.A., et al., *Calculating Structures and Free Energies of Complex Molecules: Combining Molecular Mechanics and Continuum Models.* Accounts of Chemical Research, 2000. **33**(12): p. 889-897.

71.   Cui, Q., et al., *Molecular Dynamics—Solvated Interaction Energy Studies of Protein–Protein Interactions: The MP1–p14 Scaffolding Complex.* Journal of Molecular Biology, 2008. **379**(4): p. 787-802.

72.   Naïm, M., et al., *Solvated Interaction Energy (SIE) for Scoring Protein-Ligand Binding Affinities. 1. Exploring the Parameter Space.* Journal of Chemical Information and Modeling, 2007. **47**(1): p. 122-133.

73.   Miller, B.R.I., et al., *MMPBSA.py: An Efficient Program for End-State Free Energy Calculations.* Journal of Chemical Theory and Computation, 2012. **8**(9): p. 3314-3321.

74.   Koebel, M.R., et al., *AutoDock VinaXB: implementation of XBSF, new empirical halogen bond scoring function, into AutoDock Vina.* Journal of Cheminformatics, 2016. **8**(1): p. 27.

75.   Swaminathan, S., W.E. Harte, Jr., and D.L. Beveridge, *Investigation of domain structure in proteins via molecular dynamics simulation: application to HIV-1 protease dimer.* Journal of the American Chemical Society, 1991. **113**(7): p. 2717-2721.

76.   Piao, L., et al., *Molecular Dynamics Simulations of Wild Type and Mutants of SAPAP in Complexed with Shank3.* International Journal of Molecular Sciences, 2019. **20**(1): p. 224.

77.   Meeprasert, A., et al., *Effect of D168V mutation in NS3/4A HCV protease on susceptibilities of faldaprevir and danoprevir.* Molecular BioSystems, 2016. **12**(12): p. 3666-3673.

78.   Murali, P., et al., *Targeting the Autophagy Specific Lipid Kinase VPS34 for Cancer Treatment: An Integrative Repurposing Strategy.* The Protein Journal, 2021. **40**(1): p. 41-53.

79.   Purisima, E.O. and S.H. Nilar, *A simple yet accurate boundary element method for continuum dielectric calculations.* Journal of Computational Chemistry, 1995. **16**(6): p. 681-689.

80.   Purisima, E.O., *Fast summation boundary element method for calculating solvation free energies of macromolecules.* Journal of Computational Chemistry, 1998. **19**(13): p. 1494-1504.

81.   Jagath, J.R., N.A. Rao, and H.S. Savithri, *Role of Arg-401 of cytosolic serine hydroxymethyltransferase in subunit assembly and interaction with the substrate carboxy group.* Biochemical Journal, 1997. **327**(3): p. 877-882.

82.   Chen, D., et al., *Regulation of protein-ligand binding affinity by hydrogen bond pairing.*

Science Advances, 2016. **2**(3): p. e1501240.

83. Baker, E.N. and R.E. Hubbard, *Hydrogen bonding in globular proteins.* Progress in Biophysics and Molecular Biology, 1984. **44**(2): p. 97-179.

84. Renwick, S.B., K. Snell, and U. Baumann, *The crystal structure of human cytosolic serine hydroxymethyltransferase: a target for cancer chemotherapy.* Structure, 1998. **6**(9): p. 1105-1116.

85. Ducker, G.S., et al., *Human SHMT inhibitors reveal defective glycine import as a targetable metabolic vulnerability of diffuse large B-cell lymphoma.* Proceedings of the National Academy of Sciences, 2017. **114**(43): p. 11404-11409.

86. Sow, F., et al., *Genetic diversity of Plasmodium vivax metacaspase 1 and Plasmodium vivax multi-drug resistance 1 genes of field isolates from Mauritania, Sudan and Oman.* Malaria Journal, 2017. **16**(1): p. 61.

87. Pettersen, E.F., et al., *UCSF Chimera—a visualization system for exploratory research and analysis.* Journal of computational chemistry, 2004. **25**(13): p. 1605-1612.

88. Organization, W.H., *Artemisinin resistance and artemisinin-based combination therapy efficacy: status report.* 2018, World Health Organization.

89. Savarino, A., et al., *New insights into the antiviral effects of chloroquine.* The Lancet infectious diseases, 2006. **6**(2): p. 67-69.

90. Mohs, R.C. and N.H. Greig, *Drug discovery and development: Role of basic biological research.* Alzheimer's & Dementia: Translational Research & Clinical Interventions, 2017. **3**(4): p. 651-657.

91. Pushpakom, S., et al., *Drug repurposing: progress, challenges and recommendations.* Nature Reviews Drug Discovery, 2019. **18**(1): p. 41-58.

92. Pillaiyar, T., et al., *A medicinal chemistry perspective of drug repositioning: Recent advances and challenges in drug discovery.* European Journal of Medicinal Chemistry, 2020. **195**: p. 112275.

93. Wishart, D.S., et al., *DrugBank 5.0: a major update to the DrugBank database for 2018.* Nucleic acids research, 2018. **46**(D1): p. D1074-D1082.

94. Maenpuen, S., et al., *Characterization of Plasmodium falciparum serine hydroxymethyltransferase—a potential antimalarial target.* Molecular and biochemical

parasitology, 2009. **168**(1): p. 63-73.

95.   Sopitthummakhun, K., et al., *Plasmodium serine hydroxymethyltransferase as a potential anti-malarial target: inhibition studies using improved methods for enzyme production and assay.* Malaria journal, 2012. **11**(1): p. 1-12.

96.   Cook, P.F. and W.W. Cleland, *Enzyme kinetics and mechanism.* 2007: Garland Science.

97.   Tian, C., et al., *ff19SB: Amino-acid-specific protein backbone parameters trained against quantum mechanics energy surfaces in solution.* Journal of chemical theory and computation, 2019. **16**(1): p. 528-552.

98.   Case, D.A., et al., *Amber 2021. University of California, San Francisco*. 2021.

99.   Yadava, U., *Search algorithms and scoring methods in protein-ligand docking.* Endocrinology & Metabolism International Journal, 2018. **6**(6): p. 359-367.

100.   Deetanya, P., et al., *Interaction of 8-anilinonaphthalene-1-sulfonate with SARS-CoV-2 main protease and its application as a fluorescent probe for inhibitor identification.* Computational and Structural Biotechnology Journal, 2021. **19**: p. 3364-3371.

101.   Sanachai, K., et al., *Identification of repurposing therapeutics toward SARS-CoV-2 main protease by virtual screening.* PloS one, 2022. **17**(6): p. e0269563.

APPENDICES

APPENDIX A

SUPPLEMETARY INFORMATION FOR MANUSCRIPT I

Structural dynamics and *in silico* design of pyrazolopyran‑based inhibitors against *Plasmodium* serine hydroxymethyltransferases

Pitchayathida Mee-udorn[1], Kochakorn Phiwkaow[2], Ruchanok Tinikul[3], Kamonpan Sanachai[4], Somchart Maenpuen[2], and Thanyada Rungrotmongkol[1,4]*

[1]Program in Bioinformatics and Computational Biology, Graduate School, Chulalongkorn University, Bangkok 10330, Thailand

[2]Department of Biochemistry, Faculty of Science, Burapha University, Chonburi 20131, Thailand

[3]Department of Biochemistry and Center for Excellence in Protein and Enzyme Technology, Faculty of Science, Mahidol University, Bangkok 10400, Thailand

[4] Department of Biochemistry, Faculty of Science, Khon Kaen University, Khon Kaen 40002, Thailand

[5]Center of Excellence in Biocatalyst and Sustainable Biotechnology, Department of Biochemistry, Faculty of Science, Chulalongkorn University, Bangkok 10330, Thailand

E-mail address: t.rungrotmongkol@gmail.com, thanyada.r@chula.ac.th

Phone: +66-2218-5426. Fax: +66-2218-541

A1. Protein-inhibitor hydrogen bonding
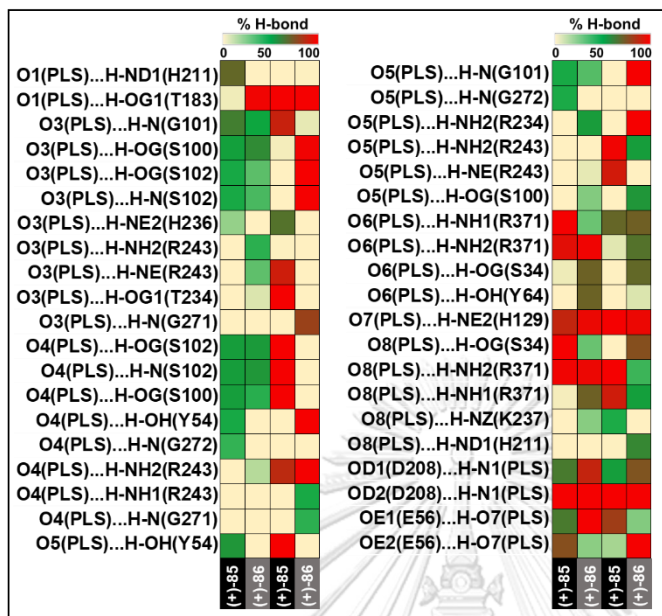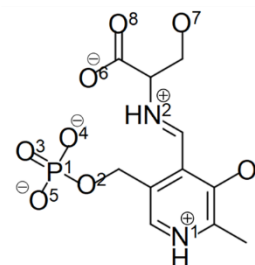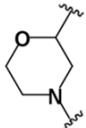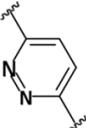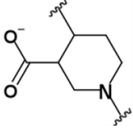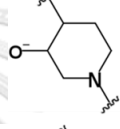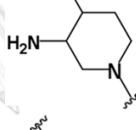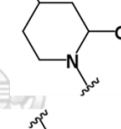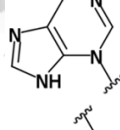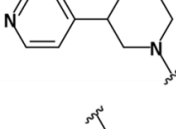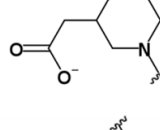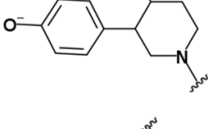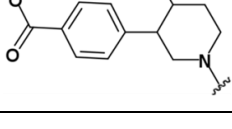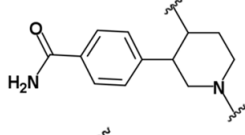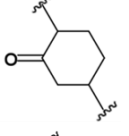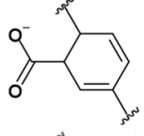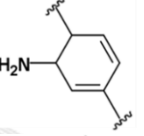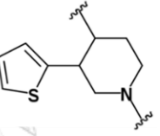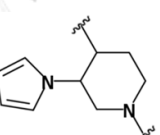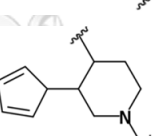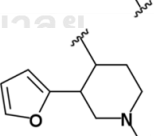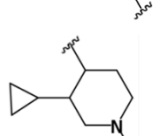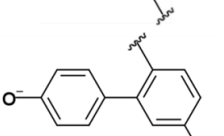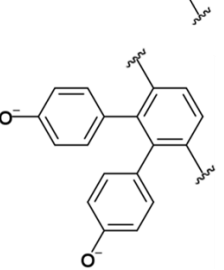
Fig. A1 (**A**) Percentage of H-bond occupation for pyridoxal 5'-phosphate (PLP) with L-serine bound in the Schiff base form (PLS) binding to *Pv*SHMT and *Pf*SHMT with ≥ 40% cut-off (**B**) The 2D structure of PLS in ketoenamine form
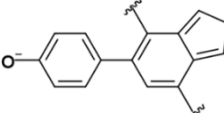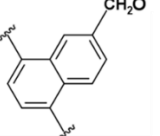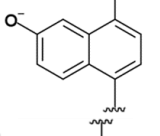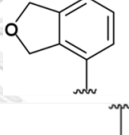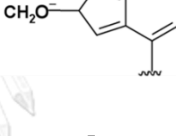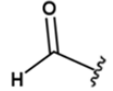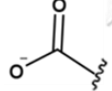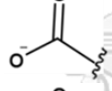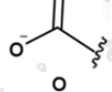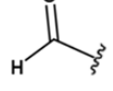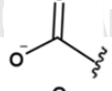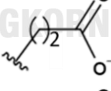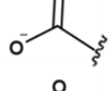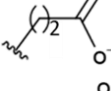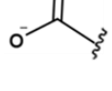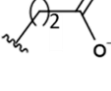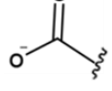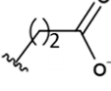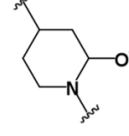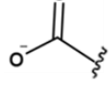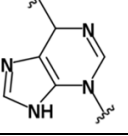
A2. Rational drug design
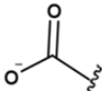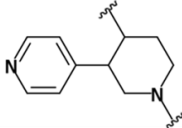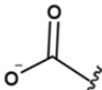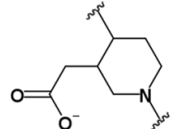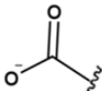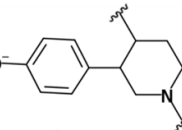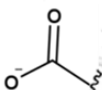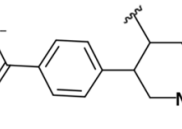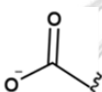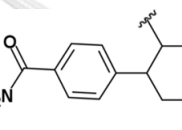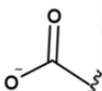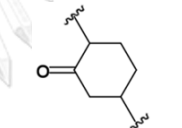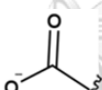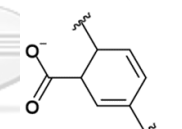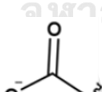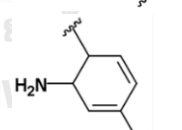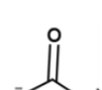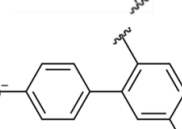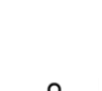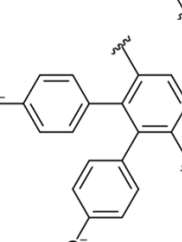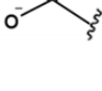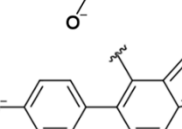
Table A1 The average docking energy (ΔG_{vinaXB}) for the designed pyrazolopyrans, where "-" means the same functional group as the template, pyrazolopyran(+)-86. The analogs with ΔG_{vinaXB} < -12.5 kcal·mol-1 are in bold text.
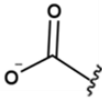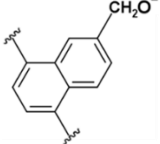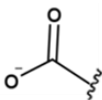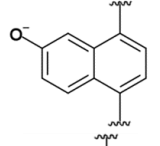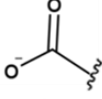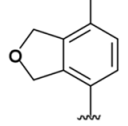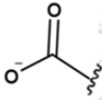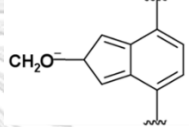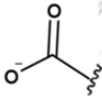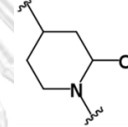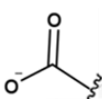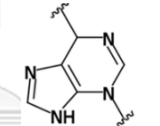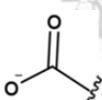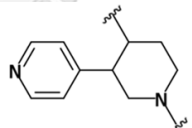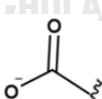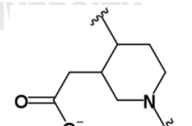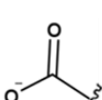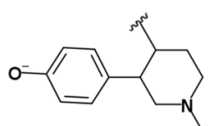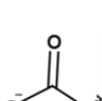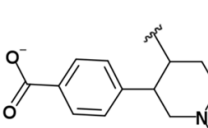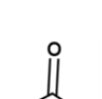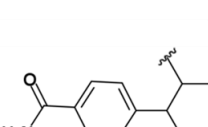
	Methyl (R1)	Isopropyl (R2)	Carboxylate (R3)	Heterocyclic (R4)	Average ΔG_{vinaXB} (kcal·mol-1)
(+)-85	(methyl)	(isobutyl)	(ester, $( )_2$)	(meta-phenyl)	-11.23 ± 0.45
(+)-86/1111	(methyl)	(isobutyl)	(carboxylate)	(N-piperidinyl)	-11.49 ± 0.51
2111	(aldehyde)	-	-	-	-10.76 ± 0.40
3111	(alkoxide)	-	-	-	-10.73 ± 0.46
4111	(H_2N-)	-	-	-	-10.60 ± 0.46
1211	-	(carboxylate)	-	-	-11.27 ± 0.40
1121	-	-	(carboxylate, $( )_2$)	-	-10.96 ± 0.40
1112	-	-	-	(pyridinyl)	-11.08 ± 0.49
1113	-	-	-	(pyrimidinyl)	-10.83 ± 0.49
1114	-	-	-	(pyranyl)	-10.99 ± 0.46

	Methyl (R1)	Isopropyl (R2)	Carboxylate (R3)	Heterocyclic (R4)	Average ΔG_{vinaXB} (kcal·mol^{-1})
1115	-	-	-		-10.40 ± 0.54
1116	-	-	-		-11.23 ± 0.49
1117	-	-	-		-11.38 ± 0.46
1118	-	-	-		-11.47 ± 0.51
1119	-	-	-		-11.08 ± 0.48
11120	-	-	-		-11.52 ± 0.48
11121	-	-	-		-11.86 ± 0.43
11122	-	-	-		-11.67 ± 0.66
11123	-	-	-		-11.33 ± 0.42
11124	-	-	-		-11.78 ± 0.59
11125	-	-	-		-11.58 ± 0.71

	Methyl (R1)	Isopropyl (R2)	Carboxylate (R3)	Heterocyclic (R4)	Average $\Delta G_{\mathrm{vinaXB}}$ (kcal·mol^{-1})
11126	-	-	-		-11.63 ± 0.67
11127	-	-	-		-12.19 ± 0.49
11128	-	-	-		-11.98 ± 0.48
11129	-	-	-		-11.90 ± 0.47
11130	-	-	-		-11.72 ± 0.50
11131	-	-	-		-11.62 ± 0.53
11132	-	-	-		-11.99 ± 0.53
11133	-	-	-		-11.80 ± 0.50
11134	-	-	-		-11.55 ± 0.58
11135	-	-	-		-12.44 ± 0.49
11136	-	-	-		-9.97 ± 1.26
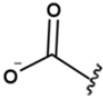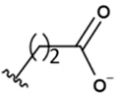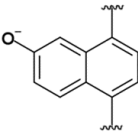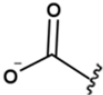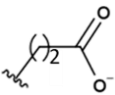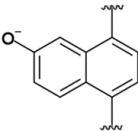
	Methyl (R1)	Isopropyl (R2)	Carboxylate (R3)	Heterocyclic (R4)	Average ΔG_{vinaXB} (kcal·mol^{-1})
11137	-	-	-	*(structure)*	**-12.76 ± 0.77**
11138	-	-	-	*(structure)*	-12.26 ± 0.53
11139	-	-	-	*(structure)*	**-12.57 ± 0.55**
11140	-	-	-	*(structure)*	-12.23 ± 0.47
11141	-	-	-	*(structure)*	-12.06 ± 0.60
2211	*(structure)*	*(structure)*	-	-	-11.35 ± 0.42
3211	*(structure)*	*(structure)*	-	-	-10.88 ± 0.42
4211	*(structure)*	*(structure)*	-	-	-10.83 ± 0.46
2221	*(structure)*	*(structure)*	*(structure)*	-	-10.73 ± 0.44
3221	*(structure)*	*(structure)*	*(structure)*	-	-11.09 ± 0.44
4221	*(structure)*	*(structure)*	*(structure)*	-	-10.90 ± 0.43
12120	-	*(structure)*	*(structure)*	*(structure)*	-11.88 ± 0.42
12121	-	*(structure)*	-	*(structure)*	-12.10 ± 0.42

	Methyl (R1)	Isopropyl (R2)	Carboxylate (R3)	Heterocyclic (R4)	Average ΔG_{vinaXB} (kcal·mol^{-1})
12122	-		-		-12.24 ± 0.60
12123	-		-		-11.57 ± 0.40
12124	-		-		-11.67 ± 0.62
12125	-		-		-12.16 ± 0.59
12126	-		-		-12.26 ± 0.77
12127	-		-		-12.40 ± 0.40
12128	-		-		-12.11 ± 0.45
12129	-		-		-12.17 ± 0.46
12135	-		-		**-12.82 ± 0.51**
12136	-		-		-10.06 ± 1.43
12137	-		-		**-13.11 ± 0.84**

	Methyl (R1)	Isopropyl (R2)	Carboxylate (R3)	Heterocyclic (R4)	Average ΔG_{vinaXB} (kcal·mol^{-1})
12138	-	(isopropyl carboxylate)	-	naphthalene, CH$_2$O$^-$	**-12.56 ± 0.57**
12139	-	(isopropyl carboxylate)	-	naphthalene, O$^-$	**-13.03 ± 0.57**
12140	-	(isopropyl carboxylate)	-	dihydroisobenzofuran	**-12.58 ± 0.47**
12141	-	(isopropyl carboxylate)	-	indene, CH$_2$O$^-$	-12.18 ± 0.59
12220	-	(isopropyl carboxylate)	(CH$_2$)$_2$COO$^-$	N-methylpiperidine, O$^-$	-11.56 ± 0.52
12221	-	(isopropyl carboxylate)	(CH$_2$)$_2$COO$^-$	purine (NH)	-11.95 ± 0.41
12222	-	(isopropyl carboxylate)	(CH$_2$)$_2$COO$^-$	pyridyl-piperidine	-11.62 ± 0.68
12223	-	(isopropyl carboxylate)	(CH$_2$)$_2$COO$^-$	piperidine, CH$_2$COO$^-$	-11.47 ± 0.41
12224	-	(isopropyl carboxylate)	(CH$_2$)$_2$COO$^-$	phenol-piperidine, O$^-$	-11.81 ± 0.61
12225	-	(isopropyl carboxylate)	(CH$_2$)$_2$COO$^-$	benzoate-piperidine	-11.77 ± 0.60
12226	-	(isopropyl carboxylate)	(CH$_2$)$_2$COO$^-$	benzamide-piperidine, H$_2$N	-12.10 ± 0.64

	Methyl (R1)	Isopropyl (R2)	Carboxylate (R3)	Heterocyclic (R4)	Average ΔG_{vinaXB} (kcal·mol^{-1})
12227	-				-12.26 ± 0.43
12228	-				-11.83 ± 0.40
12235	-				**-13.47 ± 0.61**
12236	-				-9.98 ± 1.24
12237	-				-12.44 ± 0.85
12238	-				-12.31 ± 0.58
12239	-				-12.42 ± 0.65
12240	-				-12.42 ± 0.46
12241	-				-11.98 ± 0.54
22235					-11.98 ± 0.51
22237					-12.01 ± 0.76

	Methyl (R1)	Isopropyl (R2)	Carboxylate (R3)	Heterocyclic (R4)	Average ΔG_{vinaXB} (kcal·mol^{-1})
22238					-11.84 ± 0.56
22239					-11.87 ± 0.53
22240					-11.48 ± 0.54
32235					-12.21 ± 0.55
32237					-12.22 ± 0.81
32238					-11.89 ± 0.68
32239					-12.06 ± 0.61
32240					-11.82 ± 0.58
42235					-11.98 ± 0.55
42237					-12.00 ± 0.79
42238					-11.74 ± 0.61

	Methyl (R1)	Isopropyl (R2)	Carboxylate (R3)	Heterocyclic (R4)	Average ΔG_{vinaXB} (kcal·mol^{-1})
42239					-12.08 ± 0.57
42240					-11.49 ± 0.55
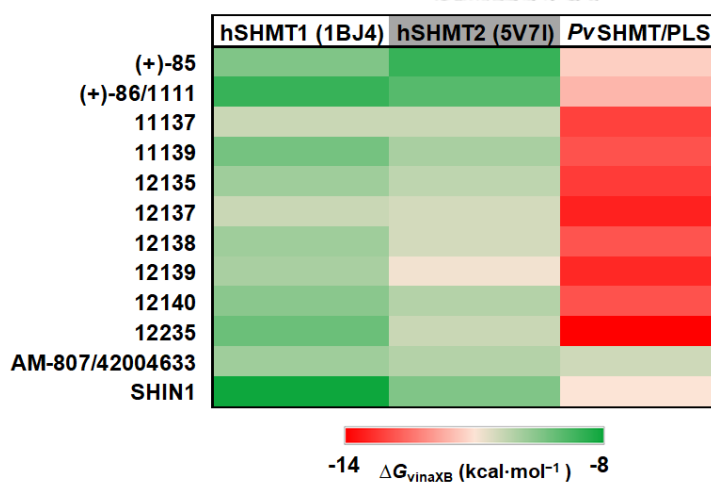
Fig. A2 The predicted binding affinity of eight newly designed pyrazolopyran-based compounds toward *Pv*SHMT/PLS, human SHMT1 (PDB entry 1BJ4 [1]) and human SHMT2 (PDB entry 5V7I [2]) compared to *Plasmodium* SHMT inhibitors (pyrazolopyran(+)-85 and (+)-86) and human SHMT inhibitors (AM-807/42004633 and SHIN1 [2-3]).

References

[1] S. B. Renwick, K. Snell, U. Baumann. Structure 6 (1998) 1105–1116. https://doi.org/10.1016/S0969-2126(98)00112-9.

[2] G. S. Ducker, J. M. Ghergurovich, N. Mainolfi, V. Suri, S. Jeong, A. Friedman, M. Manfredi, H. Kim, J. D. Rabinowitz. Proc. Natl. Acad. Sci. USA. 114 (2017) 11404–11409. https://doi.org/10.1073/pnas.1706617114.

[3] Y. Han, L. He, Y. Qi, Y. Zhao, Y. Pan, B. Fang, S. Li, J.Z.H. Zhang, L. Zhang. Chem Biol Drug Des. 97 (2021) 221–230. https://doi.org/10.1111/cbdd.13774.

APPENDIX B

SUPPLEMETARY INFORMATION FOR MANUSCRIPT II

***in silico* and *in vitro* potential of FDA-approved drugs for antimalarial drug discovery against *Plasmodium* serine hydroxymethyltransferases**

Pitchayathida Mee-udorn[a], Kochakorn Phiwkaow[b], Ruchanok Tinikul[c], Kamonpan Sanachai[d], Somchart Maenpuen[b], and Thanyada Rungrotmongkol[a,e]*

[a]Program in Bioinformatics and Computational Biology, Graduate School, Chulalongkorn University, Bangkok 10330, Thailand

[b]Department of Biochemistry, Faculty of Science, Burapha University, Chonburi 20131, Thailand

[c]Department of Biochemistry and Center for Excellence in Protein and Enzyme Technology, Faculty of Science, Mahidol University, Bangkok 10400, Thailand

[d]Department of Biochemistry, Faculty of Science, Khon Kaen University, Khon Kaen 40002, Thailand

[e]Center of Excellence in Biocatalyst and Sustainable Biotechnology, Department of Biochemistry, Faculty of Science, Chulalongkorn University, Bangkok 10330, Thailand

E-mail address: t.rungrotmongkol@gmail.com, thanyada.r@chula.ac.th

Phone: +66-2218-5426. Fax: +66-2218-541

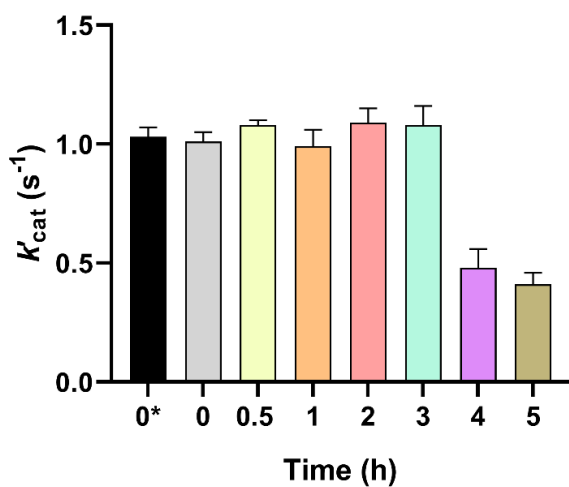**Fig. B1** The stability of His$_6$-*Pf*SHMT activity in 1% (v/v) DMSO at different incubation times, 0 (at start), 0.5, 1, 2, 3, 4, and 5 h, compared to the His$_6$-*Pf*SHMT activity measured at start in the absence of DMSO (0*). The result showed that His$_6$-*Pf*SHMT is catalytically active in 1% (v/v) DMSO within only 3 h. Error bars represent standard deviations (S.D.) from three replications of the data.
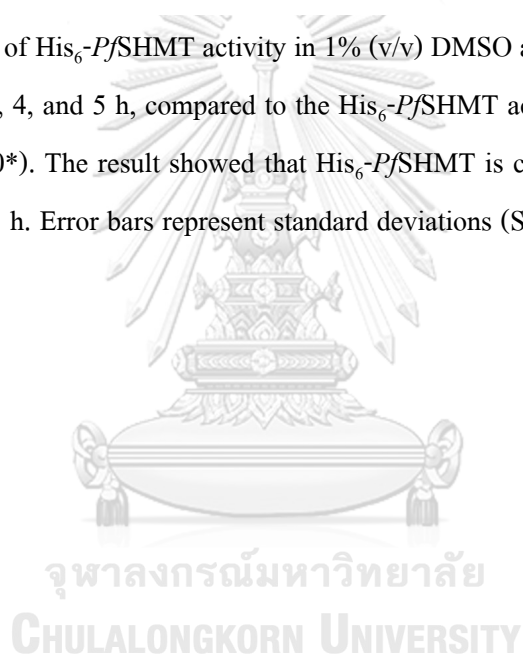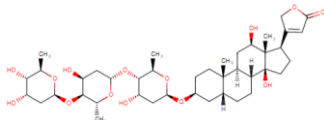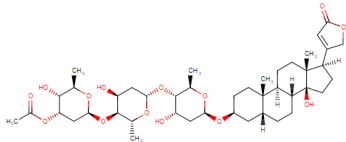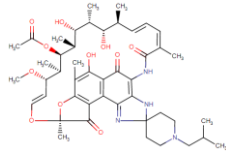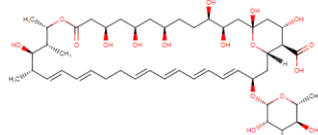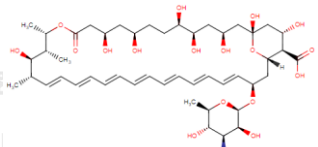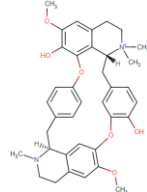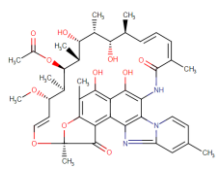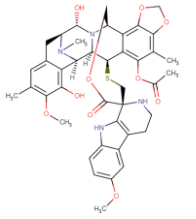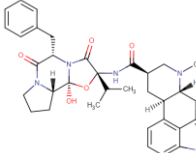
Table B1 The information on the eleven hit compounds [93], which were found in seven complexes of *Plasmodium* SHMTs by the molecular method. It should be noted that a selected compound for MD simulations is in bold text.

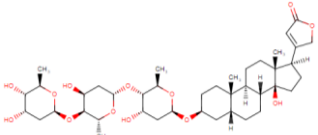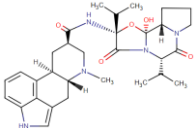|	Drugbank ID	Name	Molecular weight	2D structure
1	DB00390	Digoxin	780.9385	
2	DB00511	Acetyldigitoxin	806.9757	
3	DB00615	Rifabutin	847.0047	
4	DB00646	Nystatin	926.1070	
5	**DB00681**	**Amphotericin B**	**924.0790**	
6	DB01199	Tubocurarine	609.7312	
7	DB01220	Rifaximin	785.8785	

	Drugbank ID	Name	Molecular weight	2D structure
8	DB01396	Digitoxin	764.9391	
9	DB11273	Dihydroergocornine	563.6990	
10	DB12674	Lurbinectedin	784.8800	
11	DB13345	Dihydroergocristine	611.7430	
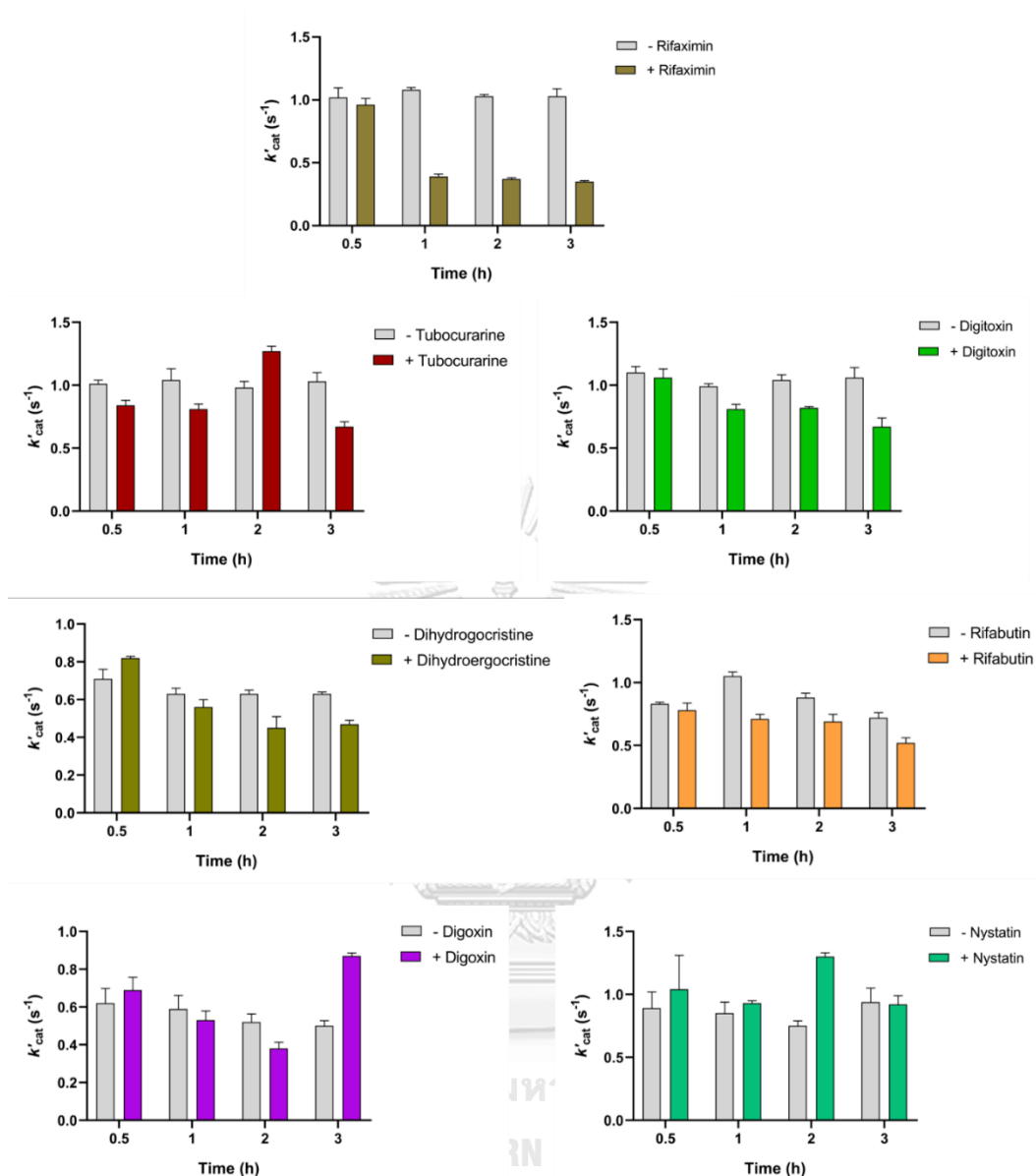
Fig. B2 Time-dependent inhibition of His$_6$-*Pf*SHMT by the rest compounds at a concentration of 100 µM. The His$_6$-*Pf*SHMT activity was measured in the presence of 100 µM of each compound at different incubation times (0.5, 1, 2, and 3 h). Error bars represent standard deviations (S.D.) from three replications of the data.

	N262	D258	Q259	E75	E89	E90	K251	K61	F266	S263	Y63	Y78	V365	
H	0	0	0	0	0	0	0	0	0	0	0	0	94	94%
H	0	0	0	0	0	0	0	0	99	0	77	0	0	100%
HBA	97	0	0	0	0	0	0	0	0	0	0	0	0	97%
HBA	0	0	0	0	0	0	0	22	0	0	0	0	0	22%
HBA	0	0	0	0	0	0	0	0	0	0	0	99	0	99%
HBA	99	0	0	0	0	0	0	0	0	0	0	0	0	99%
HBA	0	0	0	0	0	0	90	0	0	0	0	0	0	90%
HBD	0	0	0	1	5	30	0	0	0	0	0	0	0	37%
HBD	0	0	0	0	0	0	0	0	99	8	0	0	0	100%
HBD	0	0	1	0	0	0	0	0	0	13	0	0	0	15%
HBD	0	47	2	0	0	0	0	0	0	0	0	0	0	49%
HBD	0	65	0	0	0	0	0	0	0	0	0	0	0	65%
HBD	0	0	0	0	0	0	0	0	0	0	0	94	0	95%
NI	0	0	0	0	0	0	99	0	0	0	0	0	0	100%
PI	0	0	0	0	2	18	0	0	0	0	0	0	0	21%

Fig. B3 The interaction heatmap of *Pf*SHMT/PLS/amphotericin B complex, which was calculated from the pharmacophore modeling method with the percentage of occurrences $\geq 20\%$. Note that H is hydrophobic, HBA is H-bond acceptor, HBD is H-bond donor, NI is negative group and PI is positive group.
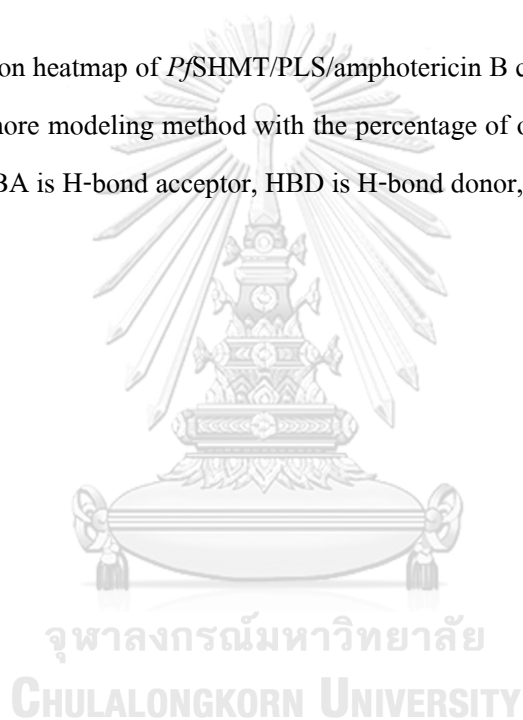
VITA

NAME	Pitchayathida Mee-udorn
DATE OF BIRTH	19 April 1995
PLACE OF BIRTH	Phrae, Thailand
INSTITUTIONS ATTENDED	2007-2012 High School Nareerat School, Phrae
	2013-2016 B.Sc. (Biology), First-Class Honors Naresuan University, Phitsanulok
	2017-Present Ph.D. Chulalongkorn University, Bangkok
HOME ADDRESS	92/1 Moo 4 Hua-Muang, Song, Phrae, Thailand
PUBLICATION	1. Pitchayathida Mee-udorn, Bodee Nutho, Romchalee Chootrakool, Somchart Maenpuen, Ubolsree Leartsakulpanich, Penchit Chitnumsub, and Thanyada Rungrotmongkol. J. Mol. Liq. 2022. 362: 119737-119746. https://doi.org/10.1016/j.molliq.2022.119737.
	2. Sakunrat Ubonprasert, Juthamas Jaroensuk, Wichai Pornthanakasem, Nuntaporn Kamonsutthipaijit, Peerapong Wongpituk, Pitchayathida Mee-udorn, Thanyada Rungrotmongkol, Onuma Ketchart, Penchit Chitnumsub, Ubolsree Leartsakulpanich, Pimchai Chaiyen, Somchart Maenpuen. J. Biol. Chem. 2019. 294(27), 10490-10502. https://doi.org/10.1074/jbc.RA119.007454.
AWARD RECEIVED	1. Outstanding Poster presentation award at the 25th International annual symposium on computational science and engineering (June 8-11, 2022, Khon Kaen University)
	2. Outstanding Poster presentation award at the 23rd International annual symposium on computational science and engineering (June 27-29, 2019, Chiang Mai University)